IMT School for Advanced Studies, Lucca
Lucca, Italy
In joint supervision with
University of Seville
Seville, Spain

COMPUTATIONAL FRACTURE MECHANICS FOR RELIABILITY OF COMPOSITES AT THE MICRO AND MACRO SCALES

PhD in Institutions, Markets and Technologies
Curriculum in Computer Science and Systems Engineering
XXXII Cycle

By

Teresa Guillén Hernández

2020

The dissertation of Teresa Guillén Hernández is approved.

Program Coordinator: Prof. Marco Paggi, IMT School for Advanced Studies, Lucca

Supervisor: Prof. Marco Paggi, IMT School for Advanced Studies, Lucca

Supervisor: Dr. José Reinoso Cuevas, University of Seville

Tutor: Prof. Marco Paggi, IMT School for Advanced Studies, Lucca

The dissertation of Teresa Guillén Hernández has been reviewed by:

Prof. Gianni Royer Carfagni, University of Parma

Prof. Albert Turon Travesa, University of Girona

Dr. Fabian Welschinger, Robert Bosch GmbH

IMT School for Advanced Studies, Lucca

2020

To my family

Contents

List of Figures

List of Tables

Acknowledgements

First of all, I would like to express my deep gratitude to Prof. Marco Paggi and Dr. José Reinoso Cuevas for providing me the opportunity of this work as well as for their guidance, ideas, attention and support.
The present thesis is based on the articles listed in the Publications Section. These articles are co-authored by Prof. Marco Paggi, Dr. José Reinoso Cuevas, Dr. Israel García García, Dr. Adrià Quintana Corominas, Prof. Albert Turon Travesa and Dr. Valerio Carollo.
I would like to thank Dr. Israel García García for his infinite help. The collaboration with him has led to the research described in Chapter 6.
I would also like to thank Dr. Adrià Quintanas Corominas for his work, support and availability. The collaboration with him has led to the research described in Section 6.3.
I have to mention Dr. Valerio Carollo to express my gratitude for his help, advice and availability during the beginnings of my PhD.
I am very grateful to my colleagues and friends from IMT Lucca and from the Group of Elasticity and Strength of Materials at the University of Seville, for the enjoyable moments spent during these years and their scientific and personal support.
Finally, I want to thank my family and friends, especially my parents, for their love, patience and confidence on me during the last 28 years.

Publications

1. V. Carollo, T. Guillén-Hernández, J. Reinoso and M. Paggi. "Recent advancements on the phase field approach to brittle fracture for heterogeneous materials and structures". *Advanced Modeling and Simulation in Engineering Sciences* 5.1 (2018): 8.
2. T. Guillén-Hernández, J. Reinoso and M. Paggi. "Fracture analysis of thin films on compliant substrates: A numerical study using the phase field approach of fracture". *International Journal of Pressure Vessels and Piping* (2019).
3. T. Guillén-Hernández, I.G. García, J. Reinoso and M. Paggi. "A micromechanical analysis of inter-fiber failure in long reinforced composites based on the phase field approach of fracture combined with the cohesive zone model". *International Journal of Fracture* (2019): 1-23.
4. T. Guillén-Hernández, J. Reinoso and M. Paggi. "Phase field model for fracture analysis of functionally graded power-based shell structures." *Mechanics of Advanced Materials and Structures* (2020): 1-11.
5. T. Guillén-Hernández, A. Quintana-Corominas, I.G. García, J. Reinoso, M. Paggi and A. Turon. "In-situ strength effects in long fibre reinforced composites: a micro-mechanical analysis using the phase field approach of fracture". *Theoretical and Applied Fracture Mechanics* (2020): 102621.

Abstract

In recent years, an increasing use of composite materials in aerospace and aeronautical applications has taken place. Fibre reinforced composites materials (FRCs) present high specific strength and stiffness ratios, which can be considered as remarkable advantages with respect to metallic materials. One of the main problems associated with the internal arrangement of fibre reinforced materials regards the numerous and complex failure mechanisms that can occur at different scales of observations. Stemming from these reasons, at present, the analysis and study of fracture in fibre composites constitutes a relevant and recurrent area of research due to the actual needs for the achievement of a higher level of understanding of such fracture phenomena. Within this context, this dissertation presents a new model to simulate fracture in FRCs with the aim of designing safe and durable aircraft structures, for instance: shells, plates or thin film-substrate structures. The fundamental computational model used in the present thesis was proposed in (14), devising a seminal combination of the Phase Field approach for brittle fracture and a Cohesive Zone Model for interface failure. In the current research, this computational framework is examined and validated through the numerical simulations of different applications at the micro- and macro-scales: (i) the micro-mechanical inter-fiber failure of composites, the subsequent propagation of failure through the thickness of the laminates arising a macro-crack and (ii) several macro-mechanical applications concerning advanced composite structures (shells, thin film-substrates and Functionally Graded Materials). Derived from the current predictions, it is possible to argue that the current numerical methodology is very suitable for the simulation of fracture in composites at different length scales and allows the preclusion of intricate remeshing techniques or crack tracking algorithms in conjunction with minimizing the mesh-dependent pathology due to its non-local character.

Chapter 1

Introduction

1.1 Introduction to composite materials

Composite structural systems and materials are present in a wide range of applications such as sporting or marine goods, automotive, bio-medics and aerospace, among many others. The widespread use of such components strives for the achievement of very specific structural and mechanical performance that are generally subjected to current practical demands.

With regard to the development of composite materials in engineering practice, these materials emerge from the combination of two or more materials obeying different internal arrangements, i.e. displaying long and short fibers within a domain or spherical-like inclusions, among many others. The objective is to obtain a new material with improved mechanical properties than those corresponding to its constituents. The advent of new composites is promoting the replacement of traditionally employed metals with the aim of achieving superior performances, for instance in terms of weight-to-strength and -stiffness, fatigue resistance, preclusion of corrosion, to quote a few of the main current targets.

From a mechanical perspective, reinforcements provide the stiffness and strength to the new material, whereas the matrix, generally protects the reinforcements and gives shape to the structure keeping its consistency in terms of the position and orientation of the reinforcements. Therefore, reinforcements can be understood as the main load-carrying phase, while the matrix transmits the loads between them. Usual ar-

rangements that comply with the previous description are the so-called long- and short-fiber reinforced polymeric composites, LFRPCs and SFRPCs respectively, whose reinforcements can be performed using carbon (denominated as CFRPs), glass (called as GFRPs) and polyamide materials, among many others. Normally, composite structures and coupons are made by the superposition of several layers of reinforcements and matrix with different orientations (See Figure 1) which is called laminate.

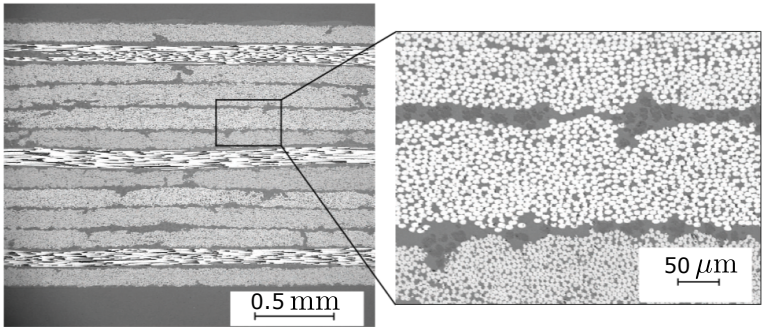

Figure 1: Micro-graphs of a carbon fiber/epoxy laminate (cross-section) made from 13 plies of Hexcel T800S/M21 prepreg with the following stacking sequence: $[+45^\circ/90^\circ/-45^\circ/+45^\circ/-45^\circ/0^\circ/90^\circ/0^\circ/-45^\circ/+45^\circ/-45^\circ/90^\circ/+45^\circ]$. Taken from (1).

A different conception of composites can be understood by the combination of several components made from different materials, as can be the case of thin film-substrate systems (see Figure 2) and functionally graded materials (see Figure 3).

Although composite materials are used in several applications, these materials have been extensively incorporated into the aerospace and aeronautical industries. Formerly, they were principally used in small components with low level of load-carrying responsibility, but nowadays, structural components of primary level of responsibility are made from composite materials. In this setting, Figure 4 depicts the increasing use of composites in aircraft constructions over the last years.

However, due to the intricate nature of composite materials and structures, their damage behaviors significantly differ from alternative materials and systems, generally more complicated, and dependent upon several factors including: the properties of the constituent materials, the fiber-nature orientation and arrangement, the stacking sequence, loading

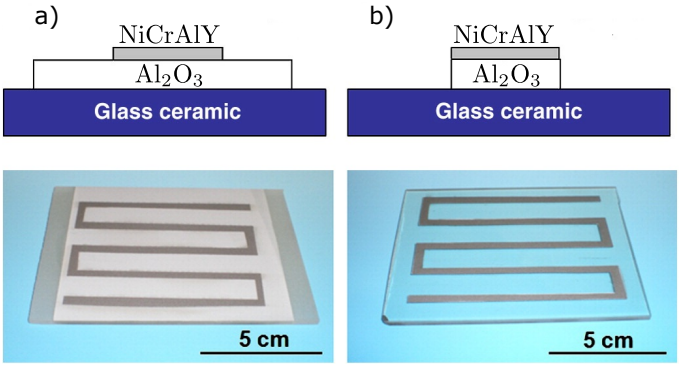

Figure 2: Schematic cross-sections and pictures of thin films-substrate systems. a) coatings or films with different width (Al_20_3 area wider than NiCrAlY area). b) coatings or films with the same width. Taken from (2) with permission.

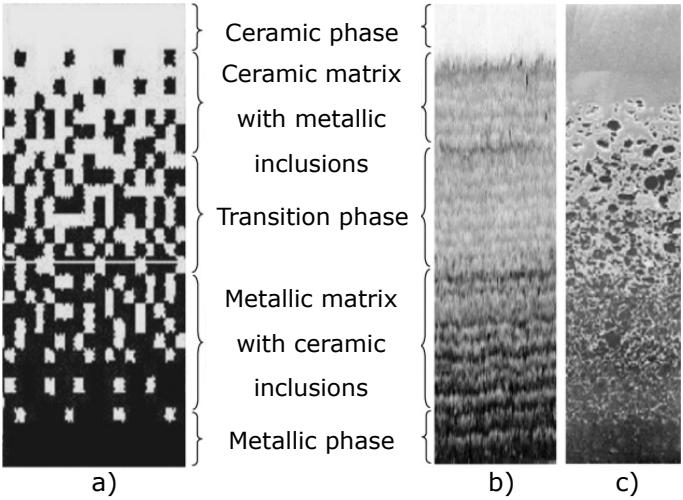

Figure 3: Scheme of a graded ceramic-metallic micro-structure. a) smoothly graded micro-structure. b) enlarged view. c) ceramic-metallic FGM. Taken from (3) with permission.

conditions, to mention just a few.

Correspondingly, within the context of current demands, the achieve-

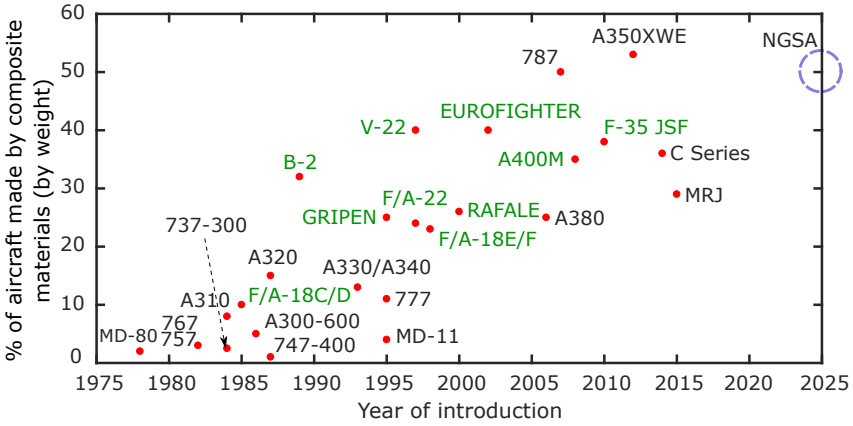

Figure 4: Aircraft composite content: military aircraft in green. Adapted from (4).

ment of a more profound understanding of failure in composite materials and structures constitutes a crucial challenge in order to prevent cracks and preserve the integrity of different systems in practice. In this setting, it is worth noting that unsolved issues still endow the accurate prediction of onset and propagation of failure events that can occur at different scales of observation. In this regard, this work is devoted to the analysis of failure events of rate-independent materials at the micro- and macro-scales with a continuum-based representation.

In the forthcoming section, a brief review of the most prominent failure modes of composite materials (LFRPs) at different scales is outlined.

1.2 Fracture of composite materials

Composite materials are affected by numerous failure modes which are very difficult to understand. The reason of this intricacy relies on the presence of different phases at different length scales, in other words, the inherent heterogeneity of these materials, which leads to a significant complexity in the failure progression.

From a macro-scopic perspective, failure modes in LFRPs comprise: (i) intra-laminar breakage (i.e. within the lamina) and (ii) inter-laminar fracture, along the interfaces between the individual plies. Intra-laminar

failures usually encompass fiber and matrix dominated fracture events. Usually, matrix dominated damage mechanisms occur at lower loading levels in comparison to fiber breakages (see Figure 5) which only take place at the last failure stages and in most of the times result to a catastrophic failure. Thus, transverse cracking through the thickness of the ply (see Figure 6) due to matrix cracking can be followed by delamination event (see Figure 7) which can be induced by the transverse cracks or starting at the free edges. It is worth mentioning that, matrix cracking, is the result of the coalesce of micro-cracks. These micro-cracks normally arise due to an initial fiber-matrix decohesion, known as debonding, followed by the propagation of the crack through the interface until a certain point where penetrates or kinks into the matrix (see Figure 8).

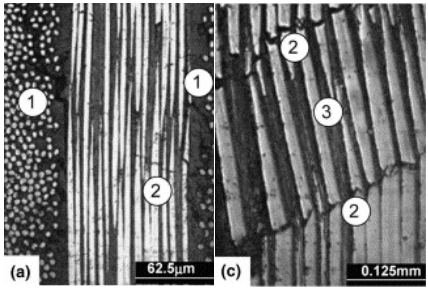

Figure 5: Micro-graphs of the fiber breaking in a $[0^\circ/90^\circ]_{15}$ carbon/epoxy laminate. 1. Matrix cracking. 2. Fiber breaking. 3. Kink band. Adapted from (5) with permission.

1.3 Review on computational fracture mechanics for composites

This section presents a brief overview of the state of the art of computational techniques for modelling fracture events in composite materials. Moreover, it is noting that some portions of the present contents are extracted from (15; 16).

Fiber reinforced composite materials (GFRP and CFRP) are widely used in aeronautical and aerospace applications with demanding requirements of high specific stiffness and strength ratios. However, as was previously mentioned, these materials present several failure modes that

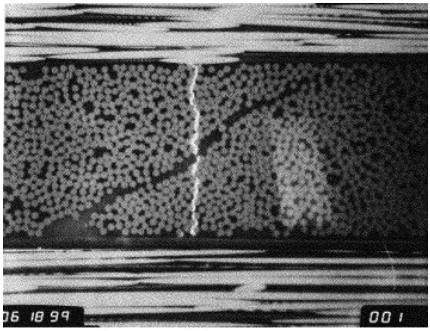

Figure 6: Transverse crack in a laminate with $[0^\circ/90^\circ/0^\circ]$ stacking sequence. Taken from (6) with permission.

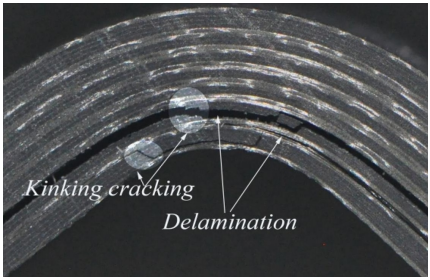

Figure 7: Delamination in a curved laminate. Taken from (7) with permission.

are very complex and therefore, difficult to characterize and understand. For this reason, it is very important to know better the fracture process of composites in order to optimise their load bearing capabilities.

For this purpose, computational fracture mechanics (CFM) has been used over the years due to its accurate predictions of damage onset and conditions leading to crack growth. To point out that, CFM can be conceived as a potential alternative to experimental tests due to its versatility for applying different loading conditions and using complex or huge geometries. Moreover, numerical predictions also incur into important cost savings in conjunction with allowing the efficient identification of the different stages of damage upon loading application.

In order to understand fracture in composite materials, micro-mechanical models are widely used. Some of the reasons for the increasing

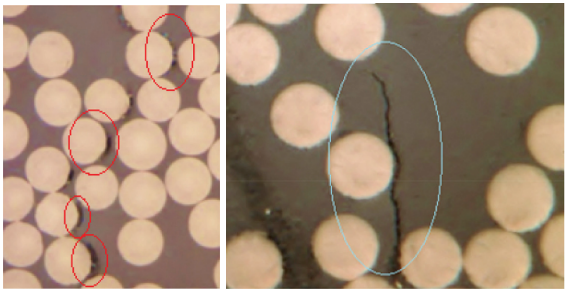

(a) (b)

Figure 8: Micro-mechanical inter-fiber failure. (a) Debonding. (b) Debonding and kinking into the matrix. Adapted from (8) with permission.

interest on micro-mechanical models are the following: the nature of failure in composites is strongly affected by damage at the micro-scale and micro-mechanical models provide a profound understanding of the physical phenomena. The key concept of the micro-scale simulations is the definition of the RVE domain (statistically representative volume element) which can be generated by digital images analysis (12), using statistical methods (12; 17; 18), deterministic models (19) or a combined experimental-numerical method (20). To highlight that, the RVE is the minimum volume of the material whose properties are representative of the complete material. From experimental observations we can argue that, fiber-matrix decohesion (also known as inter-fiber failure) is the most common way of failure initiation at the micro-scale. It generates an interface crack, which growths in a stable mode, until a certain point where migrates into the matrix. Therefore, micro-cracks arise and their coalesce provokes the appearance of macro-scopic inter-fiber cracks. For that reason, debonding between fibers and matrix has been studied in the last two decades using several numerical strategies (finite element method (FEM), boundary element method (BEM) or extended finite element method (XFEM)), models (finite fracture mechanics (FFM), linear elastic fracture mechanics (LEFM), cohesive zone model (CZM) or phase field (PF)) and problems (single-fiber problem, two fibers problem, unidirectional (UD) laminates or cross ply laminates).

The single-fiber problem is considered by many authors as a benchmark for the prediction of the sequence of stages of failure initiation in

the micro-scale. Within the context of linear elastic fracture mechanics (LEFM), this problem has been solved under transverse tension (21), biaxial tension (22) and transverse compression (23) using the boundary element method (BEM) to estimate the energy release rate (ERR) of fiber-matrix debonding cracks. Moreover, the effect of the inclusion of a secondary fiber has been analyzed in (24) while in (25) a higher number of fibers are considered. However, with LEFM, the crack onset cannot be predicted, it is necessary the existence of an initial crack. Therefore, an initial debonding angle around to 10° is assumed. Also, the crack propagation trough the matrix cannot be captured. It is worth mentioning that an analytical procedure to evaluate the debonding angle was conducted in (26; 27) but in different applications.

The coupled stress-energy criterion, also known as finite fracture mechanics (FFM), has been used to study the mono-fiber problem under tension (28) within the BEM framework. It can predict the crack onset but cannot capture the migration of the crack into the matrix.

About the simulation of the interfaces between fibers and matrix, linear elastic interfaces (also known as weak interfaces) and cohesive zone models (CZM) are used within the BEM (29; 30) and FEM (31; 32; 33) framework. This two methods eliminate the assumption of the stress singularity at the crack tip supposed by LEFM. Therefore, they can predict the crack onset. The first method considers a continuous distribution of linear-elastic springs between both sides of the interface. When the surfaces of an interface separate, traction increases until a maximum resulting a complete separation. However, the novelty of CZM is the consideration of the fracture process zone. This is a zone ahead of the actual crack tip where there are cohesive tractions. In other words, when the surfaces of an interface separate, traction increases until a maximum and then, progressively, reduces to zero (softening) resulting a complete separation.

To capture the propagation of the crack through the matrix, pressure dependant elasto-plastic models are used to describe the behavior of the matrix (18; 34). These models consider that plastic strain localization causes fracture events. It is worth mentioning that, plastic strain localization areas are known as shear bands and they determine the crack paths. Some of these elasto-plastic models use the Mohr-Coulomb yield criterion (35) and others the Ducker-Pagger yield criterion (36). Finally, some authors coupled elasto-plastic models with smeared local damage models (33; 37; 38) which are known as elasto-plastic damage models. In (33; 37) the yield criterion used is paraboloidal. Therefore, the non-

linear behaviour of polymers under compression can be properly captured (39). However, in (38) the yield criterion is a modification of the Drucker–Prager yield function and no hardening effect is considered. It is important to highlight two aspects. Firstly, all the previous elasto-plastic and elasto-plastic damage models are solved with FEM. Secondly and finally, the smeared local damage models are rooted on continuum damage mechanics (CDM) which means that, instead of having a strong discontinuity as in the models based on fracture mechanics (LEFM, FFM, CZM), there is a smeared crack. In other words, damage is not consider as a discontinuous phenomenon because there is progressive degradation of the material properties.

Another smeared damage model used to simulate the mono-fiber problem within the FEM framework is the phase field (PF) (40). This model is hybrid because is rooted on fracture mechanics but within the framework of smeared crack models. The advantages of this model are the following: it can capture the onset of damage (there is no need of assuming an initial crack) and the crack growth through the matrix. Moreover, there is no mesh dependency due to its non-local character.

After the investigation of the single-fiber problem, the following step is the analysis of fracture in laminates. In particular, transverse cracking of cross ply laminates have been widely investigated because it is one of the most controversial failure in composites. The seminal work conducted by (41) on $[0/90]_s$ laminates showed that the reduction of the 90° layer thickness provokes an increase in the critical strain for transverse cracking initiation. Therefore, for sufficiently thin 90° layers, the actual strength response of the laminate would be that associated with the 0° supporting layers, being this scenario of crucial importance for the incorporation of thin and ultra-thin plies in composite structures. This behaviour is denominated as *in-situ* strength response in fiber reinforced composites.

The incorporation of such effect in macro-scale models of composite laminates can be accounted for using the analytical procedure proposed by Camanho et al. (42; 43), recalling the fundamental concepts on fracture mechanics proposed by Dvorak, through the affection of the strength values associated with: (i) in-plane transverse tensile Y_T^{is} and compression Y_C^{is} effects, and (ii) in-plane shear S_L^{is} and transverse shear S_T^{is} effects. To say that, where the analytical solutions cannot be developed, the FEM is used to solve numerically these problems (44; 45). An alternative methodology is that relying on finite fracture mechanics developed by García et al. (46; 47) whereby a semi-analytical expression

for the prediction of the critical strain originating the first crack onset is derived in conjunction with a rigorous size effect law depending upon the central 90° layer thickness. In (46) the results of a 2D model within the BEM are shown and in (47) a 3D model is simulated using the FEM with remeshing techniques. Apart from these valuable results, García et al. (46) performed a careful overview with regard to the main models existing in the related literature addressing the *in-situ* strength effect. These models can be categorized as: Incremental energy models (48; 49; 50), Dvorak-based formulations (42; 51; 52) and statistical-based models (53; 54). To point out that, models rooted on fracture mechanics (LEFM, FFM or CZM) present problems on tracking the crack path. Therefore, to solve these problems smeared crack models (PF or CDM discussed previously), remeshing techniques or Extended Finite Element Models (XFEM) (55; 56; 57) are used.

At present, as a consequence of the advent of new numerical capabilities, a different perspective for the analysis of *in-situ* strength effects in thin-ply composite laminates concerns the exploitation of micromechanical models. The principal aim of the use of micro-mechanics is to provide a potential explanation via the reproduction of fracture patterns in terms of initiation and propagation of crack events at lower scales that can shed light to the experimental observations presented in (11). Specifically, Saito and coauthors (11) identified the reduction of the corresponding energy release rate as the main cause for transverse crack suppression effect and highlighted the higher crack density for thinner plies. Interestingly, Sebay et al. (58) idealized an experimental procedure enabling the transverse cracking detection via optical means with relevant results on the matter. Within this context, from a numerical standpoint, previous works analyzed via numerical techniques the appearance of matrix cracking and fiber-matrix decohesion at the micro-scale (22; 28; 59) as we have discussed previously in this section. Comprising, high-fidelity micro-structures of fiber reinforced composites, Arteiro et al. (60) developed a finite element (FE)-based framework including pressure-dependent plasticity models and cohesive zone formulations for triggering matrix and fiber-matrix decohesion failure, respectively, showing completely different failure patterns for cross-ply laminates with standard thickness and thin-ply 90° layers in good agreement with experimental results and identifying such *in-situ* effect in transverse compression and pinpointing the assumable reliability of simple analytical models proposed in (42). Following a similar approach, Herráez et al. (61) estimated via computational micro-mechanics

that the transverse ply strength was independent of the 90° layer thickness. In this direction, París et al. (62) addressed the investigation of the initial phases of damage of 90° plies based on linear elastic fracture mechanics concepts and precluding the potential coalescence of interface cracks throughout the polymeric matrix, where boundary element (BE)-based models with fracture mechanics capabilities were generated for this purpose. These authors claimed that, at these initial phases along the cracking stage, such *in-situ* effect was not captured due to the fact that evolution of the energy release rate of a debonding crack ($\mathcal{G}_c$) was not affected by the neighboring 0° layer.

In contrast, Kohler et al. (63) carried out an experimental and numerical study (using an embedded multi-scale approach), whose main results showed a good experimental-numerical agreement pinpointing the occurrence of the *in-situ* strength effect.

Despite the importance in practical applications and the great deal of research that has been devoted to this topic, there exits a clear lack of apparent consensus with regard to the possible causes generating *in-situ* strength effects.

1.4 Advanced composites in aeronautical and aerospace applications

Nowadays, thin-walled structures (shells and plates) are extensively used in the construction of aircrafts (64; 65; 66). They can be stiffened with stringers and frames, as we can see in Figure 9, to prevent buckling under compressive loads. Another modern structure used is the sandwich panel (67; 68; 69) due to its high bending strength and stiffness. This structure presents two stiff outer skins, also known as thin films or coatings, over a thick, compliant and lightweight core or substrate (see Figure 10).

One of the main advantages of composites is the possibility of being tailored differently depending on their applications. Following this idea, a new composite material known as functionally graded material (FGM) arises. This composite material is made of several phases where the volume fractions of its constituents vary smoothly and continuously within the specimen domain, especially along the thickness direction in the case of shells. Commonly, FGMs are made of ceramic and metallic phases (70), but alternative combinations can be found in the related literature,

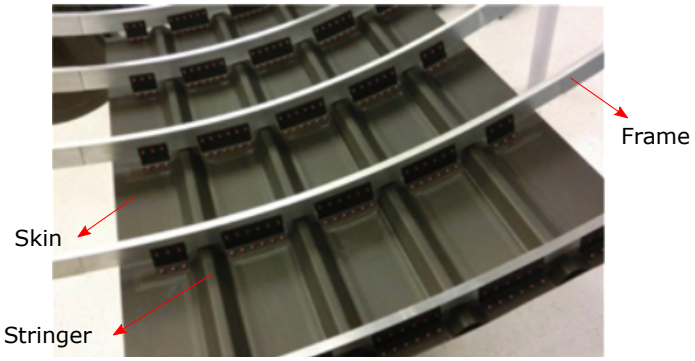

Figure 9: Thin-walled panel. Taken from (9).

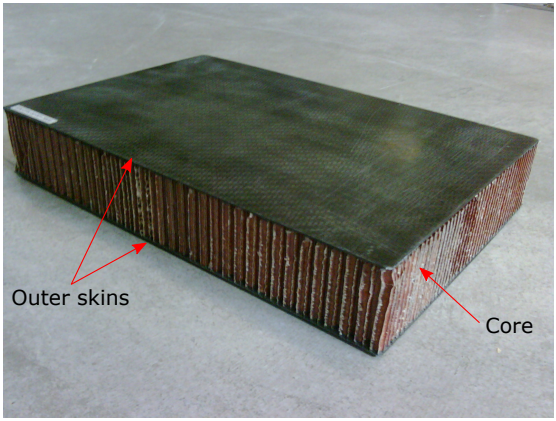

Figure 10: Sandwich panel. Taken from (10).

see (71; 72) and the references given therein. Due to the combination of different materials and also to the smooth variation of their composition, FGMs have very important advantages with respect to conventional materials. For example, in interfaces between conventional layer-based materials, the existing elastic mismatch on the material properties generally leads to notable interfacial stresses that can provoke structural failure. However, using FGMs, this problem is overcome because the discontinuity on the material properties is highly reduced. Moreover, FGMs present good mechanical and thermal properties because they can be tai-

lored depending on their applications.

In aerospace applications, thermal barrier coatings (TBC) play a very important role. These coatings have to protect the substrate from very high temperatures, bigger than the substrate admissible temperature. TBC can be obtained using the advanced composite materials seen before, FGMs (73; 74), or using thin film-substrate systems (75; 76).

To conclude, shells, thin film-substrate systems (TBC or sandwich panels) and FGMs are very important concepts in aeronautical and aerospace applications because they are widely used in modern aerostructures. For that reason, applications involving them are going to be analysed in this dissertation.

1.5 Motivation, state of the art and objectives

The present PhD thesis is aimed at analyzing fracture phenomena in composites (heterogeneous materials) because, as it has been said before, to increase the durability, efficiency and applicability of aerostructures, it is necessary to predict their failure. In particular, the original combination of the phase field method and cohesive-like interface crack methods has been used in this dissertation to accurately predict failure in micro and macro-mechanical applications. Concretely, 3 different applications have been explored: fracture of long-fiber reinforced composites, fracture of thin films on compliant substrates and fracture of functionally graded power based shells. Finally, to mention that this section is based on (15; 16; 77; 78).

1.5.1 Fracture of long-fiber reinforced composites

The state of the art of this section has been extensively discussed previously. In this thesis, the inter-fiber failure and the so-called *in-situ* strength effects have been investigated in order to know and understand better the fracture process of composites. To do that, the phase field model combined with a compatible cohesive zone model has been used (14). The reason of that are the numerous advantages of this technique with respect to other alternatives given in the literature. Some of these advantages are: there is no mesh dependency due to its non-local character, there are no problems tracking the crack path, there is no need of using remeshing techniques, is based on physically sound parameters,

gives very good results with brittle matrices and captures the crack onset and the subsequent crack propagation through the matrix.

1.5.2 Fracture of thin films on compliant substrates

Coatings or thin films supported on compliant substrates are used in a wide range of applications: electronic packages, coatings for thermal barriers, chemical or abrasion protection, among many others (79; 80). However, thin film-substrate systems can experience different fracture events, which can limit the performance and mechanical integrity of the corresponding engineering systems. An overview of the failure modes of thin film-substrate systems under tension and under compression is given in (81) and (73), respectively.

In order to achieve a deep understanding of thin film-substrate designs, numerous studies have been carried out in the last three decades through analytical, experimental and numerical methods (mostly using the nonlinear finite element method, FEM). The complexity of these systems provokes the appearance of multiple fracture patterns as a consequence of the notable elastic mismatch of the constituents. Within the framework of linear elastic fracture mechanics (LEFM), Hutchinson and coauthors (82; 83) provided an overall picture with regard to the energy release rate associated with penetration-deflection scenarios for general layered materials, whose fundamental results have been later recalled in (84; 85; 86) and the references given therein. Numerically, many recent investigations prolifically dealt with the use of cohesive zone models (87; 88) for triggering delamination events in thin layer-substrate systems, whereby inelastic processes due to fracture have been mostly confined to the interface between the composing parts (73; 89).

However, in the present thesis, the phase field model combined with a compatible cohesive zone model has been used (14). This new technique is able to capture bulk damage and deflection or penetration at the interfaces in a robust and reliable manner. Moreover, it is capable of predicting several complex crack paths such coalescence and branching and enables overcoming some of the most remarkable limitations of discontinuity-based methods (90; 91). Therefore, in this work we analyze crack events in thin film-substrate systems subjected to tensile stresses, with the aim of gaining a more profound understanding of the failure mechanisms that interplay in their designs.

1.5.3 Fracture of functionally graded power based shells

Functionally graded materials (FGMs) are used in a wide range of high tech applications such as bio-medics (92; 93), thermal barrier coatings (94), or sensors (95), among many others. One of the most prominent forms for the practical use of FGMs is their incorporation as thin-walled structures which have been concurrently exploited in many engineering applications such as energy absorbing components (96; 97), structural components in aeronautics (64; 98; 99), or photovoltaic panels (100).

Therefore, research activities on structural theories, encompassing beams, plates and shells, have attracted the attention of numerous researchers. In this setting, with special focus on shell-based structures, an impressive range of models for shells have been proposed so far. A possible categorization of the existing shell models can differentiate between classical and novel/advanced shell formulations. Thus, well-established models, known as classical shell theories (CST), encompass the popular Kirchhoff-Love (3-parameter) and Reissner-Mindlin (5-parameter) theories (101; 102). Both of such CST make some mechanical assumptions across the thickness advocating the *dimensional reduction* concept that allows referring the magnitudes to the shell mid-surface. However, Kirchhoff-Love (3-parameter) and Reissner-Mindlin (5-parameter) theories inherently imply the adoption of relevant hypotheses regarding the out-of-plane response of the shell body, which directly embody the simplification of the constitutive tensor via a plane stress formulation. Note that in both CST formulations, the assumption concerning the inextensibility of the shell director vector is put forward, which means that the strains in the thickness direction are not taken into consideration. To overcome this limitation, higher order theories (HOT) have been developed in the last two decades. Within this context, Carrera proposed the so-called unified formulation (CUF) (103). In brief, the CUF is an axiomatic model that is postulated via the consistent expansion of the displacement field (u_i) complying with the following scheme:

$$u_i = u_{0i} + z^j u_{ji} \qquad \text{with} \quad i = x, y, z \quad \text{and} \quad j = 1, ..., N \tag{1.1}$$

being N the order of expansion and u_{0i} the displacement of the mid-reference surface in the i-th direction. This formulation is able to cover the equivalent single layer (ESL) and the layer-wise (LW) approaches (104; 105) in an amenable and robust manner.

Alternative to CUF-based models, continuum-based shell elements have been extensively exploited in the last years, with special attention

to the so-called solid shell kinematic model and the corresponding finite element discretization schemes, see (44; 106; 107) and the references therein given. Despite the appealing aspect of such solid shell formulations, including the avoidance of using rotational degrees of freedom and the fully 3D constitutive description of the shell body, their corresponding discrete models using low-order (namely first-order) displacements interpolation are prone to suffer from locking. These locking pathologies provide artificially stiffer solutions, and to overcome such issues numerical techniques such as the enhanced assumed strain method (EAS), the assumed natural strain method (ANS) and the reduced integration formulations (108; 109; 110; 111; 112; 113) are invoked. For specialized previous shell models for FGMs, the reader is referred to fundamental references, see (114; 115; 116; 117; 118).

Furthermore, the technical importance of shells in many industrial sectors motivates the development of predictive modelling methods for the accurate prediction of fracture events in such components. Nonetheless, this is a very challenging task due to the imbrication of curved geometries, potential geometrical nonlinear effects, among other aspects. In this concern, different fracture formulations have been formulated in the related literature during the last years such as the Extended-FEM (X-FEM) (119; 120), cohesive zone models (CZM) (88; 121; 122; 123; 124) to quote a few of them. Particularly, both X-FEM and CZM techniques fall into the category of *strong discontinuous crack methods*, which present notable difficulties in tracking the crack path and require the adoption of ad-hoc criteria for crack initiation and propagation criteria.

In contrast to the previous cracking methodologies, *smeared crack* techniques can be conceived as potential modelling tools for triggering fracture phenomena in solids. Specifically, the so-called phase field (PF) approach of fracture is characterized by the introduction of a damage-like field within the formulation, regularizing the variational formalism associated with the fracture theory of Griffith. PF methods permit the simulation of complex fracture phenomena in very elegant and consistent manner with the only use of physically sound material parameters (40; 125; 126; 127).

Despite the notable development of PF in the last years, the application of such numerical methodology to shells has received a limited attention. Similarly to PF for solids, the variational formalism for cracking shells encompasses the contribution to the total energy functional of the elastic and the fracture counterparts. In this concern, Amiri et al. (128) derived a PF model for thin shells via the adoption of the Kirchoff–Love

(3-parameter) kinematics via the local maximum entropy mesh-free method, whereas alternative PF formulations for shells can be found in (117; 129). However, to the best knowledge of the author, the PF shell models aforementioned are not locking-free. In order to remedy this aspect, Reinoso et al. (106) proposed a new modelling framework for solid shell model equipped with PF capabilities, which endowed the combined use of the EAS and the ANS for locking issues, and exhibited very promising results and robustness for large and small strain applications (130; 131).

Stemming from the previous arguments, in this work, we propose a new formulation to simulate fracture of functionally graded (FG) power-based shells. In the model herein proposed, the phase field approach to brittle fracture is employed in combination with a 6-parameter shell kinematic description for the structural model. Moreover, as recalled above, the present model integrates two methods to alleviate locking pathologies: the Enhanced Assumed Strain (EAS) method and the Assumed Natural Strain (ANS) method (116), rendering a locking-free finite element formulation. Finally, the proposed approach also accounts for the spatial variation along the thickness direction of the elastic and fracture properties as well as the phase field length scale (132).

1.6 Outline

In this section an outline of each chapter is provided. The current dissertation is organized into nine chapters as follows:

Chapter 2 outlines the basic concepts of continuum mechanics. In Section 2.1 the basic kinematic parameters are explained. In Section 2.2 the elements transformations from the reference to the current configuration are detailed. Moreover, in Section 2.3 and 2.4, the formulation of several strain and stress tensors are presented while in Section 2.5, the balance principles of continuum thermo-mechanics are exposed. Finally, the initial boundary value problem is analysed in Section 2.6 while the finite element method is explained in Section 2.7.

Chapter 3 addresses the fundamental aspects of fracture mechanics. In Section 3.1 the crack opening modes are exposed. After that, a review on fracture mechanics is done. Particularly, in Section 3.2 the assumptions, models and basic concepts of classical fracture mechanics are explained. However, in Section 3.3 the recent and advanced methods for fracture mechanics are summarized.

In Chapter 4, the phase field approach for brittle fracture is presented.

The fundamental concepts of phase field are explained in Section 4.1 while the formulation and implementation of this model in solids and shells is addressed in Section 4.2 and 4.3, respectively. Finally, in Section 4.4, the extension of the phase field to functionally graded shells is described.

In Chapter 5, the cohesive zone models used in this work are described. In Section 5.1, a new cohesive zone model (tension cut-off law) compatible with phase field is presented while in Section 5.2 we can find other cohesive zone model (bi-linear traction-separation law) which is uncoupled with phase field.

Chapter 6 addresses the simulation of fracture events in long-fiber reinforced composites. In particular, in Section 6.1, we can find some preliminary experimental results. After that, in Section 6.2, the single-fiber problem is investigated. Finally, in Section 6.3, simulations of fracture in cross ply laminates are exposed.

In Chapter 7, several simulations to understand and predict fracture in thin films on compliant substrates are carried out. In Section 7.1, 2D numerical simulations are presented while in Section 7.2, we find the 3D simulations results.

Chapter 8 presents the numerical simulations of functionally graded power-based shells performed. Particularly, in Section 8.1 a plate under tension is simulated while in Section 8.2 and 8.3, a cylindrical shell under different loads is solved.

Finally, the conclusions of this investigation and the future developments are addressed in Chapter 9.

Chapter 2

Fundamentals of continuum mechanics

This chapter contains a short introduction to continuum mechanics (CM) (133; 134; 135; 136; 137). It is worth mentioning that, CM is the part of mechanics devoted to the deformation and stress analysis of materials and structures which is characterized by the consideration of a particular body as a continuous system. In Section 2.1 the different mathematical aspects used by continuum mechanics to describe the motion of a material point are exposed. Moreover, the basic kinematic parameters and concepts are explained. In Section 2.2 the transformations of different elements from the reference to the current configuration are addressed. After that, the strain and stress tensors are formulated in Section 2.3 and 2.4, respectively. The conservation laws of thermo-mechanical problems are addressed in Section 2.5. Finally, the formulation of the initial boundary value problem and its weak form are presented in Section 2.6 while the finite element method is explained in Section 2.7.

2.1 Kinematics

Lets consider a material body whose initial configuration is denoted by $\mathcal{B}_0 \equiv \boldsymbol{\chi}_{t_0}(\mathcal{B}) \subset \mathbb{R}^3$ and whose material points are identified by vectors $\mathbf{X} := \boldsymbol{\chi}_{t_0}(P) \in \mathcal{B}_0$. This reference configuration is assumed to be undistorted and stress-free. This material body, after the deformation process

at an arbitrary time t, occupies a new position $\mathcal{B}_t \equiv \boldsymbol{\chi}_{t_t}(\mathcal{B}) \subset \mathbb{R}^3$, see Figure 11.

The reference and the current configurations are related using the nonlinear deformation map $\boldsymbol{\varphi} : \mathcal{B}_0 \times [0,t] \to \mathbb{R}^3$, where $[0,t]$ refers to the time interval elapsed in such that $\mathbf{X} \in \mathcal{B}_0$ are mapped onto the current material points $\mathbf{x} \in \mathcal{B}_t$, i.e. $\mathbf{x} = \boldsymbol{\varphi}(\mathbf{X}, t)$. Moreover, the absolute temperature $\vartheta : \mathcal{B}_0 \times [0,t] \to \mathbb{R}_+$ is assumed to be a smooth function of $(\mathbf{X}, t) \in \mathcal{B}_0 \times [0,t]$.

Accordingly, one defines the standard displacement vector as: $\mathbf{u} := \mathbf{x} - \mathbf{X}$.

The displacement of the material point P (p in the current configuration) is defined as:

$$\mathbf{u}(\mathbf{X}, t) := \mathbf{x}(\mathbf{X}, t) - \mathbf{X} \tag{2.1}$$

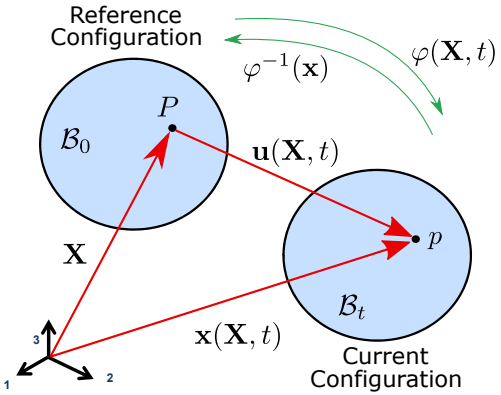

Figure 11: Reference and current configuration of a material body.

In order to determine the motion of a material point, two different mathematical descriptions are used: the Lagrangian or Material description and the Eulerian or Spatial description. While in the Lagrangian description all the magnitudes are referred to the initial configuration **X**, in the Eulerian formulation they are referred to the current configuration **x**.

To measure deformation in continuum mechanics, the so-called Deformation Gradient tensor **F** is defined. It relates quantities before and after the deformation and its definition is given by the following equa-

tion:

$$\mathbf{F} := \nabla_{\mathbf{X}} \boldsymbol{\varphi} = \frac{\partial \boldsymbol{\varphi}(\mathbf{X}, t)}{\partial \mathbf{X}} = \frac{\partial \mathbf{x}(\mathbf{X}, t)}{\partial \mathbf{X}} \quad \rightarrow \quad \mathrm{d}\mathbf{x} = \mathbf{F}\mathrm{d}\mathbf{X} \tag{2.2}$$

where $\nabla_{\mathbf{X}}(\cdot)$ is the gradient of $(\cdot)$. Note that as given above, the deformation gradient can be seen as a linear map of the referential material element $d\mathbf{X}$ onto the spatial counterpart. In addition, taking into account Equation 2.1, we can arrive at an alternative expression:

$$\mathbf{F} = \frac{\partial(\mathbf{u} + \mathbf{X})}{\partial \mathbf{X}} = \mathbf{I} + \frac{\partial \mathbf{u}}{\partial \mathbf{X}} = \mathbf{I} + \nabla_{\mathbf{X}}(\mathbf{u}) \tag{2.3}$$

being $\nabla_{\mathbf{X}}$ the gradient with respect to the material configuration.

The Deformation Gradient tensor admits the so-called polar decomposition, which is given by:

$$\mathbf{F} = \mathbf{R}\mathbf{U} = \mathbf{V}\mathbf{R} \tag{2.4}$$

where $\mathbf{R}$ is the rotation tensor, $\mathbf{U}$ is the right stretch tensor and $\mathbf{V}$ is the left stretch tensor. This is known as polar decomposition theorem. To highlight that, $\mathbf{U}$ is defined in the reference configuration while $\mathbf{V}$ is defined in the current configuration.

2.2 Transformation of elements of line, area and volume

In order to transform elements from the reference to the current configuration and vice versa, the Deformation Gradient tensor $\mathbf{F}$ is herewith exploited. The transformation of line elements obeys the following expressions:

$$\mathrm{d}\mathbf{x} = \mathbf{F}\mathrm{d}\mathbf{X} \rightarrow \text{Push–forward of } \mathrm{d}\mathbf{X} \tag{2.5}$$

$$\mathrm{d}\mathbf{X} = \mathbf{F}^{-1}\mathrm{d}\mathbf{x} \rightarrow \text{Pull–back of } \mathrm{d}\mathbf{x} \tag{2.6}$$

The transformation of elements of area, between the reference and current configurations renders:

$$\mathrm{d}\mathbf{A} := \mathrm{d}\mathbf{X}_1 \times \mathrm{d}\mathbf{X}_2 \qquad \mathrm{d}\mathbf{a} := \mathrm{d}\mathbf{x}_1 \times \mathrm{d}\mathbf{x}_2 \tag{2.7}$$

The cofactor of the deformation gradient tensor, $\mathrm{cof}\,[\mathbf{F}]$, is used:

$$\mathrm{d}\mathbf{a} = \mathbf{F}\mathrm{d}\mathbf{X}_1 \times \mathbf{F}\mathrm{d}\mathbf{X}_2 = \mathrm{cof}\,[\mathbf{F}]\,\mathrm{d}\mathbf{A} \tag{2.8}$$

Finally, the transformation of volume elements is expressed as in Equation 2.9, whereby the Jacobian of the motion J is exploited:

$$\mathrm{d}V := [\mathrm{d}\mathbf{X}_1 \times \mathrm{d}\mathbf{X}_2] \cdot \mathrm{d}\mathbf{X}_3 \qquad \mathrm{d}v := [\mathrm{d}\mathbf{x}_1 \times \mathrm{d}\mathbf{x}_2] \cdot \mathrm{d}\mathbf{x}_3 \tag{2.9}$$

$$\mathrm{d}v = \det[\mathbf{F}]\,\mathrm{d}V = J\mathrm{d}V. \tag{2.10}$$

Note that the Jacobian of the transformation complies with: $\mathrm{J}(\mathbf{X}, t) := \det[\mathbf{F}] > 0$. Accordingly, we denote $\rho_0 = \mathrm{J}\rho$ and ρ as the density in the reference and current configurations, respectively.

2.3 Strain tensor definitions

In this section, different strain tensors are presented. To do so, let's consider two material particles (P and Q) being $\mathrm{d}\mathbf{X}$ the distance between them in the reference configuration. However, due to the deformation process, the separation distance in the current configuration is given by $\mathrm{d}\mathbf{x}$. See Figure 12 for clarification.

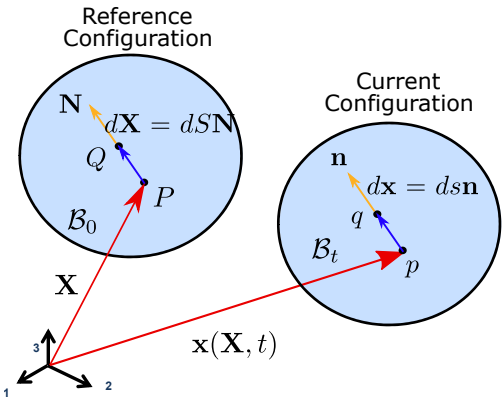

Figure 12: Transformation of line elements.

The Right Cauchy-Green tensor $\mathbf{C}$ is defined as follows:

$$\mathrm{d}s^2 = \mathrm{d}\mathbf{x} \cdot \mathrm{d}\mathbf{x} = \mathbf{F}\mathrm{d}\mathbf{X} \cdot \mathbf{F}\mathrm{d}\mathbf{X} = \mathrm{d}\mathbf{X}[\mathbf{F}^T\mathbf{F}]\mathrm{d}\mathbf{X} = \mathrm{d}\mathbf{X}\,[\mathbf{C}]\,\mathrm{d}\mathbf{X} \tag{2.11}$$

Considering the polar decomposition theorem exposed previously, the expression of $\mathbf{C}$ stays as follows:

$$\mathbf{C} = \left[\mathbf{F}^T\mathbf{F}\right] = [\mathbf{R}\mathbf{U}]^T\,\mathbf{R}\mathbf{U} = \mathbf{U}\mathbf{U} \tag{2.12}$$

However, if such scalar product is done in the reference configuration, we obtain the Left Cauchy-Green tensor **b**:

$$\mathrm{d}S^2 = \mathrm{d}\mathbf{X}\cdot\mathrm{d}\mathbf{X} = \mathbf{F}^1\mathrm{d}\mathbf{x}\cdot\mathbf{F}^{-1}\mathrm{d}\mathbf{x} = \mathrm{d}\mathbf{x}\left[\mathbf{F}^{-T}\mathbf{F}^{-1}\right]\mathrm{d}\mathbf{x} = \mathrm{d}\mathbf{x}\left[\mathbf{b}^{-1}\right]\mathrm{d}\mathbf{x} \quad (2.13)$$

$$\mathbf{b} = \left[\mathbf{F}\mathbf{F}^T\right] = \mathbf{V}\mathbf{R}\left[\mathbf{V}\mathbf{R}\right]^T = \mathbf{V}\mathbf{V} \quad (2.14)$$

Considering the difference of the squares of line elements in both configurations, see Equation 2.15, the corresponding stain tensors are defined via the computation of the following expression:

$$\mathrm{d}s^2 - \mathrm{d}S^2 = \mathrm{d}\mathbf{x}\cdot\mathrm{d}\mathbf{x} - \mathrm{d}\mathbf{X}\cdot\mathrm{d}\mathbf{X} \quad (2.15)$$

Thus, in the reference configuration, we can obtain the definition of the Green-Lagrange Strain tensor **E**:

$$\mathrm{d}s^2 - \mathrm{d}S^2 = \mathrm{d}\mathbf{X}\cdot\mathbf{C}\cdot\mathrm{d}\mathbf{X} - \mathrm{d}\mathbf{X}\cdot\mathrm{d}\mathbf{X} = \mathrm{d}\mathbf{X}\cdot\left[\mathbf{C}-\mathbf{I}\right]\cdot\mathrm{d}\mathbf{X} = 2\mathrm{d}\mathbf{X}\cdot\mathbf{E}\cdot\mathrm{d}\mathbf{X} \quad (2.16)$$

where:

$$\mathbf{E} = \frac{1}{2}\left[\mathbf{C}-\mathbf{I}\right] \quad (2.17)$$

However, if we operate in the same way but using the Left Cauchy-Green tensor **b** (see Equation 2.18), the new strain tensor given in Equation 2.19 is referred to the current configuration:

$$\mathrm{d}s^2 - \mathrm{d}S^2 = \mathrm{d}\mathbf{x}\cdot\mathrm{d}\mathbf{x} - \mathrm{d}\mathbf{x}\cdot\mathbf{b}^{-1}\cdot\mathrm{d}\mathbf{x} = \mathrm{d}\mathbf{x}\cdot\left[\mathbf{I}-\mathbf{b}^{-1}\right]\cdot\mathrm{d}\mathbf{x} = 2\mathrm{d}\mathbf{x}\cdot\mathrm{d}\mathbf{a}\cdot d\mathbf{x} \quad (2.18)$$

$$\mathbf{a} = \frac{1}{2}\left[\mathbf{I}-\mathbf{b}^{-1}\right] \quad (2.19)$$

being **a** the so-called Almansi Strain tensor.

2.4 Stress tensor definitions

In this section, several stress tensors defined with respect to different configurations are presented. Let's consider a cut off $\mathcal{C}_0 \subset \mathcal{B}_0$ in the reference configuration and other cut off $\mathcal{C}_t \subset \mathcal{B}_t$ in the current configuration. The boundaries of the previous cut offs are, respectively, $\partial\mathcal{C}_0$ and $\partial\mathcal{C}_t$ as we can see in Figure 13.

The interaction traction vector **t** at any material point on this arbitrary internal cut, also known as traction vector, acts on the area element da

and represent the force d**f**=**t**da on $\mathcal{C}_t$. The form of this traction vector is given by the Cauchy Lemma:

$$\mathbf{t}\mathrm{d}a = (\boldsymbol{\sigma}\mathbf{n})\,\mathrm{d}a = \boldsymbol{\sigma}\mathrm{d}\mathbf{a} \rightarrow \mathbf{t} := \boldsymbol{\sigma}\mathbf{n} \tag{2.20}$$

being $\boldsymbol{\sigma}$ the Cauchy stress tensor or the so-called true stress because it relates the actual force with the actual deformed area, in other words, it is related to the current configuration.

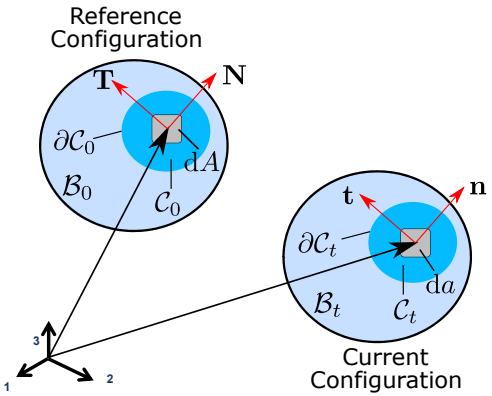

Figure 13: Definition of the stress tensor.

Taking into account that the differential of area can be expressed as follows:

$$\mathrm{d}\mathbf{a} = \det[\mathbf{F}]\,\mathbf{F}^{-T}\mathrm{d}\mathbf{A} \tag{2.21}$$

we arrive at a new expression:

$$\boldsymbol{\sigma}\mathrm{d}\mathbf{a} = \boldsymbol{\sigma}\det[\mathbf{F}]\,\mathbf{F}^{-T}\mathrm{d}\mathbf{A} = \mathbf{P}\mathrm{d}\mathbf{A} \tag{2.22}$$

being **P**, the first Piola-kirchhoff stress tensor which is is a two field tensor with one basis expressed in the reference configuration and the other one in the current configuration.

However, in order to obtain a stress tensor expressed in the reference configuration, it is necessary to apply the pull-back technique through the deformation gradient tensor **F** as follows:

$$\mathbf{S} = \mathbf{F}^{-1}\,\mathbf{P} \tag{2.23}$$

where **S** is the Second Piola-Kirchhoff Stress tensor and is defined in the reference configuration.

Finally, similarly to Cauchy Lemma, the Stokes heat flux takes the form:

$$q_n = \mathbf{q} \cdot \mathbf{n} \tag{2.24}$$

being q_n and **q** the scalar and vector heat flux on the current configuration (Cauchy), respectively. However, taking into account that the heat flux has to be the same in both configurations (see Equation 2.25), we arrive to the expression of the reference (first Piola-kirchhoff) heat flux vector **Q** given by Equation 2.26.

$$\mathbf{q} \cdot \mathrm{n} \mathrm{d}a = \mathbf{Q} \cdot \mathbf{N} \mathrm{d}A \tag{2.25}$$

$$\mathbf{Q} = J\mathbf{F}^{-1} \cdot \mathbf{q} \tag{2.26}$$

2.5 Conservation or balance laws

In this section, the conservation laws or balance principles of continuum thermo-mechanics, are presented. They have to be satisfied all the time in any particular material.

2.5.1 Conservation of mass

The mass of a continuum body cannot be modified by a deformation process for any arbitrary closed system. In other words, the mass of a continuum body remains constant before and after the deformation process. The conservation of mass, in the Lagrangian and Eulerian configurations, can be respectively written as:

$$\rho_0 = \mathrm{J}\rho; \quad \dot{\rho} + \rho \mathrm{div}\left[\mathbf{v}\right] = 0, \tag{2.27}$$

where $\mathrm{div}\left[\bullet\right]$ denotes the divergence with respect to the current setting and **v** is the spatial velocity.

2.5.2 Conservation of linear momentum

The change of linear momentum in time is equal to the sum of all the applied external forces acting on the continuum body. Therefore, the La-

grangian and Eulerian forms of this balance equation, respectively, read:

$$\rho_0 \dot{\mathbf{V}} = \mathrm{DIV}\left[\mathbf{P}\right] + \mathbf{F}_v = 0; \quad \rho \dot{\mathbf{v}} = \mathrm{div}\left[\boldsymbol{\sigma}\right] + \mathbf{f}_v = 0, \tag{2.28}$$

with $\mathrm{DIV}\left[\bullet\right]$ denoting the divergence with respect to the reference setting. $\dot{\mathbf{V}}$ and $\dot{\mathbf{v}}$ being, respectively, the material and spatial acceleration while $\mathbf{F}_v$ and $\mathbf{f}_v$ denote the body forces per unit of reference and current volume.

2.5.3 The conservation of energy

This conservation law governs the energy transformation in thermodynamic processes and it is also known as the first law of thermodynamics. Every continuum body interacts with its surroundings taking place an exchange of heat and work between them in a way that, the total energy of the body remains constant. The conservation of energy, in the Lagrangian and Eulerian configurations, takes the form:

$$\rho_0 \dot{e} = \mathbf{S} : \dot{\mathbf{E}} + R - \mathrm{DIV}\left[\mathbf{Q}\right]; \quad \rho \dot{e} = \boldsymbol{\sigma} : \mathbf{d} + r - \mathrm{div}\left[\mathbf{q}\right], \tag{2.29}$$

being e the specific internal energy, $\dot{\mathbf{E}}$ the material rate of $\mathbf{E}$ and $\mathbf{d}$ the deformation rate. Finally, R and r are the internal heat source per unit reference and current volume, respectively.

2.5.4 Entropy inequality

The first law of thermodynamics does not determine the direction of energy transfer. To solve this limitation, the second law of thermodynamics is introduced. It establishes that the total entropy of an isolated system is always positive. The Lagrangian and Eulerian expressions of this inequality, respectively, take the following form:

$$\rho_0 \dot{\eta} \geq \frac{R}{\vartheta} - \frac{1}{\vartheta}\mathrm{DIV}\left[\mathbf{Q}\right] + \frac{1}{\vartheta^2}\mathbf{Q}\cdot\nabla_{\mathbf{X}}\vartheta; \quad \rho\dot{\eta} \geq \frac{r}{\vartheta} - \frac{1}{\vartheta}\mathrm{div}\left[\mathbf{q}\right] + \frac{1}{\vartheta^2}\mathbf{q}\cdot\nabla_{\mathbf{x}}\vartheta, \tag{2.30}$$

where η is the specific entropy and $\nabla_{\mathbf{x}}\left(\cdot\right)$ the spatial gradient of $\left(\cdot\right)$.

Alternative expressions for the second law of thermodynamics in the reference and current configurations are given in Equation 2.31 thanks to

the introduction of Helmholtz free energy function ψ through the Legendre transformation: $\psi = e - \vartheta\eta$.

$$\mathbf{S} : \dot{\mathbf{E}} - \rho_0 \left(\dot{\psi} + \dot{\vartheta}\eta\right) - \frac{1}{\vartheta}\mathbf{Q}\cdot\nabla_{\mathbf{X}}\vartheta \geq 0; \quad \boldsymbol{\sigma} : \mathbf{d} - \rho \left(\dot{\psi} + \dot{\vartheta}\eta\right) - \frac{1}{\vartheta}\mathbf{q}\cdot\nabla_{\mathbf{x}}\vartheta \geq 0. \tag{2.31}$$

Note that based on empirical evidences $-\frac{1}{\vartheta}\mathbf{Q}\cdot\nabla_{\mathbf{X}}\vartheta \geq 0$ and $-\frac{1}{\vartheta}\mathbf{q}\cdot\nabla_{\mathbf{x}}\vartheta \geq 0$, indicate the direction of heat flow. Therefore, the Equation 2.31 takes a new form:

$$D_{\text{int}} := \mathbf{S} : \dot{\mathbf{E}} - \rho_0(\dot{\psi} + \dot{\vartheta}\eta) \geq 0; \quad D_{\text{int}} := \boldsymbol{\sigma} : \mathbf{d} - \rho(\dot{\psi} + \dot{\vartheta}\eta) \geq 0 \tag{2.32}$$

where D_{int} is the internal dissipation and has to be always positive.

Finally introducing D_{int} into Equation (2.29), the balance equations read:

$$\rho_0\vartheta\dot{\eta} = D_{\text{int}} + R - \text{DIV}\left[\mathbf{Q}\right]; \quad \rho\vartheta\dot{\eta} = D_{\text{int}} + r - \text{div}\left[\mathbf{q}\right]. \tag{2.33}$$

2.6 Initial boundary value problem (IBVP)

This section introduces the formulation of the IBVP for coupled thermo-mechanical problems (see Figure 14) and its weak formulation.

2.6.1 Formulation of the IBVP

The balance equation of linear momentum in terms of the reference coordinates $\mathbf{X} \in \mathcal{B}_0$ given in Equation (2.28) renders:

$$\text{DIV}\left[\mathbf{P}\right] + \mathbf{F}_v = 0 \text{ in } \mathcal{B}_0. \tag{2.34}$$

While, the energy balance in the Lagrangian description given in Equation 2.29 reads:

$$\rho_0\dot{e} = \mathbf{S} : \dot{\mathbf{E}} + R - \text{DIV}\left[\mathbf{Q}\right] \text{ in } \mathcal{B}_0. \tag{2.35}$$

Introducing the second law of the thermodynamics given in Equation (2.33):

$$\rho_0\vartheta\dot{\eta^e} = D_{\text{int}}^{\text{mech}} - \text{DIV}\left[\mathbf{Q}\right] + R, \tag{2.36}$$

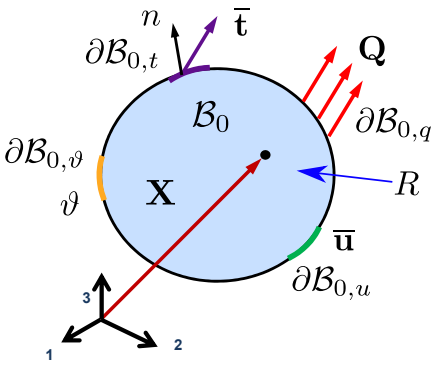

Figure 14: Thermo-mechanical problem of an arbitrary body.

and defining $\rho_0 \vartheta \dot{\eta^e} = c_p \dot{\vartheta} + \mathcal{H}$, the Equation (2.36) can be change to:

$$c_p \dot{\vartheta} = D_{\text{int}}^{\text{mech}} - \text{DIV}\left[\mathbf{Q}\right] + R - \mathcal{H}, \tag{2.37}$$

being c_p the specific heat capacity at constant deformation, $\mathcal{H}$ the structural heating or cooling and $D_{\text{int}}^{\text{mech}}$ the mechanical counterpart of the internal dissipation D_{int}.

2.6.2 Weak formulation

In this section, the weak form of the coupled thermo-mechanical IBVP is presented. It is worth mentioning that, the construction of the weak form, is used to perform the corresponding numerical approximation based on FEM.

Let's consider an arbitrary body $\mathcal{B}_0$ in the reference configuration whose boundary $\partial\mathcal{B}_0$ is subdivided into several disjointed parts corresponding to different sub-problems (mechanical and thermal) as we can see in Figure 14: $\partial\mathcal{B}_{0,u} \subset \partial\mathcal{B}_0$ and $\partial\mathcal{B}_{0,t} \subset \partial\mathcal{B}_0$, with $\partial\mathcal{B}_0 = \partial\mathcal{B}_{0,u} \cup \partial\mathcal{B}_{0,t}$ and $\partial\mathcal{B}_{0,u} \cap \partial\mathcal{B}_{0,t} = \emptyset$ corresponding to the mechanical sub-problem, and $\partial\mathcal{B}_{0,\vartheta} \subset \partial\mathcal{B}_0$ and $\partial\mathcal{B}_{0,q} \subset \partial\mathcal{B}_0$, with $\partial\mathcal{B}_0 = \partial\mathcal{B}_{0,\vartheta} \cup \partial\mathcal{B}_{0,q}$ and $\partial\mathcal{B}_{0,\vartheta} \cap \partial\mathcal{B}_{0,q} = \emptyset$ corresponding to the thermal sub-problem.

The weak form of the linear momentum balance Equation (2.34) obtained through the standard Galerkin procedure, reads:

$$G^{u}\left(\mathbf{u},\vartheta,\delta\mathbf{u}\right)=\int_{\mathcal{B}_0}\mathbf{P}:\nabla_{\mathbf{X}}\delta\mathbf{u}\mathrm{dV}-\int_{\partial\mathcal{B}_0}\delta\mathbf{u}\cdot\left(\mathbf{P}\cdot\mathbf{N}\right)\mathrm{dA}-\int_{\mathcal{B}_0}\mathbf{F}_{v}\cdot\delta\mathbf{u}\mathrm{dV}, \tag{2.38}$$

being $\delta\mathbf{u}$ the virtual displacement. Following the same procedure as before, but for the energy balance equation given in (2.37), the result is the following :

$$G^{\vartheta}\left(\mathbf{u},\vartheta,\delta\vartheta\right)=\int_{\mathcal{B}_0}\left(\mathcal{D}_{\mathrm{int}}^{\mathrm{mech}}-\mathrm{DIV}\left[\mathbf{Q}\right]+R-\mathcal{H}-c_{p}\dot{\vartheta}\right)\delta\vartheta\mathrm{dV}=0, \tag{2.39}$$

where $\delta\vartheta$ is the virtual temperature. Introducing the Divergence Theorem:

$$\int_{\mathcal{B}_0}\mathrm{DIV}\left[\mathbf{Q}\right]\delta\vartheta\mathrm{dV}=\int_{\partial\mathcal{B}_0}\mathbf{Q}\cdot\mathbf{N}\delta\vartheta\mathrm{dA}-\int_{\mathcal{B}_0}\mathbf{Q}\cdot\nabla_{\mathbf{X}}\delta\vartheta\mathrm{dV}. \tag{2.40}$$

we arrive to a new expression for the weak form of the energy balance:

$$\begin{aligned}G^{\vartheta}\left(\mathbf{u},\vartheta,\delta\vartheta\right)=&\int_{\mathcal{B}_0}\mathcal{D}_{\mathrm{int}}^{\mathrm{mech}}\delta\vartheta\mathrm{dV}+\int_{\mathcal{B}_0}R\delta\vartheta\mathrm{dV}-\int_{\mathcal{B}_0}\mathcal{H}\delta\vartheta\mathrm{dV}-\int_{\mathcal{B}_0}c_{p}\dot{\vartheta}\delta\vartheta\mathrm{dV}\\&+\int_{\mathcal{B}_0}\mathrm{J}\mathbf{q}\cdot\nabla_{\mathbf{x}}\delta\vartheta\mathrm{dV}-\int_{\partial\mathcal{B}_0}Q_{n}\delta\vartheta\mathrm{dA}=0,\end{aligned} \tag{2.41}$$

To highlight that, Q_n represents the scalar reference surface heat flux and is defined as: $Q_n=\mathbf{Q}\cdot\mathbf{N}$.

2.7 The finite element method

In this section, the numerical method known as finite element method (FEM) is outlined. This numerical method is used to solve the initial boundary value problem (IBVP) previously introduced. For more information about the FEM, the reader is referred to (138; 139).

2.7.1 Weak formulation and linearization of the equilibrium equations

The weak form of the equilibrium equations in the current configuration adopts the form:

$$G(\mathbf{u},\mathbf{v}) = \int_{\Omega} \sigma : \mathrm{grad}\mathbf{v}\,\mathrm{dV} - \int_{\partial\Omega} \mathbf{t}\cdot\mathbf{v}\,\mathrm{dA} - \int_{\Omega} \mathbf{F}_v \cdot \mathbf{v}\,\mathrm{dV} \tag{2.42}$$

where $\mathbf{u}$ is the solution or real displacement and $\mathbf{v}$ is the virtual displacement. It can be noticed the nonlinear character of the previous equation. Therefore, the linearization of the weak formulation through the Taylor series expansion is performed as follows:

$$G(\mathbf{u}+\epsilon\mathbf{w},\mathbf{v}) = G(\mathbf{u},\mathbf{v}) + \left.\frac{\mathrm{d}G(\mathbf{u}+\epsilon\mathbf{w},\mathrm{v})}{\mathrm{d}\epsilon}\right|_{\epsilon=0} \cdot \mathbf{w} + \mathbf{R}_n \tag{2.43}$$

being:

$$\begin{aligned}
\left.\frac{\mathrm{d}G(\mathbf{u}+\epsilon\mathbf{w},\mathrm{v})}{\mathrm{d}\epsilon}\right|_{\epsilon=0} &= \delta G(\mathbf{u},\mathbf{v},\mathbf{w}) \\
&= \lim_{\epsilon\to 0} \frac{G(\mathbf{u}+\epsilon\mathbf{w},\mathbf{v}) - G(\mathbf{u},\mathbf{v})}{\epsilon} \\
&= \left.\frac{\mathrm{d}G(\mathbf{u}+\epsilon\mathbf{w})}{\mathrm{d}\epsilon}\right|_{\epsilon=0} \\
&= \int_{\Omega} \left.\frac{\mathrm{d}\sigma(\mathbf{u}+\epsilon\mathbf{w})}{\mathrm{d}\epsilon}\right|_{\epsilon=0} : \varepsilon(\mathbf{w})\,\mathrm{dV} \\
&= \int_{\Omega} \left.\frac{\mathrm{dF}(\varepsilon(\mathbf{u}+\epsilon\mathbf{w}))}{\mathrm{d}\epsilon}\right|_{\epsilon=0} : \varepsilon(\mathbf{v})\,\mathrm{dV} \\
&= \int_{\Omega} \left.\frac{\partial \mathrm{F}(\varepsilon(\mathbf{u}+\epsilon\mathbf{w}))}{\partial\varepsilon(\mathbf{u}+\epsilon\mathbf{w})}\right|_{\epsilon=0} \left.\frac{\mathrm{d}\varepsilon(\mathbf{u}+\epsilon\mathbf{w})}{\mathrm{d}\epsilon}\right|_{\epsilon=0} : \varepsilon(\mathbf{v})\,\mathrm{dV} \\
&= \int_{\Omega} \mathbb{C}(\mathbf{u}) : \varepsilon(\mathbf{w}) : \varepsilon(\mathbf{v})\,\mathrm{dV}
\end{aligned} \tag{2.44}$$

where $\mathrm{F}(.)$ stands for the Gateaux differentiable of the corresponding variable and $\mathbb{C}(\mathbf{u})$ is the tangential material stiffness tensor.

2.7.2 Spatial discretization

For the numerical solution of the previous PDE, the FEM is used. Therefore, the domain of a continuous body Ω is decomposed into small subregions Ω_e known as finite elements (see Figure 15), allowing an approximation of the continuous body by a discretized domain Ω_h as follows:

$$\Omega \approx \Omega_h = \bigcup_{i=1}^{ne} \Omega_e \tag{2.45}$$

where ne is the number of subregions or finite elements.

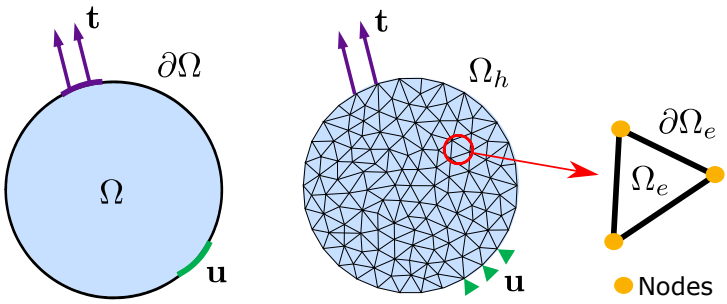

Figure 15: Discretization of a continuous body Ω by finite elements Ω_e.

The geometry and displacement of each finite element is interpolated between discrete points within the finite element called nodes. The interpolations are made by the shape functions N_I. It is worth mentioning that, due to the isoparametric concept, the interpolation functions used for the displacements and the geometry, see Equations 2.46 and 2.47, are identical.

$$\mathbf{u}_h(x) = \sum_{I=1}^{n} N_I(x)\mathbf{u}_I \qquad \forall\ \mathbf{x} \text{ in } \Omega_e \tag{2.46}$$

$$\mathbf{x}_h = \sum_{I=1}^{n} N_I \mathbf{x}_I \qquad \forall\ \mathbf{x} \text{ in } \Omega_e \tag{2.47}$$

Neglecting the body forces $\mathbf{F}_v$ and taking into account that the discretized form of the integrals over the domain are given by the following expression:

$$\int_{\Omega} (\cdot)\, \mathrm{dV} \approx \int_{\Omega_h} (\cdot)\, \mathrm{dV} = \bigcup_{i=1}^{ne} \int_{\Omega_e} (\cdot)\, \mathrm{dV} \tag{2.48}$$

The continuous and discretized forms of the equilibrium equation introduced in 2.42, stay as follows:

$$
\begin{aligned}
G\left(\mathbf{u},\mathbf{v}\right) &= \int_{\Omega} \boldsymbol{\sigma} : \delta\varepsilon \,\mathrm{dV} - \int_{\partial\Omega^t} \mathbf{t}\cdot\mathbf{v}\,\mathrm{dA} = 0 \\
&\approx \bigcup_{i=1}^{ne}\sum_{I=1}^{n} \mathbf{v}_I^T \int_{\Omega_e} \mathbf{B}_I^T\boldsymbol{\sigma}\,\mathrm{dV} - \bigcup_{i=1}^{ne}\sum_{I=1}^{n}\mathbf{v}_I^T\int_{\partial\Omega^t}\mathbf{t}N_I\,\mathrm{dA} \\
&= \bigcup_{i=1}^{ne}\sum_{I=1}^{n}\mathbf{v}_I^T\mathbf{R}_I - \bigcup_{i=1}^{ne}\sum_{I=1}^{n}\mathbf{v}_I^T\mathbf{P}_I \\
&= \mathbf{v}^T\mathbf{R} - \mathbf{v}^T\mathbf{P}
\end{aligned}
\tag{2.49}
$$

being $\mathbf{B}_I$ the matrix containing the derivatives of the shape functions (N_I), $\mathbf{R}_I$ and $\mathbf{P}_I$ the internal and external nodal forces, respectively and finally $\mathbf{R}$ and $\mathbf{P}$, the global internal and external force vectors.

The discretized strain variables are given by:

$$
\varepsilon(\Delta\mathbf{u}) = \Delta\varepsilon(\mathbf{u}) = \sum_{I=1}^{n}\mathbf{B}_I\Delta\mathbf{u}_I, \quad \varepsilon(\mathbf{v}) = \sum_{I=1}^{n}\mathbf{B}_I\mathbf{v}_I \tag{2.50}
$$

Therefore, the discrete linearized formulation of the equilibrium equations takes the following form:

$$
\begin{aligned}
\delta G(\mathbf{u},\mathbf{v},\Delta\mathbf{u}) &= \int_{\Omega}\mathbb{C}(\mathbf{u})\Delta\varepsilon(\mathbf{u})\varepsilon(\mathbf{v})\,\mathrm{dV}\,\Delta\mathbf{u} \\
&\approx \bigcup_{i=1}^{ne}\sum_{I=1}^{n}\sum_{J=1}^{n}\mathbf{v}_I^T\int_{\Omega^e}\mathbf{B}_I^T\mathbb{C}\mathbf{B}_J\,\mathrm{dV}\,\Delta\mathbf{u}_J \\
&= \bigcup_{i=1}^{ne}\sum_{I=1}^{n}\sum_{J=1}^{n}\mathbf{v}_I^T\mathrm{K}_{IJ}^e\,\Delta\mathbf{u}_J
\end{aligned}
\tag{2.51}
$$

Where K_{IJ}^e is the element stiffness matrix which connects the nodes I and J of a finite element and $\Delta\mathbf{u}$ is an incremental increase of the solution $\mathbf{u}$. Finally, it should be mention that the global stiffness K is obtained assembling the element stiffness matrices as follows:

$$
\mathrm{K} = \bigcup_{i=1}^{ne}\mathrm{K}^e \tag{2.52}
$$

Chapter 3

Fundamentals of fracture mechanics

Fracture mechanics (FM) is the field of mechanics concerned with the study of the onset and growth of cracks in materials. This discipline has attracted a huge interest in many industrial sectors over the last decades involving bio-mechanics, aerospace, automotive, electronics, etc.

This chapter is devoted to present the fundamental aspects and concepts of fracture mechanics. The organization of the present chapter is as follows. In Section 3.1, the conceptual identification of the fracture modes are explained, whereas in Section 3.2 the classical fracture mechanics models are exposed. Finally, in Section 3.3 more recent and advanced models are addressed.

3.1 Fracture modes

A crack opening or the relative displacement between crack edges can be described as the combination of 3 failure modes (See Figure 16):

Mode I or opening mode: it is due to a normal stress to the fracture plane.

Mode II or sliding mode: it arises when there is a shear stress in the fracture plane.

Mode III or tearing mode: it happens when there is a shear stress in a plane different to the fracture plane.

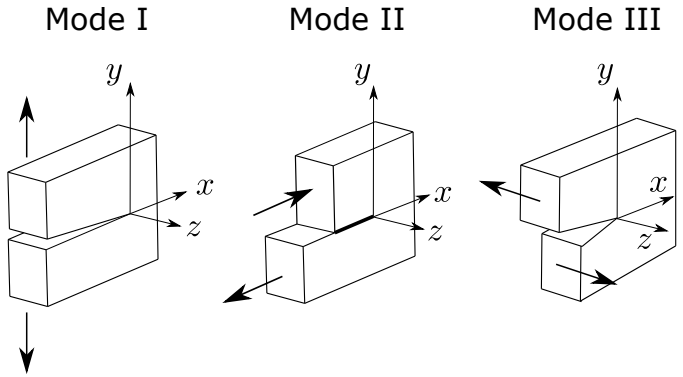

Figure 16: Fracture modes.

3.2 Classical fracture mechanics

Fracture mechanics is usually divided into linear elastic fracture mechanics (LEFM) and nonlinear fracture mechanics (NLFM). The first one uses linear elasticity and is appropriated for brittle fracture. In contrast, NLFM is used in fracture processes which are dominated by inelastic material behaviour. In other words, when the material presents an elasto-plastic behaviour. For that reason, NLFM is commonly known as elasto-plastic fracture mechanics (EPFM).

3.2.1 Linear elastic fracture mechanics

The first investigation was made by Inglis (140). In his seminal studies, this author analyzed an infinite plane with an elliptical hole subjected to a constant remote stress (Figure 17). The stress around the crack tip, location A, is given by the expression:

$$\sigma_A = \sigma \left(1 + \frac{2a}{b} \right) \tag{3.1}$$

which means that, in the case of a sharp crack (b $\rightarrow$ 0) the stress diverges ($\sigma \rightarrow \infty$). Therefore, it was no possible to establish a stress criterion for crack propagation.

After that, Griffith introduced the basis of modern fracture mechanics

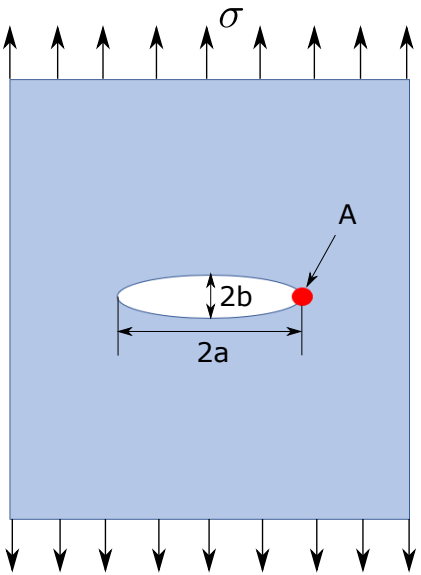

Figure 17: Infinite plane with a central elliptical hole under tension.

with an energetic vision, who established an energy balance criterion for crack propagation (141):

$$U_t = U_i - U_a - U_w + U_\gamma \tag{3.2}$$

being U_t the total elastic energy of the cracked body, U_i the initial strain energy of the uncracked body, U_a the elastic energy release due to the introduction of the crack, U_w the work made by external loadings and U_γ the increase of the surface energy as a consequence of the new crack creation. Therefore, a crack will propagate if the energy released upon crack growth is sufficient to provide the energy necessary for creating new free surfaces.

Subsequently, Irwin was able to compute the stress field around the crack tip (142), who considered that fracture is presented in a small area near the crack tip (plastic zone) instead of considering it concentrated in a single point (crack tip). Therefore, a stress criterion for crack propagation and the concept of stress intensity factor K were introduced.

Finally, to mention the limitations of LEFM: it is necessary the exis-

tence of a pre-existing defect and only applies to brittle materials.

3.2.2 Elasto-plastic fracture mechanics

Elasto-plastic fracture mechanics (EPFM) is an extension of LEFM. It is used when the material develops a significant plasticity near the crack tip arising the plastic zone. To remark that, although the plastic zone concept was introduced previously by Irwin (142), the plastic zone was sufficiently small compared to the specimen dimensions, which means that it could be considered as negligible.

The dimension and shape (143) of this plastic zone depends on the material properties, the geometry of the problem, the loading conditions and also on the crack length. One of the first estimations of the plastic zone length under Mode I and plane stress conditions was:

$$d_e = \frac{1}{2\pi}\left(\frac{K_I}{\sigma_{yy}}\right)^2 \tag{3.3}$$

where K_I is the stress intensity factor in Mode I and σ_{yy} the yield stress. This calculation was made considering a perfect plastic behaviour and it was based on an elastic crack-tip solution. For that reason, some authors as Irwin (144) or Dugdale (145) introduced corrections of the plastic zone length.

Among the potential fracture criteria used in EPFM, the main ones are: crack tip opening displacement (CTOD) (146) and J-integral (147). Although these models are widely used, they cannot predict the crack onset.

3.3 Advanced methods for fracture mechanics

Apart from the models mentioned in the previous sections, finite fracture mechanics (FFM) and cohesive zone models (CZMs) are widely used and both of them can predict the crack onset.

FFM was proposed by Leguillon (148). This author used a coupled stress-energy criterion which means that, both criteria (stress and energy criterion), have to be fulfilled simultaneously for the onset and growth of the crack. Owing to its solid theoretical roots, FFM can predict the crack onset, in other words, does not need the existence of an initial crack, because an instantaneous formation of cracks of finite size is assumed. This tool have been widely used in the literature, See (31; 149; 150).

Alternative methodologies for the prediction of fracture events in solids and interfaces are CZMs, which have been extensively exploited in the last decades (151; 152; 153). These models consider two crack tips: one

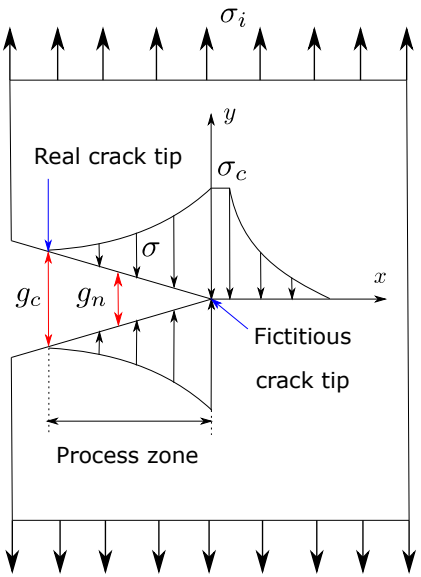

Figure 18: CZM.

fictitious and other real, being the distance between them known as process zone. In CZM when the surfaces of an interface separate, traction increases until a maximum σ_c (fictitious crack tip) and then progressively reduces to zero (real crack tip) resulting a complete separation as we can see in Figure 18. A detailed description of CZMs and its combination with phase field methods is given in Chapter 5.

Note that, all these models based on fracture mechanics have problems representing the crack opening and predicting the crack propagation. Therefore, remeshing techniques, the extended finite element methods (XFEM) (154), the enhanced finite element method (EFEM) (155) and algorithms to track the crack path are needed. However, these techniques still present problems in 3D applications. To solve this situation, smeared crack models emerged. It is worth mentioning that, the XFEM is an extension of the traditional finite element method based on the concept of

the partition of unity. It enriches the degrees of freedom using special displacement functions in order to allow discontinuities in an element. In other words, a crack within an element can be described. Conversely, the EFEM is very similar to XFEM but in that case the enrichment is accomplished in the strain space by adding a set of incompatible modes which allows crack representation.

Finally, with regard to the smeared crack models, one of the most prominent methods is the so-called phase field (PF) approach of brittle fracture (40; 156; 157), which is rooted on the Griffith theory. The PF model considers that the damage does not depend on a single point (discrete crack), depends on the stress field near to the point considered (diffusive crack). Therefore, although PF methods exploit fracture mechanics concepts, damage is envisaged in a diffusive fashion instead of using strong discontinuous formulations. This fact allows the preclusion of tracking the crack path or to remeshing techniques as the crack propagates. Moreover, it is a non-local damage model so pathological mesh dependency is reduced.

Due to all the previous advantages in conjunction with its capacity of capturing very complex crack paths and also to its inherent versatility, the phase field model has been widely developed over the last decade and will be a matter of use in this dissertation in high-tech components (long-fiber reinforced composites, FGMs, shells and thin film-substrate structures) and on different length scales. Consequently, a more comprehensive description of this method is outlined in the forthcoming chapter.

Chapter 4

Phase field model for brittle fracture

In this chapter, the basic concepts of the phase field (PF) approach of fracture (156) are presented in Section 4.1. Moreover, the formulation and implementation of this model in different elements, such as solids and shells, has been exposed in Section 4.2 and 4.3, respectively. Finally, in Section 4.4, the extension of the phase field model to functionally graded materials is discussed. Contents of the present chapter are based on the research papers (15; 16; 77; 78).

4.1 Theoretical concepts of the phase field model

In order to introduce the basic aspects of the PF approach of fracture in a multi-dimensional (2D or 3D) framework, we refer to an arbitrary solid in the Euclidean space $\mathbb{R}^n$, which is identified by $\mathcal{B} \subset \mathbb{R}^n$, where n is the dimension of the analysis. A material point within the domain in the Cartesian setting is given by the position vector $\mathbf{x}$. Body actions are denoted by the vector $\boldsymbol{f}_{\mathrm{v}} : \mathcal{B} \longrightarrow \mathbb{R}^n$. The boundary of the solid $\mathcal{B}$ is identified by $\partial\mathcal{B} \subset \mathbb{R}^{n-1}$, which is split into the boundary portions whereby the kinematic and static actions are prescribed, namely the regions $\partial\mathcal{B}_{\mathrm{u}}$ and $\partial\mathcal{B}_{\mathrm{t}}$, respectively, which are characterized by the corresponding fields $\overline{\mathbf{u}}$ and $\overline{\mathbf{t}}$. These parts of the body boundary fulfill the standard conditions: $\partial\mathcal{B}_t \cup \partial\mathcal{B}_u = \partial\mathcal{B}$ and $\partial\mathcal{B}_t \cap \partial\mathcal{B}_u = \emptyset$. Therefore,

these prescribed actions can be expressed as:

$$\mathbf{u} = \overline{\mathbf{u}} \quad \text{on } \partial\mathcal{B}_u \quad \text{and} \quad \overline{\mathbf{t}} = \boldsymbol{\sigma} \cdot \mathbf{n} \quad \text{on } \partial\mathcal{B}_t \tag{4.1}$$

where $\mathbf{n}$ stands for the outer normal vector to the body.

The kinematics of the solid is characterized by the displacement field $\mathbf{u} : \mathcal{B} \rightarrow \mathbb{R}^n$. The Cauchy stress and the infinitesimal strain tensor fields are introduced as: $\boldsymbol{\sigma} : \mathcal{B} \rightarrow \mathbb{R}^{n\times n}$ and $\boldsymbol{\varepsilon} : \mathcal{B} \rightarrow \mathbb{R}^{n\times n}$. In the infinitesimal deformation setting, the strain field is defined as the symmetric part of the displacement gradient: $\boldsymbol{\varepsilon} := \nabla^s_{\mathbf{x}}\mathbf{u}$.

Rooted on the Griffith theory of fracture (141), the central aspect of the PF technique envisages a regularized crack representation of the sharp crack topology within a diffusive crack zone of width l, being l known as phase field length and given by the following equation (125; 126):

$$l = \frac{27E'\mathcal{G}_C}{256\sigma_c^2} \tag{4.2}$$

This regularization is characterized through the introduction of a damage-like scalar variable $\mathfrak{d} : \mathcal{B} \times [0, t] \longrightarrow [0, 1]$ (126), which triggers the progressive stiffness degradation upon fracture evolution. This regularization is schematically depicted in Figure 19 for a 1D problem (127; 156), and it is characterized by the length l which controls the transition between fully intact ($\mathfrak{d} = 0$) and broken ($\mathfrak{d} = 1$) states.

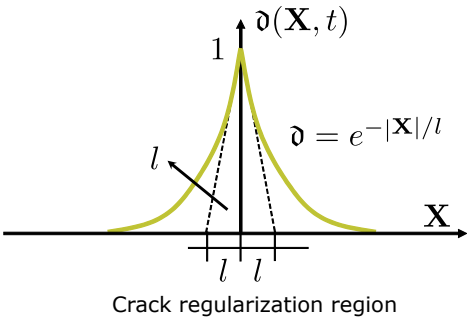

Figure 19: Diffusive crack at regularization. 1D problem at $x = 0$ depending on the length scale parameter l.

According to (156), the equations associated with the phase field prob-

lem in the bulk take the form:

$$\mathfrak{d} - l^2 \Delta \mathfrak{d} = 0 \quad \text{in } \mathcal{B} \quad \text{and} \quad \nabla_{\mathbf{x}} \mathfrak{d} \cdot \mathbf{n} = 0 \quad \text{in } \partial \mathcal{B} \tag{4.3}$$

whereby $\Delta \mathfrak{d}$ is the Laplacian of the variable $\mathfrak{d}$, and $\nabla_{\mathbf{x}} \mathfrak{d}$ stands for its spatial gradient.

The crack surface density functional $\gamma(\mathfrak{d}, \nabla_{\mathbf{x}} \mathfrak{d})$ accounting for the regularized crack topology is defined as:

$$\Gamma_c(\mathfrak{d}) := \int_{\mathcal{B}} \gamma(\mathfrak{d}, \nabla_{\mathbf{x}} \mathfrak{d}) \, \mathrm{d}\Omega \tag{4.4}$$

This functional endows the condition that Equation (4.4) converges to the sharp crack surface Γ_c for the limit $l \to 0$ in the spirit of the Γ-convergence concept. The particular form of $\gamma(\mathfrak{d}, \nabla_{\mathbf{x}} \mathfrak{d})$ herewith adopted is in line with that previously defined in (156):

$$\gamma(\mathfrak{d}, \nabla_{\mathbf{x}} \mathfrak{d}) = \frac{1}{2l} \mathfrak{d}^2 + \frac{l}{2} \left| \nabla_{\mathbf{x}} \mathfrak{d} \right|^2 \tag{4.5}$$

Moreover, by the virtue of the introduction of the previous functional, the crack-related integral in the original Griffith formulation can be approximated by the volume integral as follows:

$$\int_{\Gamma_c} \mathcal{G}_c \, \mathrm{d}\partial\Omega \approx \int_{\mathcal{B}} \mathcal{G}_c \gamma(\mathfrak{d}, \nabla_{\mathbf{x}} \mathfrak{d}) \, \mathrm{d}\Omega \tag{4.6}$$

Accordingly, the total energy functional of the solid reads (Figure 20):

$$\Pi(\mathbf{u}, \mathfrak{d}) = \int_{\mathcal{B}} \psi(\boldsymbol{\varepsilon}, \mathfrak{d}) \, \mathrm{d}\Omega + \int_{\mathcal{B}} \mathcal{G}_c \gamma(\mathfrak{d}, \nabla_{\mathbf{x}} \mathfrak{d}) \, \mathrm{d}\Omega + \Pi_{ext}(\mathbf{u}) \tag{4.7}$$

where the first term represents the elastic energy that is affected by the degradation variable, and the second term stands for the dissipated energy due to the crack evolution characterized by the fracture toughness $\mathcal{G}_c$ (both terms are arranged into the internal functional Π_{int} ($\mathbf{u}$, $\mathfrak{d}$); finally Π_{ext} ($\mathbf{u}$) accounts for the contribution of the external actions. Note that in the previous derivations, in a 2D setting, body and boundary integrals are associated with surface and line integrals, respectively. The corresponding extension to 3D analyses encompasses the evaluation of such terms over volume domains and crack-surface regions, respectively. One key aspect of this numerical technique is the fact that crack propagation results from the direct competition between the bulk and crack

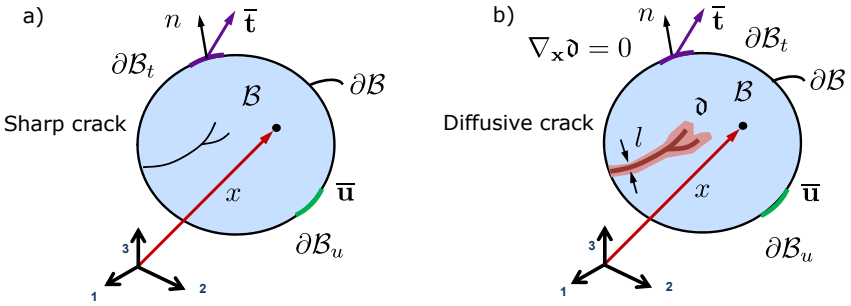

Figure 20: Phase field method for diffusive crack modeling for bulk fracture: representation for arbitrary bodies. a) identifies an arbitrary cracked body accounting for a discrete crack. b) identifies the regularized crack representation using the phase field approach of fracture

energy terms. The displacement and phase field are then determined by minimizing the energy functional given in Equation (4.7), which can be performed following either fully monolithic or a staggered solution schemes (127; 156). In order to prevent cracking in regions under compression states, the elastic energy term of the solid ($\psi(\boldsymbol{\varepsilon}, \mathfrak{d})$) admits the use of the spectral decomposition to split the traction and compression counterparts as follows (156):

$$\psi(\boldsymbol{\varepsilon}, \mathfrak{d}) = \mathfrak{g}(\mathfrak{d})\psi_+^e(\boldsymbol{\varepsilon}) + \psi_-^e(\boldsymbol{\varepsilon}), \tag{4.8a}$$

$$\psi_+^e(\boldsymbol{\varepsilon}) = \frac{\lambda}{2}\left(\langle \mathrm{tr}[\boldsymbol{\varepsilon}]\rangle_+\right)^2 + \mu \mathrm{tr}[\boldsymbol{\varepsilon}_+^2], \tag{4.8b}$$

$$\psi_-^e(\boldsymbol{\varepsilon}) = \frac{\lambda}{2}\left(\langle \mathrm{tr}[\boldsymbol{\varepsilon}]\rangle_-\right)^2 + \mu \mathrm{tr}[\boldsymbol{\varepsilon}_-^2], \tag{4.8c}$$

$$\boldsymbol{\varepsilon}_\pm = \sum_{i=1}^{ndim} 2^{-n} = \langle \varepsilon^i \rangle_\pm \boldsymbol{n}_\varepsilon^i \otimes \boldsymbol{n}_\varepsilon^i \tag{4.8d}$$

being λ y μ the Lamé constants; $\boldsymbol{\varepsilon}_+$ and $\boldsymbol{\varepsilon}_-$ respectively stand for the positive and negative parts of the infinitesimal strain tensor. The symbol tr[•] identifies the trace operator, whereas $\langle\bullet\rangle_\pm$ denotes the Macaulay bracket: $\langle\bullet\rangle_\pm = (\bullet \pm |\bullet|)/2$. The symbols ε^i and $\boldsymbol{n}_\varepsilon^i$ are, respectively, the eigenvalues and eigenvectors of the strain tensor. Note that alternative schemes such as the isochoric-volumetric decomposition can be also adopted in a straightforward manner. It is worth to clarify that, this decomposition into positive and negative parts is done because a crack cannot nucle-

ate or propagate under compressive loads. However, during the load history, material interpenetration can happen. Although the interpenetration problem is out of the scope of the present work, it should be very interesting to analyse in the future the preclusion of this phenomenon. A possible way can be the method proposed in (158).

The degradation function $\mathfrak{g}(\mathfrak{d})$ used in the present thesis reads:

$$\mathfrak{g}(\mathfrak{d}) = (1 - \mathfrak{d})^2 + \mathcal{K} \tag{4.9}$$

where $\mathcal{K}$ is a residual stiffness parameter to avoid computational instabilities.

Following standard thermodynamic arguments, the Cauchy stress tensor for the PF formulation can be expressed as:

$$\boldsymbol{\sigma} := \frac{\partial \hat{\psi}}{\partial \boldsymbol{\varepsilon}} = \mathfrak{g}(\mathfrak{d})\boldsymbol{\sigma}_+ + \boldsymbol{\sigma}_-; \qquad \text{with } \boldsymbol{\sigma}_\pm = \lambda \left(\langle \text{tr}[\boldsymbol{\varepsilon}] \rangle_\pm \right) \mathbf{1} + 2\mu \boldsymbol{\varepsilon}_\pm \tag{4.10}$$

being $\mathbf{1}$ the second order identify matrix, and $\boldsymbol{\sigma}_\pm$ denoting the positive and negative parts of $\boldsymbol{\sigma}$. Note that, alternative positive-negative decomposition schemes such as that proposed in (159) and (160) can be adopted in the current modeling framework in a simple manner. However, the discussion of the performance of such alternative decomposition methods are beyond the scope of the present study. In addition to the previous considerations, in the current formulation, we account for the irreversible character of fracture processes via an history dependent variable in line with (156). In order to perform a careful analysis regarding possible effects of the proposed model to ensure such irreversibility, the procedure proposed in (161) is a plausible way to overcome some potential drawbacks preserving the accuracy of the method.

4.2 2D finite element formulation of the phase field model in solids

In this section, the main aspects of the numerical implementation of the PF model for brittle fracture are described within the framework of the finite element method (FEM). First of all, the weak form of the PF model is obtained by the virtual variation of the functional given in Equation

(4.7):

$$\begin{aligned}\delta\Pi(\mathbf{u},\delta\mathbf{u},\mathfrak{d},\delta\mathfrak{d}) = &\int_\Omega \boldsymbol{\sigma} : \delta\boldsymbol{\varepsilon}\,\mathrm{d}\Omega - \int_\Omega 2(1-\mathfrak{d})\delta\mathfrak{d}\psi_+^e(\boldsymbol{\varepsilon})\,\mathrm{d}\Omega + \\ &\int_\Omega \mathcal{G}_c l\left[\frac{1}{l^2}\mathfrak{d}\delta\mathfrak{d} + \nabla_{\mathbf{x}}\mathfrak{d}.\nabla_{\mathbf{x}}(\delta\mathfrak{d})\right]\mathrm{d}\Omega + \delta\Pi_{ext}(\mathbf{u},\delta\mathbf{u}) \\ &\forall\delta\mathbf{u}\in\mathfrak{D}^u, \delta\mathfrak{D}\in\mathfrak{D}^{\mathfrak{d}}\end{aligned} \tag{4.11}$$

where:

$$\begin{aligned}&\mathfrak{D}^u = \delta\mathbf{u} \mid \mathbf{u} = \bar{\mathbf{u}} \text{ on } \delta\Omega_u, \mathbf{u}\in H^1 \\ &\mathfrak{D}^{\mathfrak{d}} = \delta\mathfrak{d} \mid \mathfrak{d} = \bar{\mathfrak{d}} \text{ on } \delta\Gamma_u, \mathfrak{d}\in H^0 \\ &\delta\Pi_{ext}(\mathbf{u},\delta\mathbf{u}) = \textstyle\int_{\delta\Omega}\bar{\boldsymbol{t}}\cdot\delta\mathbf{u}\,\mathrm{d}\delta\Omega + \int_\Omega \boldsymbol{f_v}\cdot\delta\mathbf{u}\,\mathrm{d}\Omega\end{aligned}$$

being $\delta\mathbf{u}$ and $\delta\mathfrak{d}$ the virtual variation of the displacement vector and of the PF variable, respectively.

Secondly, we introduce the finite element (FE) discretization. To mention that, the isoparametric element is the bi-unit square domain centered in the origin of the vector space $\boldsymbol{\xi} = (\xi^1, \xi^2)$. As we can see in Equation (4.12) and (4.13), the position ($\boldsymbol{x}$), the displacement field ($\mathbf{u}$), its variation ($\delta\mathbf{u}$) and its linearization ($\Delta\mathbf{u}$), are interpolated using the Lagrangian shape functions $N^I(\boldsymbol{\xi})$:

$$\boldsymbol{x} \cong \sum_{I=1}^{n} N^I \bar{\boldsymbol{x}}_{\boldsymbol{I}} = \boldsymbol{N}\bar{\boldsymbol{x}}, \quad \mathbf{u} \cong \sum_{I=1}^{n} N^I \mathbf{d}_I = \boldsymbol{N}\boldsymbol{d} \tag{4.12}$$

$$\delta\mathbf{u} \cong \sum_{I=1}^{n} N^I \delta\boldsymbol{d}_{\boldsymbol{I}} = \boldsymbol{N}\delta\boldsymbol{d}, \quad \Delta\mathbf{u} \cong \sum_{I=1}^{n} N^I \Delta\boldsymbol{d}_{\boldsymbol{I}} = \boldsymbol{N}\delta\boldsymbol{d} \tag{4.13}$$

being n the number of nodes per element, $\bar{\boldsymbol{x}}_{\boldsymbol{I}}$ and $\boldsymbol{d}_{\boldsymbol{I}}$ the nodal coordinates and displacement values of the node I, $\bar{\boldsymbol{x}}$ and $\boldsymbol{d}$ the vectors containing the nodal coordinates and nodal displacements of the element and $\boldsymbol{N}$ the operator collecting the interpolation functions at the element level. However, to interpolate the strain field ($\boldsymbol{\varepsilon}$), its variation ($\delta\boldsymbol{\varepsilon}$) and its linearization ($\Delta\boldsymbol{\varepsilon}$), the displacement-strain operator $\boldsymbol{B_d}$ is used as follows:

$$\boldsymbol{\varepsilon} \cong \boldsymbol{B_d}\boldsymbol{d}, \quad \delta\boldsymbol{\varepsilon} \cong \boldsymbol{B_d}\delta\boldsymbol{d}, \quad \Delta\boldsymbol{\varepsilon} \cong \boldsymbol{B_d}\Delta\boldsymbol{d} \tag{4.14}$$

Finally, to interpolate the parameters associated with the damage variable, we need to use two operators $\boldsymbol{B}_{\mathfrak{d}}$ and $\boldsymbol{N}$. In particular, $\boldsymbol{N}$ is used for the interpolation of the PF variable ($\mathfrak{d}$), its variation ($\delta\mathfrak{d}$) and its linearization ($\Delta\mathfrak{d}$):

$$\mathfrak{d} \cong \sum_{I=1}^{n} N^I \bar{\mathfrak{d}_I} = \boldsymbol{N}\bar{\mathfrak{d}}, \quad \delta\mathfrak{d} \cong \sum_{I=1}^{n} N^I \delta\bar{\mathfrak{d}_I} = \boldsymbol{N}\delta\bar{\mathfrak{d}}, \quad \Delta\mathfrak{d} \cong \sum_{I=1}^{n} N^I \Delta\bar{\mathfrak{d}_I} = \boldsymbol{N}\delta\bar{\mathfrak{d}} \tag{4.15}$$

while $\boldsymbol{B}_{\mathfrak{d}}$ is used to interpolate the gradient of the PF variable ($\nabla_{\mathbf{x}}\mathfrak{d}$), its variation ($\nabla_{\mathbf{x}}\delta\mathfrak{d}$) and its linearization ($\nabla_{\mathbf{x}}\Delta\mathfrak{d}$):

$$\nabla_{\mathbf{x}}\mathfrak{d} \cong \boldsymbol{B}_{\mathfrak{d}}\bar{\mathfrak{d}}, \quad \nabla_{\mathbf{x}}(\delta\mathfrak{d}) \cong \boldsymbol{B}_{\mathfrak{d}}\delta\bar{\mathfrak{d}}, \quad \nabla_{\mathbf{x}}(\Delta\mathfrak{d}) \cong \boldsymbol{B}_{\mathfrak{d}}\Delta\bar{\mathfrak{d}} \tag{4.16}$$

Following the same idea as in Equation (4.12), $\bar{\mathfrak{d}_I}$ and $\bar{\mathfrak{d}}$ are, respectively, the values of the PF variable at the node level and the vector containing the nodal PF variable at the element level. After the previous discussion of the interpolation scheme, we can conclude that, the discretized form of Equation (4.11) at the element level is the following:

$$\begin{aligned}
\delta\bar{\Pi}^{el}(\boldsymbol{d}, \delta\boldsymbol{d}, \bar{\mathfrak{d}}, \delta\bar{\mathfrak{d}}) =& \delta\boldsymbol{d}^T \left[\int_{\Omega^{el}} \left[\left((1-\mathfrak{d})^2 + k\right) \boldsymbol{B_d}^T \boldsymbol{\sigma}_+ + \boldsymbol{B_d}^T \boldsymbol{\sigma}_- \right] \mathrm{d}\Omega \right. \\
& \left. - \int_{\partial\Omega^{el}} \boldsymbol{N}^T \bar{\boldsymbol{t}} \, \mathrm{d}\partial\Omega - \int_{\Omega^{el}} \boldsymbol{N}^T \boldsymbol{f}_{\mathrm{v}} \, \mathrm{d}\Omega \right] \\
& + \delta\bar{\mathfrak{d}}^T \left[\int_{\Omega^{el}} -2(1-\mathfrak{d}) \boldsymbol{N}^T \psi_+^e(\boldsymbol{\varepsilon}) \, \mathrm{d}\Omega \right. \\
& \left. + \int_{\Omega^{el}} \mathcal{G}_c l \left(\boldsymbol{B}_{\mathfrak{d}}^T \nabla_{\mathbf{x}}\mathfrak{d} + \frac{1}{l^2} \boldsymbol{N}^T \mathfrak{d} \right) \mathrm{d}\Omega \right] \\
=& \, \delta\boldsymbol{d}^T \boldsymbol{f}_{\mathrm{d}} + \delta\bar{\mathfrak{d}}^T \boldsymbol{f}_{\mathfrak{d}}
\end{aligned} \tag{4.17}$$

where:

$$\begin{aligned}
\boldsymbol{f}_{\mathrm{d}} = \boldsymbol{f}_{\mathrm{d,\,ext}} - \boldsymbol{f}_{\mathrm{d,\,int}} =& \int_{\Omega^{el}} \left[\left((1-\mathfrak{d})^2 + k\right) \boldsymbol{B_d}^T \boldsymbol{\sigma}_+ + \boldsymbol{B_d}^T \boldsymbol{\sigma}_- \right] \mathrm{d}\Omega \\
& - \int_{\partial\Omega^{el}} \boldsymbol{N}^T \bar{\boldsymbol{t}} \, \mathrm{d}\partial\Omega - \int_{\Omega^{el}} \boldsymbol{N}^T \boldsymbol{f}_{\mathrm{v}} \, \mathrm{d}\Omega
\end{aligned} \tag{4.18}$$

$$\boldsymbol{f}_{\mathfrak{d}} = \int_{\Omega^{el}} -2(1-\mathfrak{d}) \boldsymbol{N}^T \psi_+^e(\boldsymbol{\varepsilon}) \, \mathrm{d}\Omega + \int_{\Omega^{el}} \mathcal{G}_c l \left(\boldsymbol{B}_{\mathfrak{d}}^T \nabla_{\mathbf{x}}\mathfrak{d} + \frac{1}{l^2} \boldsymbol{N}^T \mathfrak{d} \right) \mathrm{d}\Omega \tag{4.19}$$

being $\boldsymbol{f}_{\mathrm{d}}$ the residual vector associated to the displacement field and $\boldsymbol{f}_{\mathfrak{d}}$ the residual vector associated to the PF variable.

The linearization of the previous residual vector yields to the following coupled system:

$$\begin{bmatrix} \boldsymbol{K}_{\boldsymbol{dd}} & \boldsymbol{K}_{\boldsymbol{d}\mathfrak{d}} \\ \boldsymbol{K}_{\mathfrak{d}\boldsymbol{d}} & \boldsymbol{K}_{\mathfrak{d}\mathfrak{d}} \end{bmatrix} \begin{bmatrix} \Delta \boldsymbol{d} \\ \Delta \mathfrak{d} \end{bmatrix} = \begin{bmatrix} \boldsymbol{f}_{\boldsymbol{d},\mathrm{ext}} \\ 0 \end{bmatrix} - \begin{bmatrix} \boldsymbol{f}_{\boldsymbol{d},\mathrm{int}} \\ \boldsymbol{f}_{\mathfrak{d}} \end{bmatrix} \tag{4.20}$$

To solve the linearized system, a Jacobi-type solution scheme in line with (156) is used. For further information about the stiffness matrices $\boldsymbol{K}_{\boldsymbol{dd}}$, $\boldsymbol{K}_{\boldsymbol{d}\mathfrak{d}}$, $\boldsymbol{K}_{\mathfrak{d}\boldsymbol{d}}$ and $\boldsymbol{K}_{\mathfrak{d}\mathfrak{d}}$, the reader is referred to (162).

4.3 3D finite element formulation of the phase field model in solid shells

This section summarizes the extension of the PF modeling approach for 3D applications incorporating a nonlinear enhanced assumed solid shell model into the formulation. This shell model is especially suitable for triggering fracture events in thin walled structures, displaying a locking free performance from the numerical standpoint (106; 113).

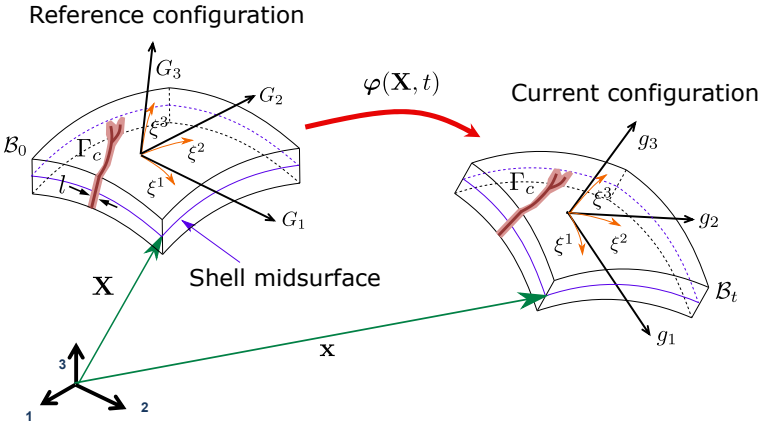

Figure 21: Description of the solid shell element.

For nonlinear shell analysis undergoing large deformations, we denote $\mathcal{B}_0 \subset \mathbb{R}^3$ as the reference placement and $\mathcal{B}_t \subset \mathbb{R}^3$ its correspond-

ing current placement. The position vectors at the reference and current configurations are denoted by $\mathbf{X}$ and $\mathbf{x}$, respectively. The nonlinear deformation mapping is defined as: $\boldsymbol{\varphi}(\mathbf{X}, t) : \mathcal{B}_0 \times [0, t] \rightarrow \mathbb{R}^3$, where $[0, t]$ stands for the time step interval mapping the reference material points ($\mathbf{X} \in \mathcal{B}_0$) onto the current material points ($\mathbf{x} \in \mathcal{B}_t$), such that $\mathbf{x} = \boldsymbol{\varphi}(\mathbf{X}, t)$. The definition of the displacement-derived deformation renders: $\mathbf{F}^u := \partial_{\mathbf{X}} \boldsymbol{\varphi}(\mathbf{X}, t)$, where $J^u = \det[\mathbf{F}^u]$ is the corresponding Jacobian of the transformation and $\partial_{\mathbf{X}}$ is the partial derivative with respect to the reference frame.

The parametric space identified for the current shell model is denoted as: $\mathcal{A} := \{\boldsymbol{\xi} = (\xi^1, \xi^2, \xi^3) \in \mathbb{R}^3 \mid -1 \leq \xi^i \leq +1; i = 1, 2, 3\}$, where (ξ^1, ξ^2) are in-plane directions, ξ^3 stands for the thickness direction and H is the initial shell thickness. The solid shell formulation, also denominated as 6-parameter shell model, envisages the parametrization of an arbitrary material point $\mathbf{X}(\boldsymbol{\xi})$ through the linear interpolation of the position of the top $\mathbf{X}_t(\xi^1, \xi^2)$ and bottom $\mathbf{X}_b(\xi^1, \xi^2)$ vectors:

$$\mathbf{X}(\boldsymbol{\xi}) = \frac{1}{2}\left(1 + \xi^3\right)\mathbf{X}_t(\xi^1, \xi^2) + \frac{1}{2}\left(1 - \xi^3\right)\mathbf{X}_b(\xi^1, \xi^2) \tag{4.21}$$

This interpolation scheme also holds for the current configuration:

$$\mathbf{x}(\boldsymbol{\xi}) = \frac{1}{2}\left(1 + \xi^3\right)\mathbf{x}_t(\xi^1, \xi^2) + \frac{1}{2}\left(1 - \xi^3\right)\mathbf{x}_b(\xi^1, \xi^2) \tag{4.22}$$

The kinematic field, $\mathbf{u}(\boldsymbol{\xi})$ yields:

$$\mathbf{u}(\boldsymbol{\xi}) := \mathbf{x}(\boldsymbol{\xi}) - \mathbf{X}(\boldsymbol{\xi}) = \mathbf{v}(\xi^1, \xi^2) + \xi^3 \mathbf{w}(\xi^1, \xi^2) \tag{4.23}$$

where $\mathbf{v}(\xi^1, \xi^2)$ and $\mathbf{w}(\xi^1, \xi^2)$ stand for the displacement of the shell mid-surface and the displacement vector that accounts for the difference between the shell director vector in the current and in the reference configuration, respectively. The co-variant basis in the reference ($\mathbf{G}_i$) and current ($\mathbf{g}_i$) configurations render:

$$\mathbf{G}_i(\boldsymbol{\xi}) := \frac{\partial \mathbf{X}(\boldsymbol{\xi})}{\partial \xi^i}, \qquad \mathbf{g}_i(\boldsymbol{\xi}) := \frac{\partial \mathbf{x}(\boldsymbol{\xi})}{\partial \xi^i} \tag{4.24}$$

whereas in the curvilinear setting the displacement derived deformation gradient, $\mathbf{F}^u$, takes the form:

$$\mathbf{F}^u := \mathbf{g}_i \otimes \mathbf{G}^i \tag{4.25}$$

The previous parametrization is also assumed for the phase field variable, identifying the phase field variables corresponding to the top and bottom surfaces of the shell, $\mathfrak{d}_t$ and $\mathfrak{d}_b$, respectively (130):

$$\mathfrak{d}(\boldsymbol{\xi}) = \frac{1}{2}\left(1+\xi^3\right)\mathfrak{d}_t(\xi^1,\xi^2) + \frac{1}{2}\left(1-\xi^3\right)\mathfrak{d}_b(\xi^1,\xi^2). \tag{4.26}$$

With regard to the variational formalism, in the current solid shell formulation, the enhanced assumed strain (EAS) technology is advocated to alleviate locking pathologies. In particular, the EAS method is adopted through the additive decomposition of the Green-Lagrange strain tensor $\mathbf{E} = \mathbf{E}^u + \tilde{\mathbf{E}}$, where $\mathbf{E}^u$ and $\tilde{\mathbf{E}}$ denote the compatible and the incompatible counterparts of the strain (109; 163), respectively. In this concern, the formulation is defined through the Hu-Washizu functional, whereby the displacements $\mathbf{u}$, the incompatible strains $\tilde{\mathbf{E}}$, the second Piola-Kirchhoff stress tensor $\mathbf{S}$ and the crack phase field variable $\mathfrak{d}$, constitute the independent fields of the formulation.

Considering a generic shell with cracks as shown in Figure 21, the Hu-Washizu functional takes the following form:

$$\begin{aligned}\Pi(\mathbf{u},\tilde{\mathbf{E}},\mathbf{S},\mathfrak{d}) = &\int_{\mathcal{B}_0\setminus\Gamma} \mathfrak{g}(\mathfrak{d})\Psi(\mathbf{E})\,\mathrm{d}\Omega - \int_{\mathcal{B}_0}\mathbf{S}:\tilde{\mathbf{E}}\,\mathrm{d}\Omega + \underbrace{\int_{\mathcal{B}_0}\mathcal{G}_c^b\gamma(\mathfrak{d},\nabla_{\mathbf{X}}\mathfrak{d})\,\mathrm{d}\Omega}_{\Pi_{\text{fr}}} \\ &+ \Pi_{\text{ext}}\end{aligned} \tag{4.27}$$

where Π_{fr} is the dissipative contribution due to fracture events and Π_{ext} is the external potential.

Taking into account the orthogonality condition for the stress field $\mathbf{S}$ and the enhanced strain field $\tilde{\mathbf{E}}$ (164), the weak form of Equation (4.27) leads to the following residual equations:

$$\begin{aligned}R^u(\mathbf{u},\delta\mathbf{u},\tilde{\mathbf{E}},\mathfrak{d}) = &R^u_{int} - R^u_{ext} = \\ &\int_{\mathcal{B}_0}\mathfrak{g}(\mathfrak{d})\frac{\partial\Psi}{\partial\mathbf{E}}:\delta\mathbf{E}^u\,\mathrm{d}\Omega + \delta\Pi_{\text{ext}} = 0\end{aligned} \tag{4.28}$$

$$R^{\tilde{E}}(\mathbf{u},\tilde{\mathbf{E}},\delta\tilde{\mathbf{E}},\mathfrak{d}) = \int_{\mathcal{B}_0}\mathfrak{g}(\mathfrak{d})\frac{\partial\Psi}{\partial\mathbf{E}}:\delta\tilde{\mathbf{E}}\,\mathrm{d}\Omega = 0 \tag{4.29}$$

$$R^{\mathfrak{d}}(\mathbf{u},\tilde{\mathbf{E}},\mathfrak{d},\delta\mathfrak{d}) = \int_{\mathcal{B}_0} -2(1-\mathfrak{d})\delta\mathfrak{d}\Psi(\mathbf{E})\,\mathrm{d}\Omega + \int_{\mathcal{B}_0} \mathcal{G}_c l\left[\frac{1}{l^2}\mathfrak{d}\delta\mathfrak{d} + \nabla_{\mathbf{x}}\mathfrak{d}\cdot\nabla_{\mathbf{x}}(\delta\mathfrak{d})\right]\mathrm{d}\Omega = 0 \tag{4.30}$$

To solve the previous nonlinear equations, Newton-Raphson method is used. Therefore, it is necessary to linearize the previous equations as follows:

$$\begin{aligned}\tilde{L}[R^u(\mathbf{u},\delta\mathbf{u},\tilde{\mathbf{E}},\mathfrak{d})]\cdot[\Delta\mathbf{u},\Delta\tilde{\mathbf{E}},\Delta\mathfrak{d}] = \\ \int_{\mathcal{B}_0}\mathfrak{g}(\mathfrak{d})\left[\delta\mathbf{E}^{\mathbf{u}}:\frac{\partial^2\Psi}{\partial\mathbf{E}^2}:\Delta\mathbf{E}^{\mathbf{u}} + \frac{\partial\Psi}{\partial\mathbf{E}}:\Delta\delta\mathbf{E}^{u}\right]\mathrm{d}\Omega \\ + \int_{\mathcal{B}_0}\mathfrak{g}(\mathfrak{d})\left[\delta\mathbf{E}^{\mathbf{u}}:\frac{\partial^2\Psi}{\partial\mathbf{E}^2}:\Delta\tilde{\mathbf{E}}\right]\mathrm{d}\Omega \\ + \int_{\mathcal{B}_0}\delta\mathbf{E}^{\mathbf{u}}:\frac{\partial\Psi}{\partial\mathbf{E}}\frac{\partial\mathfrak{g}(\mathfrak{d})}{\partial\mathfrak{d}}\Delta\mathfrak{d}\,\mathrm{d}\Omega\end{aligned} \tag{4.31}$$

$$\begin{aligned}\tilde{L}[R^{\tilde{E}}(\mathbf{u},\tilde{\mathbf{E}},\delta\tilde{\mathbf{E}},\mathfrak{d})]\cdot[\Delta\mathbf{u},\Delta\tilde{\mathbf{E}},\Delta\mathfrak{d}] = \\ \int_{\mathcal{B}_0}\mathfrak{g}(\mathfrak{d})\left[\delta\tilde{\mathbf{E}}:\frac{\partial^2\Psi}{\partial\mathbf{E}^2}:\Delta\mathbf{E}^{u} + \delta\tilde{\mathbf{E}}:\frac{\partial^2\Psi}{\partial\mathbf{E}^2}:\Delta\tilde{\mathbf{E}}\right]\mathrm{d}\Omega + \\ \int_{\mathcal{B}_0}\delta\tilde{\mathbf{E}}:\frac{\partial\Psi}{\partial\mathbf{E}}\frac{\partial\mathfrak{g}(\mathfrak{d})}{\partial\mathfrak{d}}\Delta\mathfrak{d}\,\mathrm{d}\Omega\end{aligned} \tag{4.32}$$

$$\begin{aligned}\tilde{L}[R^{\mathfrak{d}}(\mathbf{u},\tilde{\mathbf{E}},\delta\tilde{\mathbf{E}},\mathfrak{d})]\cdot[\Delta\mathbf{u},\Delta\tilde{\mathbf{E}},\Delta\mathfrak{d}] = \int_{\mathcal{B}_0} -2(1-\mathfrak{d})\delta\mathfrak{d}\frac{\partial\Psi}{\partial\mathbf{E}}:\Delta\mathbf{E}^{u}\,\mathrm{d}\Omega \\ + \int_{\mathcal{B}_0} -2(1-\mathfrak{d})\delta\mathfrak{d}\frac{\partial\Psi}{\partial\mathbf{E}}:\Delta\tilde{\mathbf{E}}\,\mathrm{d}\Omega + \int_{\mathcal{B}_0} 2\delta\mathfrak{d}\Psi(\mathbf{E})\Delta\mathfrak{d}\,\mathrm{d}\Omega \\ + \int_{\mathcal{B}_0}\mathcal{G}_c l\left[\frac{1}{l^2}\delta\mathfrak{d}\Delta\mathfrak{d} + \nabla_{\mathbf{x}}\Delta\mathfrak{d}\cdot\nabla_{\mathbf{x}}(\delta\mathfrak{d})\right]\mathrm{d}\Omega\end{aligned} \tag{4.33}$$

About the FE discretization. To interpolate the position vector in the current and in the reference configuration, standard tri-linear shape func-

tions $\boldsymbol{N}(\boldsymbol{\xi})$ are used:

$$\mathbf{X} \cong \sum_{I=1}^{n} N^I(\xi)\mathbf{X}_I = \boldsymbol{N}(\boldsymbol{\xi})\tilde{\mathbf{X}} \tag{4.34}$$

$$\mathbf{x} \cong \sum_{I=1}^{n} N^I(\xi)\mathbf{x}_I = \boldsymbol{N}(\boldsymbol{\xi})\tilde{\mathbf{x}} \tag{4.35}$$

being $\mathbf{X}_I$ and $\mathbf{x}_I$ the coordinates values of the node I in the reference and current configurations, respectively; $\tilde{\mathbf{X}}$ and $\tilde{\mathbf{x}}$ vectors containing the nodal coordinates of the element in the reference and current configuration and n the number of nodes.

For the interpolation of the displacement field ($\mathbf{u}$) and the phase field variable ($\Delta\mathfrak{d}$), their respective variations ($\delta\mathbf{u}$, $\Delta\mathfrak{d}$) and their increments ($\Delta\mathbf{u}$, $\Delta\mathfrak{d}$), the $\boldsymbol{N}(\boldsymbol{\xi})$ operator is again used:

$$\mathbf{u} \cong \boldsymbol{N}(\boldsymbol{\xi})\mathbf{d}, \quad \delta\mathbf{u} \cong \boldsymbol{N}(\boldsymbol{\xi})\delta\mathbf{d}, \quad \Delta\mathbf{u} \cong \boldsymbol{N}(\boldsymbol{\xi})\Delta\mathbf{d} \tag{4.36}$$

$$\mathfrak{d} \cong \boldsymbol{N}(\boldsymbol{\xi})\tilde{\mathfrak{d}}, \quad \delta\mathfrak{d} \cong \boldsymbol{N}(\boldsymbol{\xi})\delta\tilde{\mathfrak{d}}, \quad \Delta\mathfrak{d} \cong \boldsymbol{N}(\boldsymbol{\xi})\Delta\tilde{\mathfrak{d}} \tag{4.37}$$

where $\mathbf{d}$ is the nodal displacement vector at the element level and $\tilde{\mathfrak{d}}$ is the nodal phase field vector at the element level.

To interpolate the material gradient of the phase field ($\nabla_{\mathbf{x}}(\mathfrak{d})$), its variation ($\nabla_{\mathbf{x}}(\delta\mathfrak{d})$) and its increment ($\nabla_{\mathbf{x}}(\Delta\mathfrak{d})$), a new operator, $\mathbf{B}^{\mathfrak{d}}$, is needed:

$$\nabla_{\mathbf{x}}(\mathfrak{d}) \cong \mathbf{B}^{\mathfrak{d}}(\xi)\tilde{\mathfrak{d}}, \quad \nabla_{\mathbf{x}}(\delta\mathfrak{d}) \cong \mathbf{B}^{\mathfrak{d}}(\xi)\delta\tilde{\mathfrak{d}}, \quad \nabla_{\mathbf{x}}(\Delta\mathfrak{d}) \cong \mathbf{B}^{\mathfrak{d}}(\xi)\Delta\tilde{\mathfrak{d}} \tag{4.38}$$

However, to interpolate the compatible strain field ($\mathbf{E}^u$), its variation ($\delta\mathbf{E}^u$) and its increment ($\Delta\mathbf{E}^u$), the displacement-strain operator **B(d)** is employed:

$$\mathbf{E}^u \cong \mathbf{B(d)}\mathbf{d}, \quad \delta\mathbf{E}^u \cong \mathbf{B(d)}\delta\mathbf{d}, \quad \Delta\mathbf{E}^u \cong \mathbf{B(d)}\Delta\mathbf{d} \tag{4.39}$$

While for the interpolation of the enhanced strain ($\tilde{\mathbf{E}}$), its variation ($\delta\tilde{\mathbf{E}}$) and its increment ($\Delta\tilde{\mathbf{E}}$), the enhancing interpolation matrix $\boldsymbol{M}(\boldsymbol{\xi})$ is used:

$$\tilde{\mathbf{E}} \cong \boldsymbol{M}(\boldsymbol{\xi})\boldsymbol{\zeta}, \quad \delta\tilde{\mathbf{E}} \cong \boldsymbol{M}(\boldsymbol{\xi})\delta\boldsymbol{\zeta}, \quad \Delta\tilde{\mathbf{E}} \cong \boldsymbol{M}(\boldsymbol{\xi})\Delta\boldsymbol{\zeta} \tag{4.40}$$

where $\boldsymbol{\zeta}$ is the vector of the discretized incompatible strains, in other words, it contains the EAS parameters. To say that $\boldsymbol{M}$, is expressed in

the global setting. For that reason, it is necessary a transformation mapping between the parametric ($\tilde{\boldsymbol{M}}$) and the global spaces ($\boldsymbol{M}$), see (106). Finally, the form of the operator $\tilde{\mathbf{M}}(\boldsymbol{\xi})$ used in this work is defined as follows (107; 110):

$$\tilde{\boldsymbol{M}}_{\boldsymbol{\xi}} = \begin{bmatrix} \xi^1 & 0 & 0 & 0 & 0 & 0 & 0 \\ 0 & \xi^2 & 0 & 0 & 0 & 0 & 0 \\ 0 & 0 & \xi^3 & \xi^1\xi^3 & \xi^2\xi^3 & 0 & 0 \\ 0 & 0 & 0 & 0 & 0 & \xi^1 & \xi^2 \\ 0 & 0 & 0 & 0 & 0 & 0 & 0 \\ 0 & 0 & 0 & 0 & 0 & 0 & 0 \end{bmatrix} \tag{4.41}$$

After the insertion of the discretized operators into the corresponding residual forms, the current formulation preserves the computational efficiency of standard shell models, setting the displacement degrees of freedom as the exclusive nodal unknowns via static condensation procedures.

Furthermore, in the current solid shell model, transverse shear and trapezoidal locking are alleviated with the assumed natural strain (ANS) method. To do so, the interpolation of the transverse shear (E_{13}, E_{23}) and normal strain (E_{33}) components are evaluated at some collocation points, which are given in Figure 22.

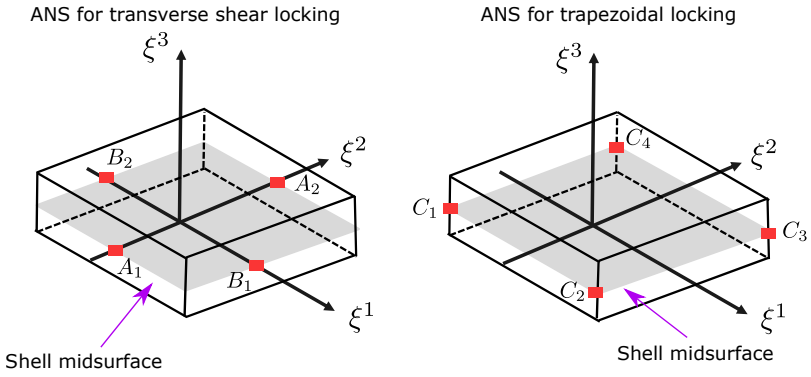

Figure 22: ANS method: definition of the collocation points in the element parametric space.

Therefore, the assumed interpolation of the transverse shear and nor-

mal strain components can be computed as:

$$E_{13}^{ANS} = \sum_{n=1}^{2}(1+\xi_{A_i}^2\xi^2)E_{13}(\xi_A) \tag{4.42a}$$

$$E_{23}^{ANS} = \sum_{n=1}^{2}(1+\xi_{B_i}^1\xi^1)E_{23}(\xi_B) \tag{4.42b}$$

$$E_{33}^{ANS} = \sum_{n=1}^{4}(1+\xi_{C_i}^1\xi^1)(1+\xi_{C_i}^2\xi^2)E_{33}(\xi_C) \tag{4.42c}$$

The insertion of the previous discretization scheme into the residual forms, Equations (4.28)-(4.30), and the linearized systems given in Equations (4.31)-(4.33), leads to the following coupled system:

$$\begin{bmatrix} \boldsymbol{K_{dd}} & \boldsymbol{K_{d\mathfrak{d}}} & \boldsymbol{K_{d\zeta}} \\ \boldsymbol{K_{\mathfrak{d}d}} & \boldsymbol{K_{\mathfrak{d}\mathfrak{d}}} & \boldsymbol{K_{\mathfrak{d}\zeta}} \\ \boldsymbol{K_{\zeta d}} & \boldsymbol{K_{\zeta\mathfrak{d}}} & \boldsymbol{K_{\zeta\zeta}} \end{bmatrix} \begin{bmatrix} \Delta \boldsymbol{d} \\ \Delta\tilde{\mathfrak{d}} \\ \Delta\zeta \end{bmatrix} = \begin{bmatrix} \boldsymbol{R}_{\boldsymbol{d},\text{ext}} \\ 0 \\ 0 \end{bmatrix} - \begin{bmatrix} \boldsymbol{R}_{\boldsymbol{d},\text{int}} \\ \boldsymbol{R}_{\mathfrak{d}} \\ \boldsymbol{R}_{\zeta} \end{bmatrix} \tag{4.43}$$

It is worth mentioning that, this system is reduced due to the static condensation of the incompatible strains at the element level (106). Therefore, the coupled system to solve reads:

$$\begin{bmatrix} \boldsymbol{K}^*_{\boldsymbol{dd}} & \boldsymbol{K}^*_{\boldsymbol{d\mathfrak{d}}} \\ \boldsymbol{K}^*_{\mathfrak{d}\boldsymbol{d}} & \boldsymbol{K}^*_{\mathfrak{d}\mathfrak{d}} \end{bmatrix} \begin{bmatrix} \Delta \boldsymbol{d} \\ \Delta\tilde{\mathfrak{d}} \end{bmatrix} = \begin{bmatrix} \boldsymbol{R}_{\boldsymbol{d},\text{ext}} \\ 0 \end{bmatrix} - \begin{bmatrix} \boldsymbol{R}^*_{\boldsymbol{d},\text{int}} \\ \boldsymbol{R}^*_{\mathfrak{d}} \end{bmatrix} \tag{4.44}$$

being the modified residuals and tangent matrices the following:

$$\boldsymbol{K}^*_{\boldsymbol{dd}} = \boldsymbol{K_{dd}} - \boldsymbol{K_{d\zeta}}\boldsymbol{K}^{-1}_{\zeta\zeta}\boldsymbol{K_{\zeta d}}, \quad \boldsymbol{K}^*_{\boldsymbol{d\mathfrak{d}}} = \boldsymbol{K_{d\mathfrak{d}}} - \boldsymbol{K_{d\zeta}}\boldsymbol{K}^{-1}_{\zeta\zeta}\boldsymbol{K_{\zeta\mathfrak{d}}} \tag{4.45}$$

$$\boldsymbol{K}^*_{\mathfrak{d}\boldsymbol{d}} = \boldsymbol{K_{\mathfrak{d}d}} - \boldsymbol{K_{\mathfrak{d}\zeta}}\boldsymbol{K}^{-1}_{\zeta\zeta}\boldsymbol{K_{\zeta d}}, \quad \boldsymbol{K}^*_{\mathfrak{d}\mathfrak{d}} = \boldsymbol{K_{\mathfrak{d}\mathfrak{d}}} - \boldsymbol{K_{\mathfrak{d}\zeta}}\boldsymbol{K}^{-1}_{\zeta\zeta}\boldsymbol{K_{\zeta\mathfrak{d}}} \tag{4.46}$$

$$\boldsymbol{R}^*_{\boldsymbol{d},\text{int}} = \boldsymbol{R}_{\boldsymbol{d},\text{int}} - \boldsymbol{K_{d\zeta}}\boldsymbol{K}^{-1}_{\zeta\zeta}\boldsymbol{R}_{\zeta}, \quad \boldsymbol{R}^*_{\mathfrak{d}} = \boldsymbol{R}_{\mathfrak{d}} - \boldsymbol{K_{\mathfrak{d}\zeta}}\boldsymbol{K}^{-1}_{\zeta\zeta}\boldsymbol{R}_{\zeta} \tag{4.47}$$

Finally, the solution scheme used is a Jacobi-type (156) as in Section 4.2.

4.4 Extension of the phase field model to functionally graded shells

The functionally graded shells considered in the present dissertation are composed by two phases (metallic and ceramic) whose volume fractions

vary smoothly along the thickness direction. In this section, we want to apply the phase field model to functionally graded (FG) shells. To do so, we only need to define the material properties as functions of the spatial variation as follows (163):

$$p(\xi^3) = p_m * f_m + p_c * f_c \tag{4.48}$$

where the subscripts m and c identify the metallic and ceramic constituents, f is the volume fraction of the corresponding phase and p is a generic material property. The volume fractions are represented by the following equations:

$$f_c = \left[\frac{\xi^3}{H} + \frac{1}{2}\right]^n \tag{4.49}$$

$$f_m = 1 - f_c \tag{4.50}$$

where n is the volume fraction exponent ($n \geq 0$) and H is the initial thickness of the shell. Therefore, when n = 0 a fully ceramic material is represented. However, when n approaches infinity, we are considering a fully metallic structure.

Through the use of the previous expression regarding the spatial variation of the material properties, it is noticing that they are dependent on the volume fraction, i.e. in the present case on the thickness coordinate ξ^3. This rule of mixture affects: Young modulus (E), fracture energy ($\mathcal{G}_c$) and phase field length scale (l). Note that the variation of l with respect to ξ^3 implies a novel aspect with respect to alternative PF formulations for FGMs (132).

Chapter 5

Cohesive zone model

As it is well known, cohesive zone models (CZMs) are widely used to model fracture of interfaces. In the present thesis, two different cohesive models have been used: a new tension cut-off model coupled with phase field (Section 5.1) and a bi-linear traction-separation cohesive model uncoupled with phase field (Section 5.2). Contents of this chapter are partially extracted from (15; 16; 78).

5.1 Cohesive zone model compatible with phase field

In the present section, the new CZM compatible with PF proposed in (14) is exposed. This section includes the basic concepts of this new model and also, its finite element formulation in 2D and 3D interface elements. To make clear that, in the sequel , the combination of the PF model and the new CZM coupled with it is denominated as PF-CZM.

5.1.1 Theoretical concepts

In order to capture complex delamination paths in heterogeneous media, Paggi and Reinoso proposed a numerical technique in (14), which consistently combines the PF approach in the bulk with interface elements complying with the cohesive zone concept. The basic hypothesis of such a technique relies on the consideration of a system which contains a crack Γ_b and a prescribed discontinuity Γ_i (characterizing the presence of an

interface). The material points of the bulk are identified by the position vectors $\mathbf{x}$, whereas a generic point of the interface is denoted by the position vector $\mathbf{x}_c$, see Figure 23.

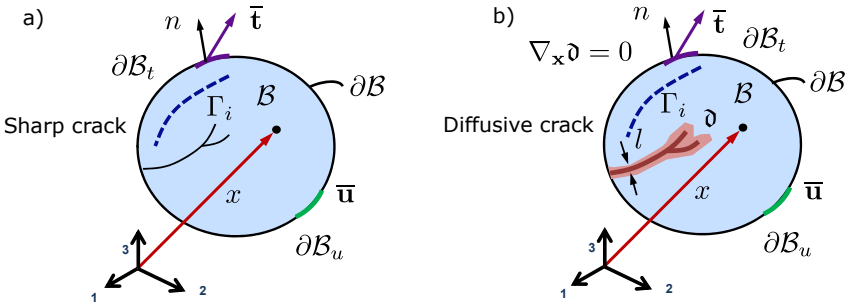

Figure 23: PF-CZ method for diffusive crack modeling for heterogeneous media. The dashed line corresponds to the placement of prescribed interfaces in the system. a) and b) plots identify the sharp and smeared crack representations in the bulk.

Accordingly, the dissipative phenomena in the system can potentially arise from two different sources: (i) the crack propagation within the bulk, and (ii) the delamination events along the existing interfaces.

Assuming this scenario, the total potential energy given in Equation (4.7) is herewith recalled. In particular, the current methodology assumes that the dissipative term in Equation (4.7) can be additively decomposed into: (i) the energy dissipated in the bulk, which is triggered following the standard PF approach and (ii) the energy dissipated via delamination along the existing interfaces, complying with a cohesive-like representation. This split is envisaged via the consideration of the bulk and the interface fracture energies, which are denoted by $\mathcal{G}_c^b$ and $\mathcal{G}^i$, respectively.

In line with this assumption, the internal body functional renders:

$$\Pi_{int}(\mathbf{u}, \Gamma_b, \Gamma_i) = \Pi_{\mathcal{B}} + \Pi_{\Gamma_b} + \Pi_{\Gamma_i} = \int_{\mathcal{B}\setminus\Gamma} \psi^e(\boldsymbol{\varepsilon})\, \mathrm{d}\Omega + \int_{\Gamma_b} \mathcal{G}_c^b(\boldsymbol{u}, \mathfrak{d})\, \mathrm{d}\Gamma + \\ + \int_{\Gamma_i} \mathcal{G}^i\left(\mathbf{g}, \mathfrak{h}, \mathfrak{d}\right)\, \mathrm{d}\Gamma \tag{5.1}$$

being $\mathbf{g}$ the continuous displacement between the two flanks of the interface, whilst $\mathfrak{h}$ and $\mathfrak{d}$ denote an history variable associated with the

interface degradation upon failure (165) and phase field variable in the bulk, respectively.

Without loss of generality, a tension cut-off interface behavior is henceforth adopted. The coupling with the phase field in the bulk is accomplished by modifying the critical displacement gap for each fracture mode through the following relationship (14): $g_c(\mathfrak{d}) = (1-\mathfrak{d})g_{c,0} + \mathfrak{d}g_{c,1}$, where $g_{c,0} = g_c(\mathfrak{d} = 0)$ and $g_{c,1} = g_c(\mathfrak{d} = 1)$. Therefore, as the phase field variable increases, the critical gap also increases. Note however that the current formulation preserves the critical fracture energy, which causes the reduction of the stiffness and the critical stress.

The corresponding traction-displacement gap law for fracture modes I and II are given by (Figure 24):

$$\sigma = \begin{cases} k_n \dfrac{g_n}{g_{nc}}, & \text{if } 0 < \dfrac{g_n}{g_{nc}} < 1; \\ 0, & \text{if } \dfrac{g_n}{g_{nc}} \geq 1, \end{cases} \tag{5.2}$$

$$\tau = \begin{cases} k_t \dfrac{g_t}{g_{tc}}, & \text{if } 0 < \dfrac{g_t}{g_{tc}} < 1; \\ 0, & \text{if } \dfrac{g_t}{g_{tc}} \geq 1. \end{cases} \tag{5.3}$$

where σ and τ identify the interface tractions associated with fracture modes I and II, respectively, whereas g_n and g_t denote the normal and tangential gaps.

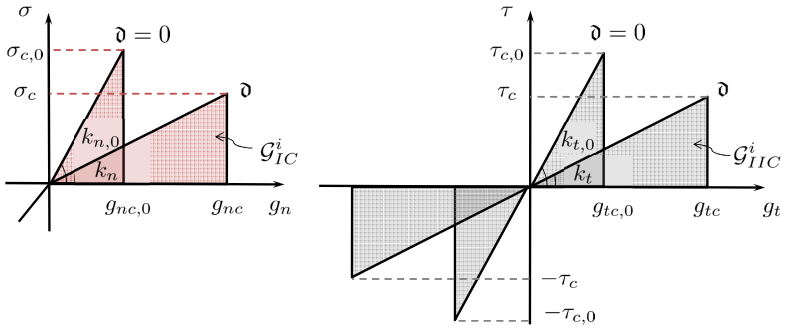

Figure 24: Schematic representation of the traction-separation law of the CZM which accounts for the PF variable. Left: mode I CZM traction σ vs. g_n. Right: mode II CZM traction τ vs. g_t.

Then, recalling the assumption of the critical fracture energy preser-

vation, the apparent interface stiffness in both modes, k_n and k_t, is given by:

$$k_n = k_{n,0}\left(\frac{g_{nc,0}}{g_{nc}}\right)^2; \quad k_t = k_{t,0}\left(\frac{g_{tc,0}}{g_{tc}}\right)^2 \tag{5.4}$$

where $k_{n,0}$ y $k_{t,0}$ indicate the initial normal and tangential stiffness for intact surrounding bulk, respectively, and $g_{nc,0}$ and $g_{tc,0}$ their corresponding critical gaps.

Interface failure is triggered using a standard quadratic fracture criterion:

$$\left(\frac{\mathcal{G}_I^i}{\mathcal{G}_{IC}^i}\right)^2 + \left(\frac{\mathcal{G}_{II}^i}{\mathcal{G}_{IIC}^i}\right)^2 = 1 \tag{5.5}$$

being $\mathcal{G}_I^i$ and $\mathcal{G}_{II}^i$ the energy release rates associated with the fracture modes I and II. If we consider the Equation 5.4 and also the coupling function, the energy release rates are expressed as follows:

$$\begin{aligned} \mathcal{G}_I^i(\mathfrak{d}) &= \frac{1}{2}k_{n,0}g_n^2\frac{g_{nc,0}^2}{\left[(1-\mathfrak{d})g_{nc,0}+\mathfrak{d}g_{nc,1}\right]^2}, \\ \mathcal{G}_{II}^i(\mathfrak{d}) &= \frac{1}{2}k_{t,0}g_t^2\frac{g_{tc,0}^2}{\left[(1-\mathfrak{d})g_{tc,0}+\mathfrak{d}g_{tc,1}\right]^2} \end{aligned} \tag{5.6}$$

As it has been said previously, the critical fracture energies ($\mathcal{G}_{IC}^i$ and $\mathcal{G}_{IIC}^i$) are constant independently of the value of the phase field damage variable. Therefore, they can be computed as follows:

$$\mathcal{G}_{IC}^i = \frac{1}{2}g_{nc,0}^2k_{n,0}; \quad \mathcal{G}_{IIC}^i = \frac{1}{2}g_{tc,0}^2k_{t,0} \tag{5.7}$$

Finally, to mention that this coupling between the phase field and the stiffness of the interface has sense when damage is initiated in the bulk and arrives to an interface (131). For other cases, a classical tension cut-off law is considered by assuming a coupling factor ($g_{c,1}/g_{c,0}$) equal to 1.

5.1.2 2D finite element formulation of the new cohesive zone model compatible with the phase field approach of brittle fracture

This subsection presents the formulation and implementation of the CZM compatible with PF in a 4 node isoparametric interface finite element

(Figure 25). Therefore, the variational formulation regarding the interface contribution to the total functional of the system given in Equation (5.1), is presented. Complying with a standard Galerkin procedure, the weak form of the interface contribution reads:

$$\delta\Pi_{\Gamma_i}(\mathbf{u},\delta\mathbf{u},\mathfrak{d},\delta\mathfrak{d}) = \int_{\Gamma_i}\left(\frac{\partial\mathcal{G}^i(\boldsymbol{u},\mathfrak{d})}{\partial\boldsymbol{u}}\delta\boldsymbol{u} + + \frac{\partial\mathcal{G}^i(\boldsymbol{u},\mathfrak{d})}{\partial\mathfrak{d}}\delta\mathfrak{d}\right)\,\mathrm{d}\Gamma \qquad (5.8)$$

In Equation (5.8), $\delta\mathbf{u}$ denotes the admissible kinematic field vector function ($\mathfrak{V}^u = \left\{\delta\mathbf{u}\,|\,\mathbf{u}=\overline{\mathbf{u}}\text{ on }\partial\mathcal{B}_u,\mathbf{u}\in\mathcal{H}^1\right\}$), whereas $\delta\mathfrak{d}$ identifies the approximation functions of the phase field variable ($\mathfrak{V}^\mathfrak{d} = \{\delta\mathfrak{d}\,|\,\delta\mathfrak{d}=0\text{ on }\Gamma_b\,,\mathfrak{d}\in\mathcal{H}^0\}$).

The discretization of the previous variational form can be carried out within the context of the FEM through the use of standard isoparametric elements. Without loss of generality, we adopt a first-order interpolation scheme for the kinematic and the phase field variables. Thus, $\boldsymbol{d}$ represents the nodal-based displacement field and $\bar{\mathfrak{d}}$ denotes the nodal-based phase field, both vectors being defined at the element level for the corresponding numerical implementation.

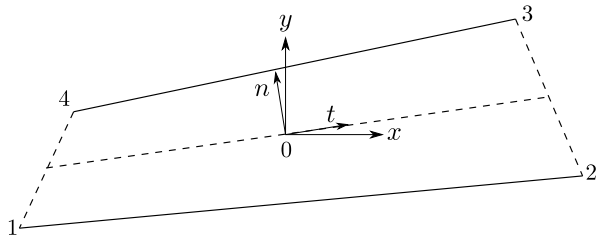

Figure 25: 2D interface element: local setting.

Accordingly, the discrete form of Equation (5.8) at the element level Γ_i^{el} ($\Gamma_i \sim \bigcup\Gamma_i^{el}$) adopts the form:

$$\delta\tilde{\Pi}^{el}_{\Gamma_i}(\mathbf{d},\delta\mathbf{d},\bar{\mathfrak{d}},\delta\bar{\mathfrak{d}}) = \int_{\Gamma_i^{el}}\left(\frac{\partial\mathcal{G}^i(\boldsymbol{d},\bar{\mathfrak{d}})}{\partial\boldsymbol{d}}\delta\boldsymbol{d} + \frac{\partial\mathcal{G}^i(\boldsymbol{d},\bar{\mathfrak{d}})}{\partial\bar{\mathfrak{d}}}\delta\bar{\mathfrak{d}}\right)\,\mathrm{d}\Gamma \qquad (5.9)$$

where $\mathcal{G}^i = \mathcal{G}^i_I + \mathcal{G}^i_{II}$:

The displacement vector between the crack flanks along the interface is characterized by the gap vector, $\boldsymbol{g}$. The discrete form of the gap vector for each point of Γ_i^{el} can be computed as the difference between the displacements of opposite points along the interface, which can be obtained

from the nodal displacements $\mathbf{d}$ multiplied by the average matrix $\mathbf{L}$ and the interpolation matrix $\mathbf{N}$:

$$\boldsymbol{g} = \boldsymbol{N}\boldsymbol{L}\boldsymbol{d} = \hat{\mathbf{B}}_{\mathbf{d}}\boldsymbol{d} \tag{5.10}$$

identifying $\hat{\mathbf{B}}_{\mathbf{d}} = \boldsymbol{N}\boldsymbol{L}$ as the interface compatibility operator. The constitutive law at the interface requires the consideration of a local setting, which is defined by the normal and tangential unit vectors (124). Correspondingly, the gap vector in the global setting (Equation (5.10)) is multiplied by the rotation matrix $\boldsymbol{R}$ in order to obtain the gap vector in the local setting $\boldsymbol{g}_{\text{loc}}$:

$$\boldsymbol{g}_{\text{loc}} \cong \boldsymbol{R}\boldsymbol{g} = \boldsymbol{R}\hat{\mathbf{B}}_{\mathfrak{b}}\boldsymbol{d} \tag{5.11}$$

In a similar manner, the discrete average phase field variable $\mathfrak{d}$ at the interface (Γ_i^{el}) can be computed at the element level as follows:

$$\mathfrak{d} \cong \boldsymbol{N}_{\mathfrak{d}}\boldsymbol{M}_{\mathfrak{d}}\bar{\mathfrak{d}} = \hat{\boldsymbol{B}}_{\mathfrak{d}}\bar{\mathfrak{d}} \tag{5.12}$$

where $\boldsymbol{M}_{\mathfrak{d}}$ is a matrix for determining the average value of the phase field variable between the interface flanks, and $\hat{\boldsymbol{B}}_{\mathfrak{d}} = \boldsymbol{N}_{\mathfrak{d}}\boldsymbol{M}_{\mathfrak{d}}$ identifies the compatibility operator for the phase field. The particular form of such matrices are derived in (14; 88), being omitted here for the sake of brevity. Then, the discrete variational form renders:

$$\begin{aligned}
\delta\tilde{\Pi}_{\Gamma_i}^{el}(\mathbf{d}, \delta\mathbf{d}, \bar{\mathfrak{d}}, \delta\bar{\mathfrak{d}}) &= \delta\boldsymbol{d}^{\mathrm{T}} \int_{\Gamma_i^{el}} \left(\frac{\partial \mathcal{G}^i(\boldsymbol{d}, \bar{\mathfrak{d}})}{\partial \boldsymbol{d}}\right)^{\mathrm{T}} \mathrm{d}\Gamma \\
&+ \delta\bar{\mathfrak{d}}^{\mathrm{T}} \int_{\Gamma_i^{el}} \left(\frac{\partial \mathcal{G}^i(\boldsymbol{d}, \bar{\mathfrak{d}})}{\partial \bar{\mathfrak{d}}}\right)^{\mathrm{T}} \mathrm{d}\Gamma \\
&= \delta\boldsymbol{d}^{\mathrm{T}} \int_{\Gamma_i^{el}} \hat{\mathbf{B}}_{\mathbf{d}}^{\mathrm{T}} \boldsymbol{R}^{\mathrm{T}} \left(\frac{\partial \mathcal{G}^i(\boldsymbol{d}, \bar{\mathfrak{d}})}{\partial \boldsymbol{g}_{\text{loc}}}\right)^{\mathrm{T}} \mathrm{d}\Gamma \\
&+ \delta\bar{\mathfrak{d}}^{\mathrm{T}} \int_{\Gamma_i^{el}} \hat{\boldsymbol{B}}_{\mathfrak{d}}^{\mathrm{T}} \left(\frac{\partial \mathcal{G}^i(\boldsymbol{d}, \bar{\mathfrak{d}})}{\partial \bar{\mathfrak{d}}}\right)^{\mathrm{T}} \mathrm{d}\Gamma
\end{aligned} \tag{5.13}$$

leading to the residual vectors:

$$\boldsymbol{f}_{\mathbf{d}}^{\boldsymbol{i}} = \int_{\Gamma_i^{el}} \hat{\mathbf{B}}_{\mathbf{d}}^{\mathrm{T}} \boldsymbol{R}^{\mathrm{T}} \left(\frac{\partial \mathcal{G}^i(\boldsymbol{d}, \bar{\mathfrak{d}})}{\partial \boldsymbol{g}_{\text{loc}}}\right)^{\mathrm{T}} \mathrm{d}\Gamma \tag{5.14a}$$

$$\boldsymbol{f}_{\mathfrak{d}}^{\boldsymbol{i}} = \int_{\Gamma_i^{el}} \hat{\boldsymbol{B}}_{\mathfrak{d}}^{\mathrm{T}} \left(\frac{\partial \mathcal{G}^i(\boldsymbol{d}, \bar{\mathfrak{d}})}{\partial \mathfrak{d}}\right)^{\mathrm{T}} \mathrm{d}\Gamma \tag{5.14b}$$

Finally, the consistent linearization of the previous residual vectors allows the computation of the element tangents of the proposed interface formulation:

$$\boldsymbol{K}^i_{\mathbf{dd}} = \frac{\partial \boldsymbol{f}_{\mathbf{d}}}{\partial \boldsymbol{d}} = \int_{\Gamma^{el}_i} \hat{\mathbf{B}}^{\mathrm{T}}_{\mathbf{d}} \boldsymbol{R}^{\mathrm{T}} \mathbb{C}^i_{\mathbf{dd}} \boldsymbol{R} \hat{\mathbf{B}}_{\mathbf{d}} \mathrm{d}\Gamma \tag{5.15a}$$

$$\boldsymbol{K}^i_{\mathbf{d}\mathfrak{d}} = \frac{\partial \boldsymbol{f}_{\mathbf{d}}}{\partial \mathfrak{d}} = \int_{\Gamma^{el}_i} \hat{\mathbf{B}}^{\mathrm{T}}_{\mathbf{d}} \boldsymbol{R}^{\mathrm{T}} \mathbb{C}^i_{\mathbf{d}\mathfrak{d}} \hat{\boldsymbol{B}}_{\mathfrak{d}} \mathrm{d}\Gamma \tag{5.15b}$$

$$\boldsymbol{K}^i_{\mathfrak{d}\mathbf{d}} = \frac{\partial \boldsymbol{f}_{\mathfrak{d}}}{\partial \boldsymbol{d}} = \int_{\Gamma^{el}_i} \hat{\boldsymbol{B}}^{\mathrm{T}}_{\mathfrak{d}} \mathbb{C}^i_{\mathfrak{d}d} \boldsymbol{R} \hat{\mathbf{B}}_{\mathbf{d}} \mathrm{d}\Gamma \tag{5.15c}$$

$$\boldsymbol{K}^i_{\mathfrak{d}\mathfrak{d}} = \frac{\partial \boldsymbol{f}_{\mathfrak{d}}}{\partial \mathfrak{d}} = \int_{\Gamma^{el}_i} \hat{\boldsymbol{B}}^{\mathrm{T}}_{\mathfrak{d}} \mathbb{C}^i_{\mathfrak{d}\mathfrak{d}} \hat{\boldsymbol{B}}_{\mathfrak{d}} \mathrm{d}\Gamma \tag{5.15d}$$

where the interface operators are given by:

$$\mathbb{C}^i_{dd} = \begin{bmatrix} \hat{\alpha} k_n & 0 \\ 0 & \hat{\beta} k_t \end{bmatrix} \tag{5.16a}$$

$$\mathbb{C}^i_{\mathbf{d}\mathfrak{d}} = \left[g_n k_n \frac{\partial \hat{\alpha}}{\partial \mathfrak{d}}, g_t k_t \frac{\partial \hat{\beta}}{\partial \mathfrak{d}} \right] \tag{5.16b}$$

$$\mathbb{C}^i_{\mathfrak{d}\mathbf{d}} = \begin{bmatrix} g_n k_n \dfrac{\partial \hat{\alpha}}{\partial \mathfrak{d}} \\ g_t k_t \dfrac{\partial \hat{\beta}}{\partial \mathfrak{d}} \end{bmatrix} \tag{5.16c}$$

$$\mathbb{C}^i_{\mathfrak{d}\mathfrak{d}} = \frac{1}{2} g_n^2 k_n \frac{\partial^2 \hat{\alpha}}{\partial \mathfrak{d}^2} + \frac{1}{2} g_t^2 k_t \frac{\partial^2 \hat{\beta}}{\partial \mathfrak{d}^2} \tag{5.16d}$$

In the previous expressions $\hat{\alpha}$ y $\hat{\beta}$ are particularized as follows:

$$\hat{\alpha} = \frac{g^2_{nc,0}}{\left[(1-\mathfrak{d}) g_{nc,0} + \mathfrak{d} g_{nc,1}\right]^2} \tag{5.17a}$$

$$\hat{\beta} = \frac{g^2_{tc,0}}{\left[(1-\mathfrak{d}) g_{tc,0} + \mathfrak{d} g_{tc,1}\right]^2} \tag{5.17b}$$

In line with Equation 4.20 and 4.43, the final derivation endows a coupled system of equations which is solved in a monolithic manner via a Newton-Raphson scheme.

5.1.3 3D finite element formulation of the new cohesive zone model compatible with the phase field approach of brittle fracture

Differing from the previous 2D small strain formulation, it is notable to remark that the extension to 3D cases requires the introduction of the fracture mode III within the proposed framework and the computation of the linearization of the rotation operator with respect to the displacement field as was detailed in (88). Then, the constitutive response for a generic fracture mode reads:

$$S_m = \begin{cases} k_m \dfrac{g_m}{g_{m,c}}, & \text{if } 0 < \dfrac{g_m}{g_{m,c}} < 1; \\ 0, & \text{if } \dfrac{g_m}{g_{m,c}} \geq 1. \end{cases} \qquad \text{with} \quad m = n, t1, t2 \tag{5.18}$$

where S_m identifies the Piola stress of the interface, $S_{m,c}$ its corresponding critical value, g_m and $g_{m,c}$ the displacement gap and its critical value in the local reference system of the interface (Figure 26) and k_m the interface stiffness. To highlight that n identifies the fracture mode I, $t1$ the mode II and $t2$ the mode III. Finally, to say that the previous cohesive law is further equipped by a penalty formulation in compression with the aim of precluding the material interpenetration at the interface.

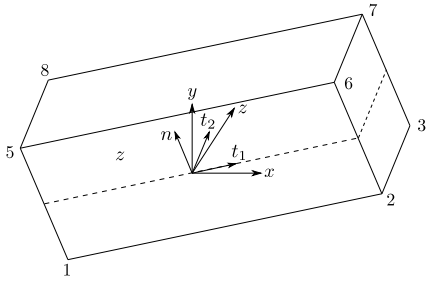

Figure 26: 3D interface element: local setting.

Relying on the previous considerations, the fracture energies for a generic fracture mode are:

$$\mathcal{G}^i_{m,c} = \frac{1}{2} S_m g_{m,c} = \frac{1}{2} k_m g^2_{m,c} \qquad \text{with} \quad m = n, t1, t2 \tag{5.19}$$

Similarly to the 2D case, the critical relative displacements triggering interface failure have a linear dependence on $\mathfrak{d}$. On the contrary, the critical energy release rate for each fracture mode is always constant. Then, imposing the independence of the fracture energies for each mode and the crack phase field value, the following expressions for the energy release rates are derived:

$$\mathcal{G}_m^i(\mathfrak{d}) = \frac{1}{2} k_{m,0} g_m^2 \frac{g_{m,c,0}^2}{\left[(1-\mathfrak{d}) g_{m,c,0} + \mathfrak{d} g_{m,c,1}\right]^2} \qquad \text{with} \quad m = n, t1, t2 \tag{5.20}$$

Without loss of generality, a standard quadratic criterion to trigger the interface failure under mixed mode fracture conditions is again adopted as in 2D and it reads:

$$\left(\frac{\mathcal{G}_n^i}{\mathcal{G}_{n,C}^i}\right)^2 + \left(\frac{\mathcal{G}_{t1}^i}{\mathcal{G}_{t1,C}^i}\right)^2 + \left(\frac{\mathcal{G}_{t2}^i}{\mathcal{G}_{t2,C}^i}\right)^2 = 1 \tag{5.21}$$

Finally, the following tangent constitutive operators at the interface are derived for the subsequent numerical treatment via nonlinear FEM:

$$\frac{\partial^2 \mathcal{G}_c^i}{\partial \mathbf{g}_{\text{loc}}^2} = \begin{bmatrix} \hat{\alpha} k_n & 0 & 0 \\ 0 & \hat{\beta} k_{t1} & 0 \\ 0 & 0 & \hat{\gamma} k_{t2} \end{bmatrix} \tag{5.22a}$$

$$\frac{\partial^2 \mathcal{G}_c^i}{\partial \mathbf{g}_{\text{loc}} \partial \hat{\mathfrak{d}}} = \begin{bmatrix} g_n k_n \dfrac{\partial \hat{\alpha}}{\partial \hat{\mathfrak{d}}} & g_{t1} k_{t1} \dfrac{\partial \hat{\beta}}{\partial \hat{\mathfrak{d}}} & g_{t2} k_{t2} \dfrac{\partial \hat{\gamma}}{\partial \hat{\mathfrak{d}}} \end{bmatrix} \tag{5.22b}$$

$$\frac{\partial^2 \mathcal{G}_c^i}{\partial \hat{\mathfrak{d}} \partial \mathbf{g}_{\text{loc}}} = \begin{bmatrix} g_n k_n \dfrac{\partial \hat{\alpha}}{\partial \hat{\mathfrak{d}}} \\ g_{t1} k_{t1} \dfrac{\partial \hat{\beta}}{\partial \hat{\mathfrak{d}}} \\ g_{t2} k_{t2} \dfrac{\partial \hat{\gamma}}{\partial \hat{\mathfrak{d}}} \end{bmatrix} \tag{5.22c}$$

$$\frac{\partial^2 \mathcal{G}_c^i}{\partial \delta \hat{\mathfrak{d}}^2} = \frac{1}{2} g_n^2 k_n \frac{\partial^2 \hat{\alpha}}{\partial \hat{\mathfrak{d}}^2} + \frac{1}{2} g_{t1}^2 k_{t1} \frac{\partial^2 \hat{\beta}}{\partial \hat{\mathfrak{d}}^2} + \frac{1}{2} g_{t2}^2 k_{t2} \frac{\partial^2 \hat{\gamma}}{\partial \hat{\mathfrak{d}}^2} \tag{5.22d}$$

where the terms $\hat{\alpha}$, $\hat{\beta}$ and $\hat{\gamma}$ are given by:

$$\hat{\alpha} = \frac{g_{nc,0}^2}{\left[(1-\mathfrak{d})g_{nc,0} + \mathfrak{d}g_{nc,1}\right]^2} \tag{5.23a}$$

$$\hat{\beta} = \frac{g_{t1c,0}^2}{\left[(1-\mathfrak{d})g_{t1c,0} + \mathfrak{d}g_{t1c,1}\right]^2} \tag{5.23b}$$

$$\hat{\gamma} = \frac{g_{t2c,0}^2}{\left[(1-\mathfrak{d})g_{t2c,0} + \mathfrak{d}g_{t2c,1}\right]^2} \tag{5.23c}$$

5.2 Cohesive zone model uncoupled with phase field

In this section, a cohesive zone model uncoupled with phase field is exposed. This cohesive model obeys a bi-linear traction-separation law (TSL) which relates the displacement jump across the interface (identified by the normal g_n and shear g_t components) with the corresponding components of the traction vector acting on it, i.e σ and τ, respectively, see Figure 27 for fracture modes I and II. This particular decohesion law follows two different phases:

- An initial linear elastic stage (from point 0 to point 1) prior damage occurrence at the interface. It is characterized by a high initial stiffness k.
- Once the combination of interfacial tractions fulfills the damage initiation criterion, point 1, the interface stiffness is gradually degraded up to via points 2 and 3.

As was comprehensively derived in (166), this is equipped with an internal damage variable $d \in [0,1]$ ($d = 0$ intact interface, $d = 1$ fully debonded interface), which ensures the irreversible character of the decohesion process and tracks the progressive stiffness degradation.

Accordingly, the corresponding TSL in 2D is given by:

$$\sigma = (1-d)kg_n \;\text{ if }\; g_n \geq 0; \qquad \tau = (1-d)kg_t \;\text{ if }\; g_t \geq 0. \tag{5.24}$$

To predict the damage propagation under mixed-mode the classical quadratic criterion is used:

$$\left(\frac{\mathcal{G}_I}{\mathcal{G}_{IC}}\right)^2 + \left(\frac{\mathcal{G}_{II}}{\mathcal{G}_{IIC}}\right)^2 = 1. \tag{5.25}$$

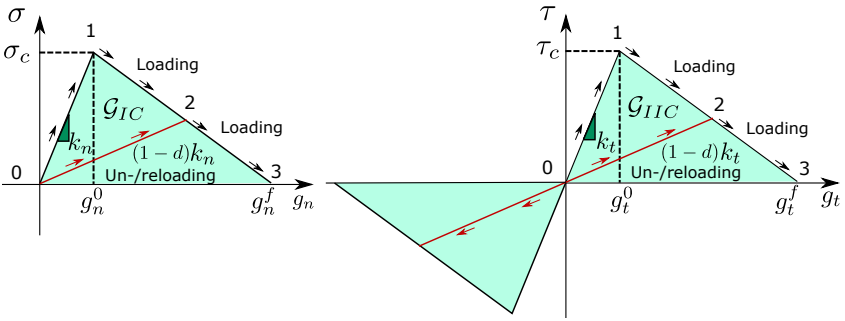

Figure 27: Bi-linear traction-separation law (TSL). Left: mode I. Right: mode II.

Finally, it is worth noting that this model is implemented in the finite element program ABAQUS (built-in implementation).

Chapter 6

Fracture simulation in long-fiber reinforced composites

In this chapter, the combination of the phase field approach for fracture and the cohesive zone model is exploited to demonstrate its capability and accuracy for the study of failure initiation at the micro-scale in long-fiber reinforced composites and the subsequent propagation of damage into the meso-scale. The onset of failure at the micro-scale is studied by means of the mono-fiber problem. However, the transition to meso-scale crack events is analysed through cross ply composites simulations. This chapter is organized as follows. In Section 6.1, there are some experimental results of CFRP composites under uni-axial transverse tension. After that, in Section 6.2, the single fiber-matrix decohesion problem have been simulated. In particular, this problem is simulated under transverse tension, under transverse bi-axial tension and finally, the influence of a neighbouring fiber on the system response is analyzed. In Section 6.3 the simulation of the fracture phenomena in cross ply laminates is addressed. Finally, to say that the present chapter is based on (15; 16) and to highlight the introduction of two length scales into the model: l (associated with the PF model) and l_{CZM} (related to the CZM). After the computation of both length parameters (124; 126) through the material properties under consideration, it has been noticed that they are of similar order of magnitude (see Equations 6.1 and 6.2). Therefore, once the

interface failure arises, a competition between both damage mechanisms might take place.

$$l = \frac{27E'\mathcal{G}_C}{256\sigma_c^2} = 9{\times}10^{-4} \text{ and } 1{\times}10^{-3} \text{ mm (Section 6.2 and 6.3, respectively).} \tag{6.1}$$

$$l_{CZM} = \frac{\pi E \mathcal{G}_{CI}}{2(1-\nu^2)\sigma_{CI}^2} = 1.7 \times 10^{-3} \text{ mm (both Sections).} \tag{6.2}$$

6.1 Preliminary in-situ experimental results

To illustrate the problem of inter-fiber (matrix) failure at the micro-scopic scale, several preliminary experimental tests have been conducted to analyze the response of CFRP composites subjected to uni-axial tensile loading transverse to the fiber direction. Figure 28 shows a schematic representation of the experiments, which were carried out using a tensile stage (DEBEN 5000S) inside a scanning electron microscope (Zeiss EVO MA-15). This experimental setup allows the in-situ characterization of the specimen response and fracture.

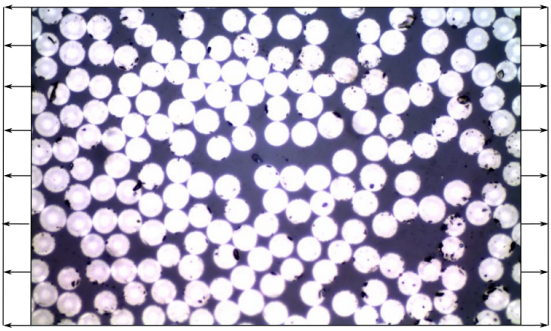

Figure 28: Schematic of the experiments carried out.

As a result of the applied loading, in line with previous investigations (23; 32; 167), inter-fiber failure is characterized by two main different stages at the micro-scale. In Stage 1, the specimen response features a linear elastic evolution load-displacement curve up to the appearance of small debonds at fiber-matrix interfaces (usually aligned with the pre-

scribed loading) which grow unstably under mixed mode fracture conditions till reaching a critical debonding angle. Subsequently, in Stage 2, some of such interface cracks kink out into the matrix promoting their coalescence and leading to transverse macro-cracks in the ply which eventually can lead to catastrophic failure. This description is coincident with the experimental evidences obtained in our preliminary tests, as can be observed in Figure 29 (a) (a careful description of those tests is beyond the scope of the present work). Moreover, performing a postmortem inspection using SEM imaging, it is even possible to observe some fibers totally separated from the main specimen, see Figure 29 (b). These observations remark the need for a consistent approach to model the progression of cracks between the fiber-matrix interface and the matrix.

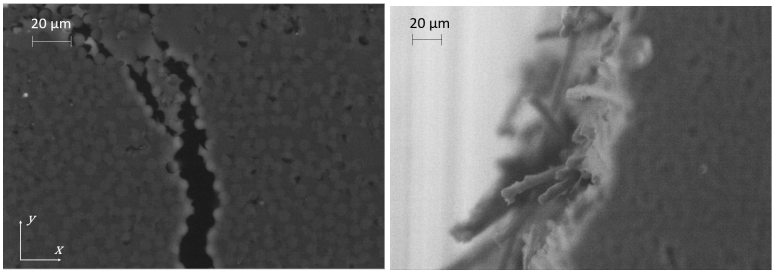

(a) Mag=1000×, WD=5.0mm, Chamber pressure =69Pa.

(b) Mag=747×, WD=6mm, Chamber pressure=70Pa.

Figure 29: SEM images of fracture of a unidirectional laminate of carbon-epoxy subjected to transverse loading. EHT=28.00kV, Signal=NTS BSD.

This preliminary study clearly shows the high complexity of the micro-scopic failure modes in long-fiber reinforced composites. Consequently, with the aim of exploiting their load bearing capacities, it is important to provide a deeper insight into the failure characteristics of such materials. This target can be achieved through the use of high fidelity micro-mechanical numerical models (mostly based on FE methods), which robustly capture the interface failure-matrix debonding and the subsequent kinking into the matrix and coalescence. The importance of capturing such inelastic effects at the micro-scale stems from the fact that macro-scopic fracture in fiber reinforced materials is generally the result of the evolution of localized micro-scopic cracks.

6.2 Fracture in single-fiber problems

The starting point for the prediction of the sequence of stages of failure initiation in the micro-scale (observed in the previous experiments) is the simulation of the mono-fiber problem. In this section, the single fiber problem is simulated under transverse tension (6.2.1) and under transverse bi-axial tension (6.2.2). After that, the effect of a secondary fiber is analysed (6.2.3). It is worth mentioning that, all the simulations are performed with the finite element program `FEAP` (168) and under displacement control.

6.2.1 Numerical simulations of the single fiber-matrix decohesion problem under transverse tension

The system under analysis, given in Figure 30, is defined by: (i) a single fiber with circular transverse section with radius R = 0.0125 mm, (ii) a surrounding squared-matrix domain with side length equal to $L = 0.2$ mm, and (iii) an interface that is located between the previous entities. In line with (31), both matrix and fiber are taken as linear elastic materials, and initially the fiber-matrix interface is assumed as perfectly bonded. Note that L is large enough relatively to R in order to neglect the edge effects.

The fracture properties of the interface and the material properties corresponding to the fiber and matrix are collected in Table 1, see (12; 23). According to the tension cut-off interface behavior previously detailed in Chapter 5, the apparent stiffness properties of the interface, i.e. k_{n0} and k_{t0} prior damage initiation, can be computed in a straightforward manner. Through the exploitation of the symmetry of the system, only one quarter of the domain is initially considered.

Material	E [GPa]	ν	$\mathcal{G}_C$ [N/mm]	l [mm]
Fiber	201	0.22	16	0.39
Matrix	2.8	0.33	0.016	0.0009

Interface Property	σ_C [MPa]	$\mathcal{G}_C$ [N/mm]
Fracture Mode I	75	0.002
Fracture Mode II	90	0.008

Table 1: Mechanical properties of fiber, matrix and interface.

For the application of the PF-CZM approach, the domain is discretized using first-order isoparametric elements. The mesh characteristics are:

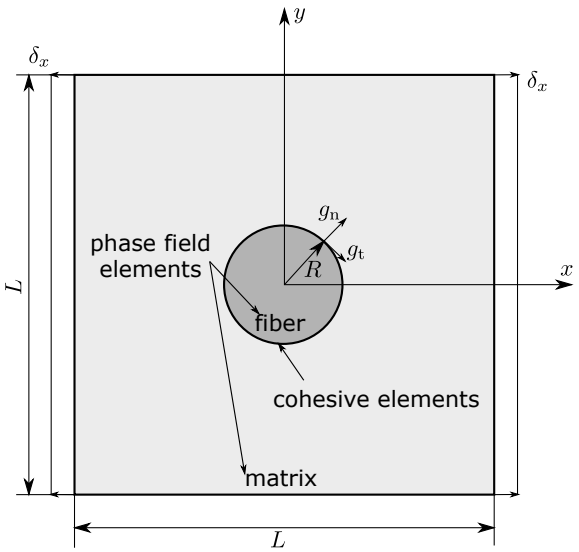

Figure 30: Micro-mechanics of fiber reinforced composite materials under transverse tensile loading conditions: geometry and boundary conditions.

30274 elements for the matrix, 1200 elements for the interface and 19095 for the fiber.

The simulations are conducted under displacement control at the lateral edges of the system (Figure 30), δ_x denoting the external displacement from which the imposed apparent strain can be computed as $\tilde{\varepsilon}_x = \delta_x/(L/2)$. The average stress is computed by adding all the nodal reaction forces on the right edge and dividing by the edge length. At upper and lower edges free-stress boundary conditions are prescribed.

Figure 31 depicts the load-displacement evolution curve of the current analysis. The response of the system is characterized by four different stages:

- The first stage of the response shows a linear elastic evolution. In this stage the non-linearities introduced by (i) the initiation of the cohesive separation between fiber and matrix along the interface and (ii) the phase field at fiber and matrix do not play any role in the global mechanical behavior of the system. This stage concludes

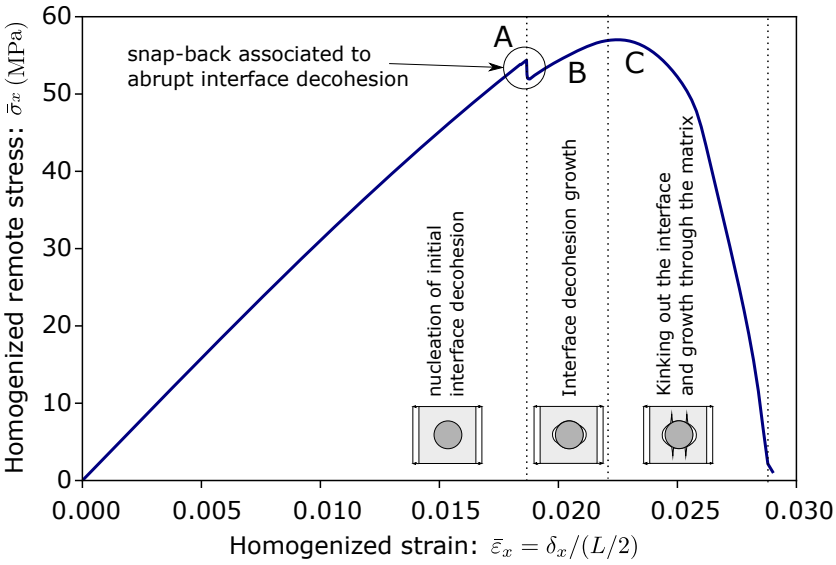

(a)

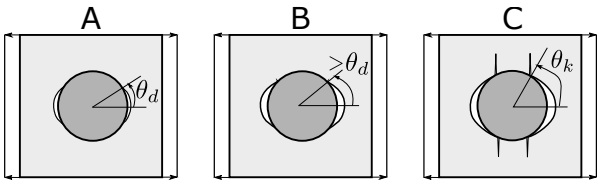

(b)

Figure 31: Micro-mechanics of fiber reinforced composite materials under transverse tensile loading conditions: (a) stress-strain evolution curve and damage pattern at different stages of the simulation. (b) Debonding and kinking angles.

with the sudden decohesion of a finite part of the fiber-matrix interface. This sudden decohesion is reflected in a drop of the stress-strain curve, see Figure 31. This failure is abrupt due to the fact that the interface crack is initiated at a non-singular point, generating a snap-back instability. Actually, to follow the unstable branch of the equilibrium path caused by snap-back, a different solution scheme should be used, as the arc-length control. However, the behavior observed here is what typically is obtained using a Newton-Raphson scheme if a snap-back instability occurs in the system. The influence of the element size and time step on the observed instability was studied and the equilibrium path tends to be fully reproducible and confirmed for element size and time size small enough.

- The second stage is characterized by the onset of damage being in agreement with (13; 30; 31). This failure is an abrupt decohesion of the fiber-matrix interface with a debonding angle approximately equal to 56°. As was mentioned above, this stage is unstable so that the interface crack onset is triggered between two consecutive pseudo-time steps in the simulations. The current predictions contrast with those given in (40), whereby the lack of the interface consideration leads to the prediction of matrix failure very close to the interface.

- A further increase in the applied displacement leads to the third stage of the system evolution, which features further interface decohesion followed by kinking of the crack into the matrix. This is a typical response in the fracture between dissimilar materials, when an existing interface crack tends to kink out into (preferentially) the compliant material (in this case the matrix) due to the higher crack growth resistance along the interface. In this particular case this tendency is promoted by the fact that the fracture mixity of the interface crack grows with the decohesion angle. These results generate an increase of the fracture toughness at the crack tip for decohesion, making energetically more favourable crack growth into the matrix. In the present simulations, interface progression failure is estimated to progress from 56° to 60°. After this, the crack kinks out and penetrates into the matrix. These predictions are in excellent agreement with the observations in (23). From a qualitative point of view, this stage exhibits a continuous increasing stress-strain evolution along the loading path upon complete failure.

(a) Damage variable

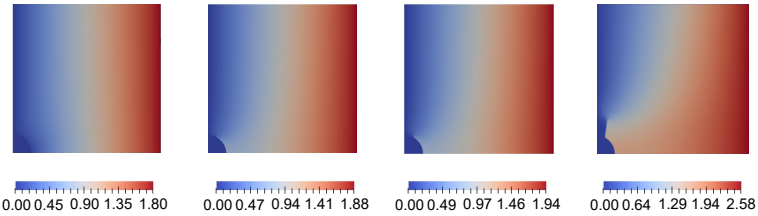

(b) Horizontal displacement u_x (μm)

Figure 32: Micro-mechanics of fiber reinforced composite materials under transverse tensile loading conditions: (a) Damage pattern. (b) Contour plot of the horizontal displacement field.

- Finally, the crack progresses along the matrix, which is reflected by a decrease in the load carrying capacity in the averaged stress-strain curve. In this case (single fiber) the crack progresses without any restriction up to reaching the domain boundary. For interacting fibers, the behavior will be more complex and it will be examined in Section 6.2.3.

It can be noticed that the four stages previously described are in agreement with those identified in (23; 169). To illustrate such a crack evolution, the damage pattern and the horizontal displacement field at the different stages during the simulations are shown in Figure 32. The discontinuity in the displacement field identifies the separation associated with the crack and the progress of failure. In this graph, both micromechanical failure modes, i.e. interface decohesion and matrix cracking, can be clearly identified.

Finally, during the first and the second stage it is remarkable to note that no damage is found in the matrix, see the first two columns in Figure 32. At these stages, damage is localized in the interface decohesion process. Once the abrupt decohesion is produced, a crack begins to nucleate

in the matrix around the interface crack tip. This fact is clearly observable in the third column of Figure 32. This point of nucleation will be the origin of the crack progressing into the matrix, see fourth column of Figure 32.

Symmetry in the crack pattern

The initial geometry and loading conditions of the problem (Figure 30) present two axes of symmetry. According to that, it could be argued that the failure progression should be symmetric with respect to these two axes. In view of the numerical results presented in the previous section, the symmetric solution in this problem corresponds to the onset of two separated decohesion zones at the fiber-matrix interface, symmetric with respect to the y-axis. However, this is not in line with the experimental evidences as discussed in (28) that corresponded to a single (asymmetric) fiber-matrix interface debonding. The reason for that emerges from the condition stating that it is the set of solutions which should fulfill the symmetry conditions and not necessarily each of them. In those problems where only one solution is possible, the direct consequence is that this unique solution is symmetric, e.g. the problems of the linear theory of elasticity. However, in this case the solution is not necessarily unique and the symmetric set of solutions is composed by three different options:

- An asymmetric decohesion on the right side of the fiber-matrix interface.
- An asymmetric decohesion on the left side of the fiber-matrix interface.
- A symmetric decohesion on the right and left side of the fiber-matrix interface.

According to (28), the coupled criterion of finite fracture mechanics (FFM) predicts an asymmetric debond, as observed in the experiments. In that investigation, the authors rigorously analyzed the set of the solutions mentioned above in a separate manner, obtaining that the asymmetric solutions are preferential over the symmetric option. The physical justification for this behavior is attributed to the fact that a symmetric solution with two interface cracks would produce a shielding effect between the two cracks, and as a consequence, a decreasing ability of releasing elastic energy per unit of newly formed cracked area. Thus, from

an energetic point of view, the asymmetric solution is prevailing over the symmetric case.

The comparison between the current PF-CZ methodology and the coupled criterion is herein carried out by studying the different failure scenarios aforementioned and obtaining the corresponding critical loadings. This is possible because the coupled criterion requires the prescription of a geometry for the situation after the occurrence of the damage event. However, the numerical strategy herewith envisaged does not require any assumption associated with the qualitative form of the solution. In such a case, if instead of a quarter of the cell (previously performed) a half of the domain (upper one) is simulated, the symmetric solution with two interface cracks is obtained. The reason is that this is the equilibrium solution detected by the solution algorithm used. In order to promote the asymmetric solution for the comparison purposes, a higher fracture toughness is prescribed in one side of the fiber-matrix interface, acting as perturbation of the symmetric problem.

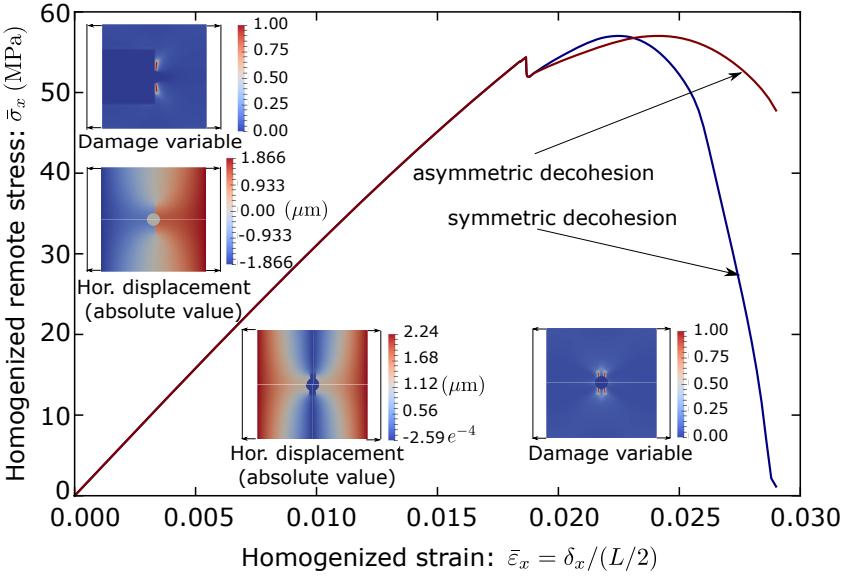

Figure 33: Micro-mechanics of fiber reinforced composite materials under transverse tensile loading conditions: one or two debonds.

Figure 33 shows the comparison of the stress-strain curves for the

asymmetric and symmetric solutions along with the damage patterns through the proposed technique. It should be expected a bigger difference between both critical stresses knowing that the asymmetric case has bigger interface fracture toughness. The justification for this discrepancy is the shielding effect between the two cracks in the symmetric case.

The physical justification for this behavior is attributed to the fact that a symmetric solution with two interface cracks would produce a shielding effect between the two cracks, and as a consequence, a decreasing ability of releasing elastic energy per unit of newly formed cracked area. Thus, from an energetic point of view, the asymmetric solution is prevailing over the symmetric case.

An additional discrepancy between the symmetric and asymmetric solutions is the fact that both solutions lead to different predictions regarding the debonding and kinking angles as we can see in Table 2. In this case, the current method predicts higher kinking angles for the asymmetric case with respect to that corresponding to the two-debonds scenario. As the kinking angle decreases, the extension of the crack propagation into the matrix increases, because the crack is more far apart from the less resistant ligament. However, the snap-back in the evolution response is predicted to occur at the same stress and strain levels in both cases. In light of this discussion, it can be concluded that for the prediction of limit loads, the symmetric solution (and the study of a quarter of the domain) can be considered as a solution with an acceptable level of accuracy.

debonds number	θ_d [°]	θ_k [°]
1	58	74
2	56	60

Table 2: Asymmetric and symmetric case: debonding and kinking angles.

Size effect of the fiber radius

Size effect is a phenomenon inherently associated with fracture and damage mechanics, see (170). The PF approach for bulk fracture has shown to be able to predict the size effect accordingly to experimental observations, see (130). For this problem, a size effect of the fiber radius has been reported (31). In order to evaluate the suitability of the present model to simulate the micro-mechanics of failure in composites, the ability to predict accurately the well-known size effect is herewith examined.

In this concern, the size effect is evaluated here by scaling the whole domain and fiber radius by using the same scaling factor in order to keep the volumetric fraction unchanged. The value of the final imposed displacement is also multiplied by the same factor. Finally the results are compared in terms of homogenized (average) stress-strain curves, so the differences are only attributable to the presence of size effect.

Figure 34 presents the stress-strain curves for several values of the fiber radius. The more remarkable difference is that smaller fibers have significantly higher critical stress. Moreover, this difference is even higher if the maximum stress is compared. For larger fibers, the stress-strain curves seem to tend to the same stress-strain curve. The explanation for this different size effect is that the failure behavior for larger fibers is governed by stress considerations, whereas for small fibers the failure behavior is controlled by energy considerations. Since the stress distribution is independent of the scale, the size effect is inhibited for large fibers, see (31) for a detailed discussion.

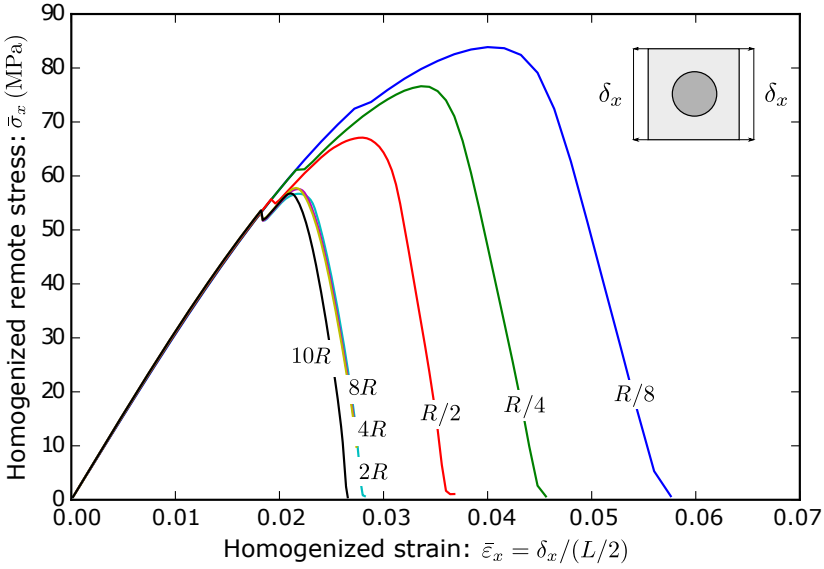

Figure 34: Micro-mechanics of fiber reinforced composite materials under transverse tensile loading conditions: fiber size effect.

Another clear difference is that the behavior is much more brittle

when the fibers have a larger radius. This is reflected in the stress-strain curves after the peak corresponding to the onset of debonding. It can be observed a significant increase in the difference between the stress of debond onset and the maximum stress for small fibers. Furthermore, the energy dissipation is much higher for small fibers, which show a tougher situation. In addition, failure of small fibers is observed for higher strain values. Thus, small fibers correspond to scenarios whereby larger energy dissipation is required.

Figure 35 shows the comparison of the size effect predicted by the present model with the predictions of the coupled criterion of the finite fracture mechanics (FFM). This criterion assumes that a crack onset occurs (a decohesion in this problem) when the next two conditions are fulfilled simultaneously: i) the stresses along the potential crack path exceed the strength and ii) the crack onset is energetically admissible. The FFM model used here for the sake of comparison is similar to the FEM model shown in Figure 30: a circular inclusion surrounded by a very large square of matrix subjected to a uni-axial tension. The stress leading to the debond onset is represented along with the stress for which the crack kinks out the interface. The critical stress for the debond onset predicted by the finite fracture mechanics is also plotted. In this graph, a good agreement can be observed between the current PF-CZM and FFM from both qualitative and quantitative points of view. In particular, from a qualitative perspective, a clear change of tendency is observed around $R = 10$ μm, going from a strong size effect for smaller fibers to a total independence for larger fibers. Finally, at quantitative level, the predictions of the two models are very similar to each other.

6.2.2 Numerical simulations of the single fiber-matrix decohesion problem under transverse bi-axial tension

The analysis of the current inter-fiber failure problem for the single fiber domain is also extended by adding secondary transverse loading. The presence of the secondary stress can notably affect the failure onset and evolution of the present problem. For this purpose, the external loading conditions applied to the system are accordingly modified including a secondary stress σ_y, see Figure 36. The nomenclature henceforth adopted follows the scheme: $\delta_y = n\delta_x$, then for instance the case $n = 1$ ($\delta_x = \delta_y$) yields to a bi-axial tensile state along both perpendicular directions. Note that any plain remote stress state can be reduced to a pair of normal

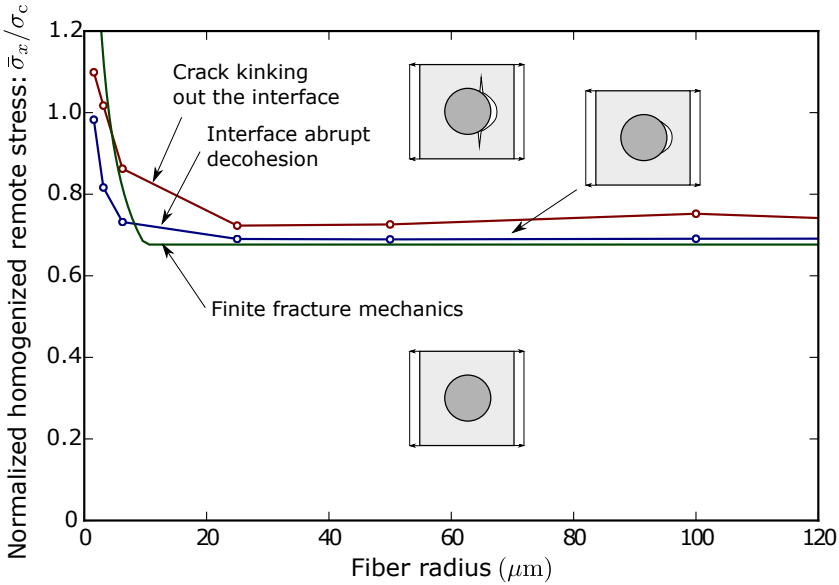

Figure 35: Micro-mechanics of fiber reinforced composite materials under transverse tensile loading conditions: fiber size effect and comparison between the present PF-CZM predictions and those provided by finite fracture mechanics.

stresses along two perpendicular directions, so the results obtained here cover any remote stress state, even including shear stresses.

The corresponding stress-strain evolution curves for the x-direction associated with the current representative scenarios are depicted in Figure 37. From this plot, it can be observed that the load level required for the initiation of growth is greater for larger values of σ_y. The reason is that a secondary tensile stress generates a compression at the interface points where decohesion takes place as a consequence of the different contraction due to Poisson effect of fiber and matrix. Thus, since matrix is more compliant than the fiber, the matrix tends to contract more in the x-direction due to the tensile stress state along the y-direction, producing a compression at the interface points. This compression counteracts the tensile state produced by the main transverse load, making more difficult the onset of decohesion. On the other hand, a secondary compression has the contrary effect, it makes easier the onset of debonding.

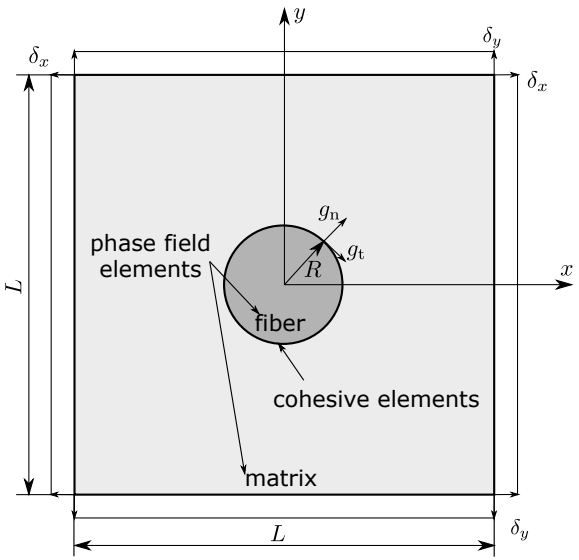

Figure 36: Micro-mechanics of fiber reinforced composite materials under bi-axial tensile loading conditions: geometry and boundary conditions.

In addition, it can be observed in Figure 37 that the presence of a secondary stress also modifies qualitatively the behavior. A secondary tensile stress produces a much more brittle behavior. In fact, in the limit for a bi-axial tensile state ($n = 1$), the failure is totally brittle: an abrupt debond onset occurs spanning the whole fiber-matrix interface. After the total decohesion of the interface, the stresses increase at the matrix, producing the instantaneous failure of the whole matrix domain. In contrast, a much more *pseudo-ductile* and tough behavior is found when the compression is relatively significant. For example, for $n = -1$, the stress-strain curve shows a wide range of strain where the debond is slowly growing along the fiber-matrix interface, the critical strain at failure being almost ten times larger than for $n = 1$.

Figure 38 represents the critical remote stresses (σ_x, σ_y) predicted for the onset of debonding and crack kinking out of the interface. This plot clearly illustrates the effect of the secondary transverse load. This prediction is in agreement with other previous models (171; 172).

With regard to failure initiation, the location of the interface debond-

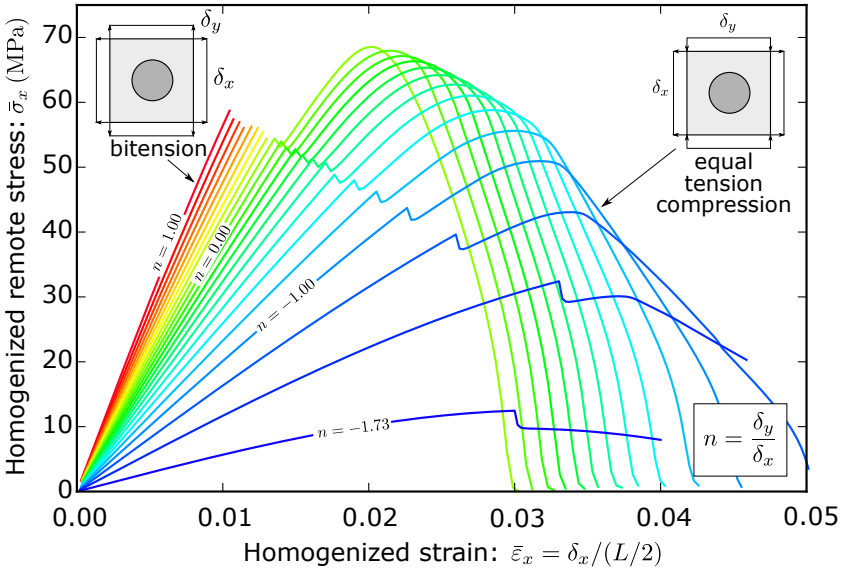

Figure 37: Micro-mechanics of fiber reinforced composite materials under bi-axial transverse tensile loading conditions: homogenized stress-strain curves.

ing coincides with that corresponding to the uni-axial tensile case for low values of the secondary transverse load. As for the unstable fiber-matrix debonding, current simulations estimate lower angles θ_d as the secondary loading increases, being this result in line with (22). When the secondary load becomes more significant, the debond location moves through the interface points more loaded, see Figure 38.

6.2.3 Numerical simulations of the two fiber-matrix decohesion problem under transverse tension

In this section, the importance of the presence of neighbouring fibers with regard to the micro-mechanical failure characteristics in composites is examined. This effect provides a more profound understanding of the fracture processes in fibrous composite materials. The present analysis is restricted to the uni-axial tensile loading as depicted in Figure 39. However, additional cases can be assessed without remarkable limitations.

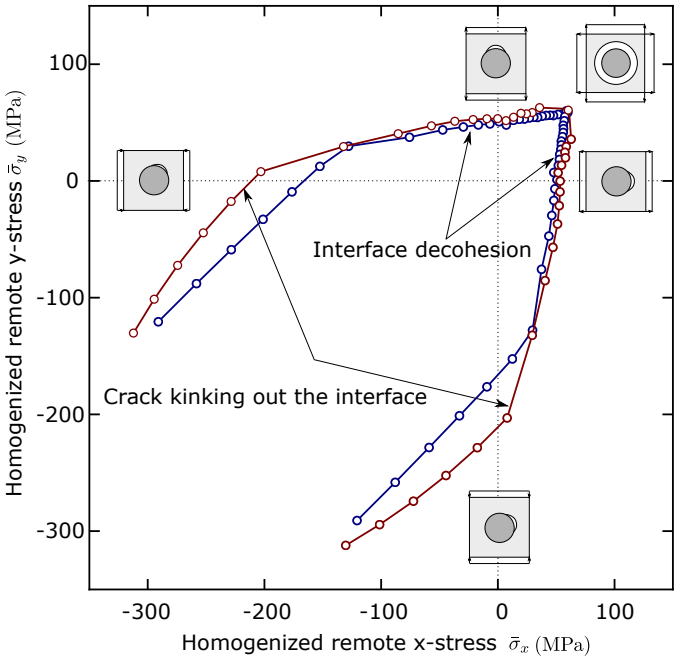

Figure 38: Micro-mechanics of fiber reinforced composite materials under bi-axial transverse tensile loading conditions: critical remote stresses for interface decohesion or for crack kinking out of the interface.

The model comprises a main fiber and a secondary fiber, whose position is modified in order to explore different cases. In the current study, complying with standard fiber volume fraction for hexagonal packing, the initial distance between both fibers is set equal to the following values: $d_f = [2.116R, 2.6R, 3R]$, where R=0.0125 mm stands for the fiber radius. Initially, the angle between the fibers α_f is equal to 45°.

The stress-strain evolution curve of the system is depicted in Figure 40 for different values of the distance between the fibers but keeping unchanged the relative angle between them. This graph evidences that a quasi-identical initial linear elastic phase of the response can be observed for the chosen distance values. Furthermore, the evolution curves display a first sudden drop which is associated with the unstable debonding event of the secondary fiber. Note that this point is slightly affected by the inter-fiber distance, obtaining higher values as d_f increases.

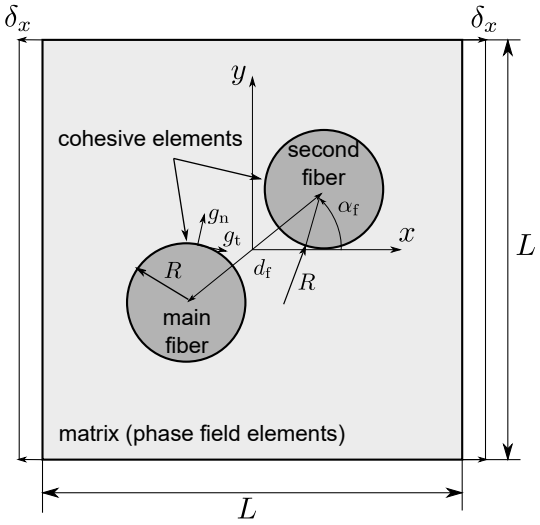

Figure 39: Two-fibers model: geometry and boundary conditions.

After that, the second stage of the evolution is characterized by the stable fiber-matrix debonding of the secondary fiber. This second stage concludes when the unstable interface decohesion in the main fiber occurs, being characterized in the stress-strain evolution by a second drop. Again, this second debonding takes place at higher load levels for increasing d_f values.

Progressing on the loading path, the third phase comprises the stable interface failure of the main fiber till this crack tends to kink out towards the matrix. During the simulations, it is observed that this kinking progresses till reaching the secondary fiber interface crack. After this, subsequent kinks of interface cracks at the main and secondary fibers towards the matrix take place. The final phase of the present response features a notable stiffness degradation for each of the cases under consideration upon complete failure, whereby the larger d_f is set, the higher maximum load value is obtained. Moreover, to point out that, the debonding and kinking angles increase as the distance between fibers increases, see Table 40.

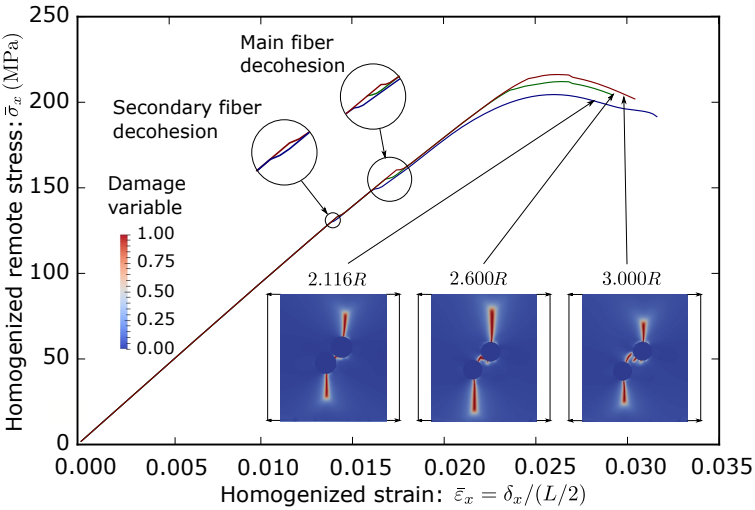

Figure 40: Micro-mechanics of two fibers reinforced composite materials under transverse tensile loading conditions: influence of the distance between fibers on the stress-strain evolution curve.

d_f $[mm]$	$\theta_{d,SF}$ [°]	$\theta_{d,MF}$ [°]	θ_k [°]
$2.116R$	90	39	118
$2.6R$	102	47	142
$3R$	112	51	151

Table 3: Two fibers problem: influence of the distance between fibers on the debonding and kinking angles.

It is worth mentioning that differing from alternative approaches (173), the current methodology endows a robust and reliable competition of the different failure mechanisms throughout the simulation and without the user intervention.

The effect of the position of the secondary fiber with respect to the main one is also studied. Fixing the distance between the fibers equal to d_f =2.116R, the following secondary fiber angles $\alpha_f = [30°,\ 45°,\ 60°]$ are studied. The obtained predictions are displayed in Figure 41. From this graph, it can be observed that, there exist two drops on the stress-strain evolution curve in the case of 45°. Conversely, for the remaining cases, only one drop along the evolution which corresponds with the unstable

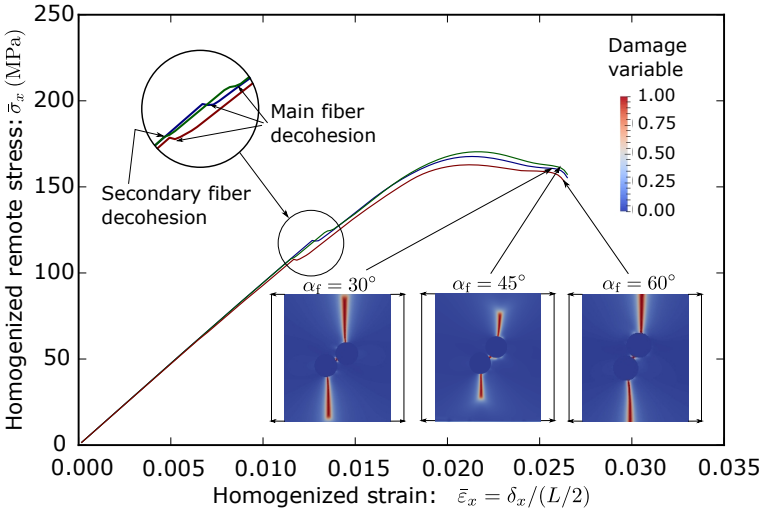

Figure 41: Micro-mechanics of two fibers reinforced composite materials under transverse tensile loading conditions: influence of the angle between fibers on the stress-strain evolution curve.

debonding of the main fiber is predicted. From the quantitative perspective, it can be also deduced that for configurations with an individual instability in the evolution, the interface crack onset requires higher load levels as the angle decreases. However, in the case of configurations with two instabilities, the highest snap-back load is found.

α_f [°]	$\theta_{d,SF}$ [°]	$\theta_{d,MF}$ [°]	θ_k [°]
30	NO	51	113
45	90	39	118
60	NO	76	135

Table 4: Two fibers problem: influence of the angle between fibers on the debonding and kinking angles.

It can be observed that the debonding and kinking angles are predicted to increase for higher angles between fibers, see Table 4. The only exception is the debonding angle of the main fiber for the $45°$ case, because is the smallest one due to the presence of a previous instability.

6.3 Fracture in cross ply laminates

In this section, to provide a further insight on the micro-mechanical response of composites, a significant attention is devoted to the analysis of the transition between micro-cracking events, which have been deeply analyse in Section 6.2, to meso-scale damage. With this aim, a new numerical model based on the phase field and on the cohesive zone model has been proposed for the simulation of fracture in cross ply laminates. The section is organized as follows: the construction of the numerical model is detailed in Section 6.3.1, whereas the results and discussions of the simulations carried out are presented in Section 6.3.2. It is worth noting that, all the simulations are performed with the finite element program `ABAQUS` and under displacement control.

6.3.1 Computational model

This section describes the generation of the micro-mechanical model under analysis. Particular details with regard to the geometry, its discretization, the loading conditions and the constitutive laws and crack modeling techniques employed for each entity, are detailed and justified in the forthcoming paragraphs.

Current FE models are generated through the adoption of a high-fidelity multi-scale embedded approach similar to that employed in (33; 60; 61; 63), with the aim at replicating the experimental configurations described in (11). Schematic description of the domains are depicted on the top of Figure 42, where the central region of interest is highlighted. As is described in detail below, the tensile loading conditions along the longitudinal directions of the specimens at the experiments are transferred to the central area via prescribed displacement conditions (denoted by δ_x in Figure 42). Excluding grip tabs, the specimens correspond to standard cross ply laminates, which are composed by three layers: two outer layers (0° layers) with fibers orientated along the loading direction, and a central layer with fibers perpendicular to the loading direction (90° layer). Note that the present simulations comprise a sufficiently long section for each specimen using a plane strain formulation, see Figure 42, and whose respective dimensions are reported in Table 5. As can be observed in this graph, three different models are generated according to the three types of specimens tested in (11). The difference between these three models relies on the thickness of the central 90° layer, ranging from 0.04 mm to 0.16 mm. In contrast, the thickness of each individual 0° layer

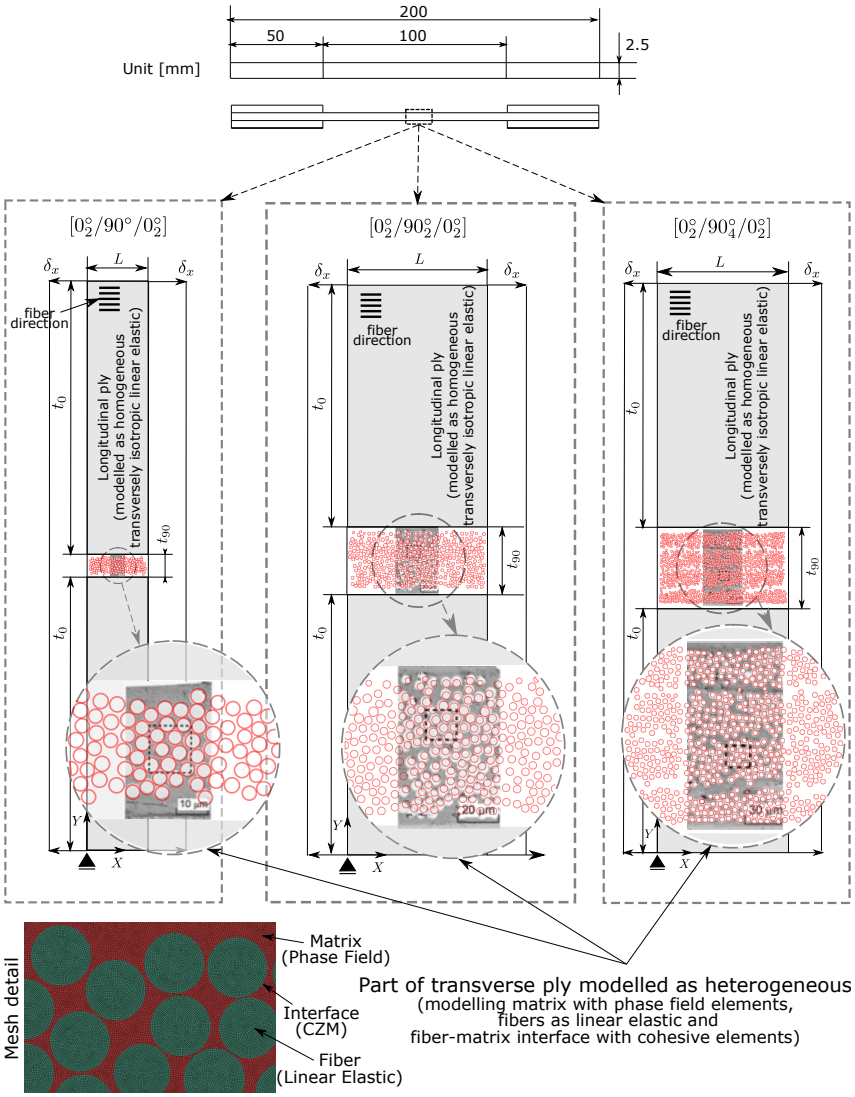

Figure 42: Details of the computational models generated to simulate the (11) experiments.

is equal to 0.24 mm. Thus, the stacking sequences of the current models correspond to: $[0^\circ_2/90^\circ_n/0^\circ_2]$ being n = 1, 2 and 4.

Material	E [GPa]	ν	$\mathcal{G}_C$ [N/mm]	l [mm]
Fiber	13	0.2	-	-
Matrix	2.79	0.33	0.02	0.00105

Material	E_{11} [GPa]	E_{22} [GPa]	E_{33} [GPa]	ν_{12}	ν_{13}	ν_{23}
Homogeneous 0° ply	113.5	8.31	8.31	0.3	0.3	0.45

Interface Property	σ_C [MPa]	$\mathcal{G}_C$ [N/mm]
Fracture Mode I	75	0.002
Fracture Mode II	100	0.04

Geometrical parameters	$[0^\circ_2/90^\circ/0^\circ_2]$	$[0^\circ_2/90^\circ_2/0^\circ_2]$	$[0^\circ_2/90^\circ_4/0^\circ_2]$
Laminate length [mm] (L)	0.4	0.8	1.6
90° layer thickness [mm] (t_{90})	0.04	0.08	0.16
0° layer thickness [mm] (t_0)	0.48	0.48	0.48

Table 5: Material properties (11; 12; 13) and geometrical parameters of the $[0^\circ_2/90^\circ_n/0^\circ_2]$ (n = 1, 2 and 4) laminates.

Focusing on the central parts of Figure 42, for each configuration, the geometry is composed by three entities (regions), representing the three layers. The outer 0° layers are modelled as homogeneous solids, whereas for the 90° layers, the actual micro-structure is specifically taken into account. This is performed by modeling such domains as heterogeneous regions with two different phases (i.e. fibers and matrix) and the corresponding interfaces. These micro-structures are identified by means of an in-house Python script that allows the rapid transfer of the geometrical information for the subsequent operations in the modelling process to be performed. Nevertheless, note that due to the fact that a reduced region of the micro-scopic fiber distribution is available in (11) for each configuration, the corresponding representative region of the micro-structure is defined and reproduced throughout the 90° plies in order to preclude undesirable edge effects upon loading.

Regarding mesh details, at the micro-mechanical level, very finely discretized 90° plies are generated (Figure 42). These dense meshes are constructed in order to fulfill with the requirements of the different constitutive laws applied to each part of the geometry. In particular, the mesh is fine enough in the *Observed area*, in order to adequately model the process of crack events which occurs at this zone.

With reference to the simulation capabilities, different modeling techniques are defined within the models, which are selected in terms of several arguments: (i) the nature of the region itself, (ii) the typical failure

behavior, and (iii) the level of interest of the region:

- The 0° layers are modelled as homogeneous orthotropic linear elastic solids with the material properties detailed in Table 5. No damage is expected to occur in these layers during the first stages of the failure mechanism herewith studied. Thus, a linear elastic constitutive law is considered to adequately represent the mechanical performance of this region of the models.

- Interface behaviors between 0° and 90° layers are simulated as a perfect interface. It is well known that the failure mechanism studied here leads to subsequent delaminations between such layers (174). However, this mechanism is out of the scope of the present study.

- Fibers in the 90° layer are modelled to follow an homogeneous isotropic linear elastic response. Fibers actually obey a transversely isotropic response. However, within the current plane strain formulation, their mechanical performances are assumed to comply with the corresponding equivalent plane strain properties, see Table 5. Similarly to the 0° layers, no damage is expected to occur inside the fibers during the first phases of the failure mechanism studied in the present study. Actually, some micro-graphs show rarely transverse breaks of fibers, but the relevance of this phenomenon is not common enough to be of remarkable significance in the failure process. In fact, no fiber breakage was reported in (11).

- Matrix within the 90° layers is modelled as homogeneous and linear elastic isotropic entities. During the failure processes, damage and cracks are expected to progress within the matrix, so it is required to reproduce such cracking phenomena with a proper level of reliability. In this direction, it is worth mentioning that modelling of crack events at the micro-scale level is very challenging and complex because such cracks progress from very short cracks, whose failure is governed by a stress criterion, to large cracks, whose failure is mainly governed by the classical Griffith energy criterion (LEFM). Thus, in our vision, modelling matrix crack events either using LEFM (which it is not able to accurately predict the behavior of small cracks at this scale) or a stress-based criterion, via e.g. a combination of damage-yielding model, (that it is not able

to predict well the behavior of large cracks) might present significant limitations. In order to overcome these issues, the adoption of robust numerical frameworks that enable predicting both behaviors is a matter of enormous importance. In this concern, cohesive zones models (CZMs), finite fracture mechanics (FFM), or phase field (PF) can be understood as suitable modeling tools for crack events which fulfill with the previous requirements. In particular, these three approaches have been assessed for recovering both extreme scenarios (stress- and energy-dominated crack phenomena) and the transition between them with excellent results, see (126; 175). Thus, for the matrix cracking, since the crack paths are a priori unknown, the phase field (PF) strategy is herewith exploited due to its extraordinary capabilities in terms of reproducing very complex crack paths without the use of arduous re-meshing and crack tracking methodologies in the corresponding FE implementation. This fracture model (PF) is implemented as user-defined element UEL into the general purpose package `ABAQUS`. As it is widely known, user element data cannot be visualized in `ABAQUS`. For that reason, we combined the UEL with an UMAT transferring the output variables of the UEL to the state variables of the UMAT by a common block. This UMAT is assigned to additional standard elements (dummy elements) which have the same nodes and connectivity as the user element layer but different numbering. Thanks to this coupling, the user element data is visualized by the state variables of the dummy elements.

- In addition to matrix-dominated cracks, based on experimental observations, failure mechanisms in the current specimens presented significant fiber-matrix debonding events (11). In order to model such phenomena, fiber-matrix interfaces within the 90° layers are modelled using CZMs as described in Section 5.2, obeying a bilinear TSL. Note that, similarly to the matrix, in this case, the average fiber-matrix crack size is small enough to be comparable to the fracture process zone. Thus, a predictive approach based exclusively on a LEFM analysis would present some limitations for the accurate estimation of the crack growth along the fiber-matrix interface. Interfacial cohesive properties are detailed in Table 5 and the interface initial stiffness K is set equal to 1×10^{8} [MPa/mm] for fracture modes I and II (12).

Regarding the prescribed boundary conditions, in line with the previ-

ous description, the external solicitation corresponds to prescribed horizontal displacements δ_x at the left and right extremes of the models. A fixed loading increment is prescribed, which is directly proportional to the individual model length L, in order to keep constant the corresponding strain increment for each model. In addition, a point is fixed at the left bottom corner in order to avoid rigid motions.

Finally, due to the fabrication procedure of the actual specimens, it is expected to find a certain level of residual thermal stresses within the domain at the layer scale. Thus, the strain levels advocated in the present results are computed in such a way that the consideration of the residual thermal stress are already incorporated. These thermal effects are calculated according to the procedure described in (176).

6.3.2 Results and discussion

This section presents the results obtained from the computational models corresponding to the micro-mechanical response of the cross ply laminates described above. Furthermore, the present section addresses a comprehensive discussion in terms of the reliability and capabilities of the current numerical methodology.

The objective is to investigate the process of initiation of a crack from the very first form of damage to a crack spanning the whole 90° layer, which can be already considered a meso-mechanical crack. The influence of the 90° layer thickness on this process is also analysed through the comparison of the present estimations for the three specimens with different thickness values and with respect to the available experimental data (11). Furthermore, it is of remarkable interest the way through which cracking events evolve at the micro-scale of the current models, since they provide a very valuable information in terms of the nature of damage progression. The careful analysis of the simulation data herein conducted can lead to a plausible understanding of the causes of the *in-situ* strength effect.

The forthcoming discussion is articulated in three individual stages based on the sequence of damage events identified throughout the simulations. First, the process of cracking initiation is analysed for each specimen, focusing on the different phases at the micro-mechanical level. Second, the computational results are correlated with the experiments reported by Saito et al. (11). Finally, the results are discussed in a global context, specifically, paying special attention to the comparison with respect to different models already proposed in the related literature.

Process of crack initiation at the layer scale from a micro-mechanical analysis: from micro-mechanical cracking to meso-scopic damage

The detailed analysis of the progress of damage and cracks within the current micro-mechanical models clearly reveals the different phases of failure processes (Figures 43-46). Specifically, failure maps corresponding to the interface damage variable and phase field-crack at the matrix are shown in Figures 43, 45 and 46, pinpointing the different cracking sequences (identified by numbers) which are represented by the damage variables for fiber-matrix delamination and matrix failure. As expected and in line with the experimental observations (11), cracks principally evolve along the direction transverse to the external loading. The comprehensive description and discussion with regard to the different phases of the crack events for the three specimens under analysis is outlined as follows:

- First, according to the computational results, the first damage event corresponds to the onset of a debond at the fiber-matrix interface (labelled as phase 1 of the crack evolution in Figures 43, 45 and 46). The position of this debond occurs at the zone of the interface where the normal stresses achieve the corresponding highest levels, which is generally identified at narrow portions of the matrix between fibers (12; 60). Advocating previous studies regarding the stress solution for a circular inclusion in a infinite domain under remote tensile stress (177), the critical point for such decohesion corresponds to one of the poles leading to a non-symmetric post-failure configuration. This event is accurately captured by the current simulations since this initial debond is predicted to occur at one of the two critical locations (phase 1) (28). Moreover, it has been extensively reported that the very first initial debonding process is an unstable phenomenon but it becomes stable in subsequent stages (15; 28; 172). This development (unstable-stable) is a direct consequence of several factors comprising the transition from fracture mode I to II along the interface, the mismatch between the mechanical properties of the fiber and the matrix, among others.

- The second fracture stage identified in computational results is the appearance of several debonds at different fiber-matrix interfaces (phases 2 and 3 in Figures 43, 45 and 46). These interface cracks can take place relatively far from the first debond, but depending upon on the particular fiber positions. The reason for this event is at-

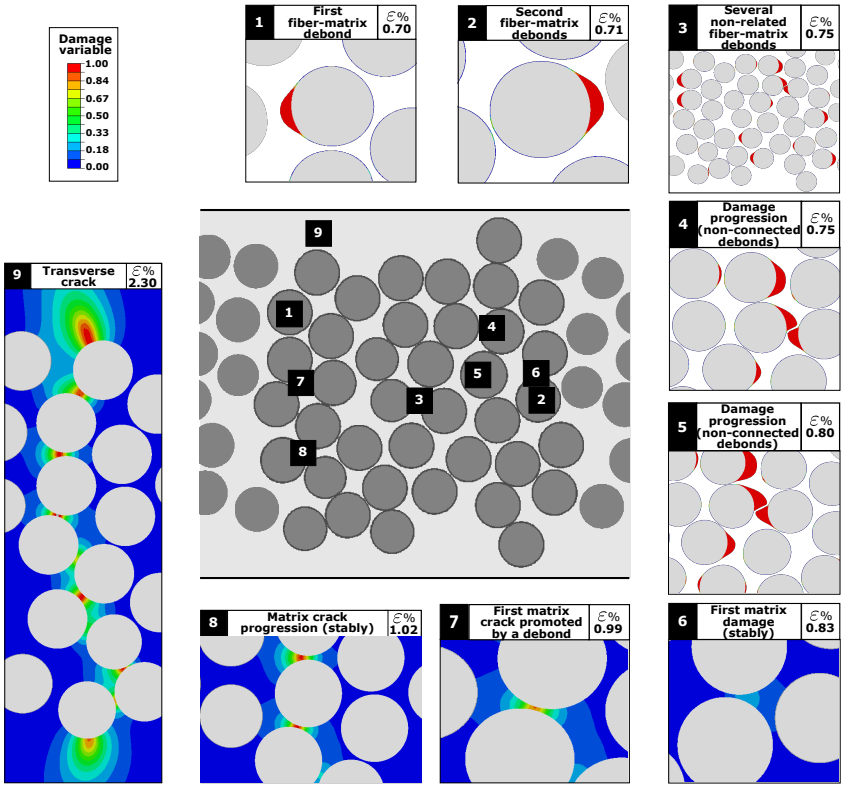

Figure 43: Sequence of damage events observed in the computational results for $[0_2^\circ/90^\circ/0_2^\circ]$ laminate.

tributed to the fact that the stress state around an intact fiber-matrix interface is very similar for most of the fibers (for the prescribed tensile loading), but with slight modifications due to geometrical aspects associated with the micro-structural arrangement, e.g. relative position of the neighbouring fibers (178; 179). Thus, several fibers with similar situations in terms of stresses, can be found in a micro-structural system. Correspondingly, for a certain strain level, it is expected to observe several isolated debonds. It is also noting that such debonds are prone to occur at the fibers with a preferential neighbouring situation, which promote the occurrence of such failure. Moreover, in all the cases here analyzed, the fiber-matrix

damage progresses at different locations up to their corresponding critical conditions prior to kinking towards the matrix, this effect being in good agreement with experimental observations.

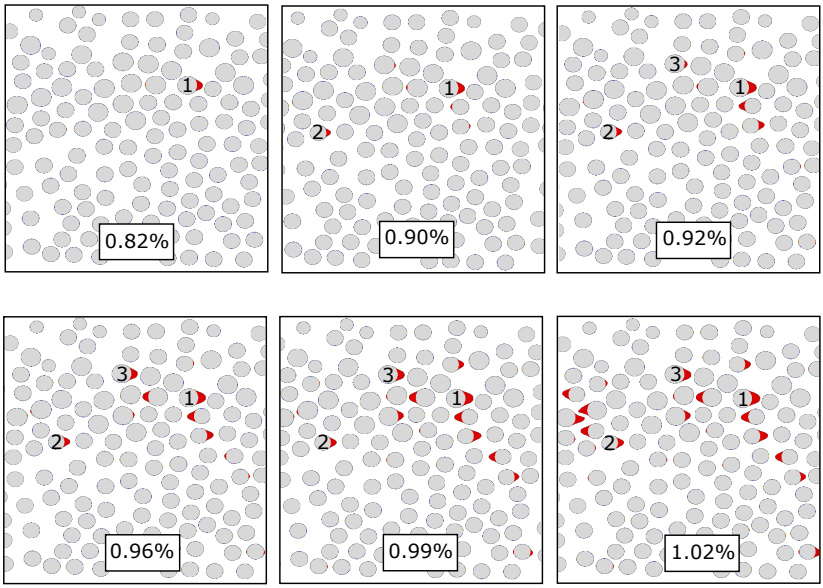

Figure 44: Detail of evolution of debonds at the first stages of damage initiation for $[0_2^\circ/90_2^\circ/0_2^\circ]$ laminate. Values showed in labels correspond to the strain level.

- The third phase observed in the present simulations can be already considered as an initial stage of damage which can have a noticeable relevance at the meso-scale (phases 4 and 5 in Figures 43, 45 and 46). The presence of fiber-matrix debonds notably alter the stress state at such locations, leading to two possible alternative scenarios upon fracture progression: (i) the further promotion of the fiber-matrix debonding in neighbouring fibers, or (ii) the protection of nearby fiber-matrix interfaces. This idea is illustrated in Figure 44, whose main conclusions are summarized:
  - In situations where a first exemplary debond is initiated at a particular location (1), in posterior loading stages, a second debond can take place at a different fiber (2), which is

relatively far from the first one (complying with the second scenario aforementioned). The reason for which these first two debonds take place at these particular locations is directly attributed to the particular arrangement of fibers. Notwithstanding, in the case of numerical studies based on statistical distributions of fibers positions, the particular location of the first debond would be also affected by this scatter.

- Continuing the analysis and evidencing the concomitant occurrence between the promoting and protective interface failure mechanisms, which depends on the status of surrounding fibers, it is observable that: whereas the fiber-matrix interface failure at fiber (1) evolves in a larger damaged zone with other neighbouring debonds aligned with the main loading direction, the debond at fiber (2) does not promote any further interface cracks at its surrounding area. In fact, subsequent debonds, as that identified by (3) in this graph, contribute to the progression of additional interface failure phenomena. Note that the connection between such debonding failure at the micro-scale may produce a meso-scale crack event.

Once the damaged regions (formed by aligned debonds) have been clearly developed, the progress of such phenomena is diverse. At this phase, several fiber-matrix debondings can further propagate in a stable manner up to the attainment of the next energetic barriers, which can correspond to the relative positions of the fibers, the presence of resin-rich regions, among others. Note that these energetic barriers are statistically distributed within the domain based on its own internal arrangement. The delay in posterior damage propagation leads to an accumulation of energy within the system, so that such energetic barriers can be overcome leading to unstable (sudden) damage evolution.

- The next stage here identified comprises the fact that fiber-matrix interface failures generally span the whole thickness of the 90° layer. This happens prior the occurrence of any crack kinking phenomenon towards the matrix in the whole thickness of the 90° layer as is shown in Figures 43, 45 and 46, and subsequently in Figures 47, 48 and 49. This behavior strongly depends on the corresponding matrix and fiber-matrix fracture properties.

- Upon loading progression, significant damage matrix events are

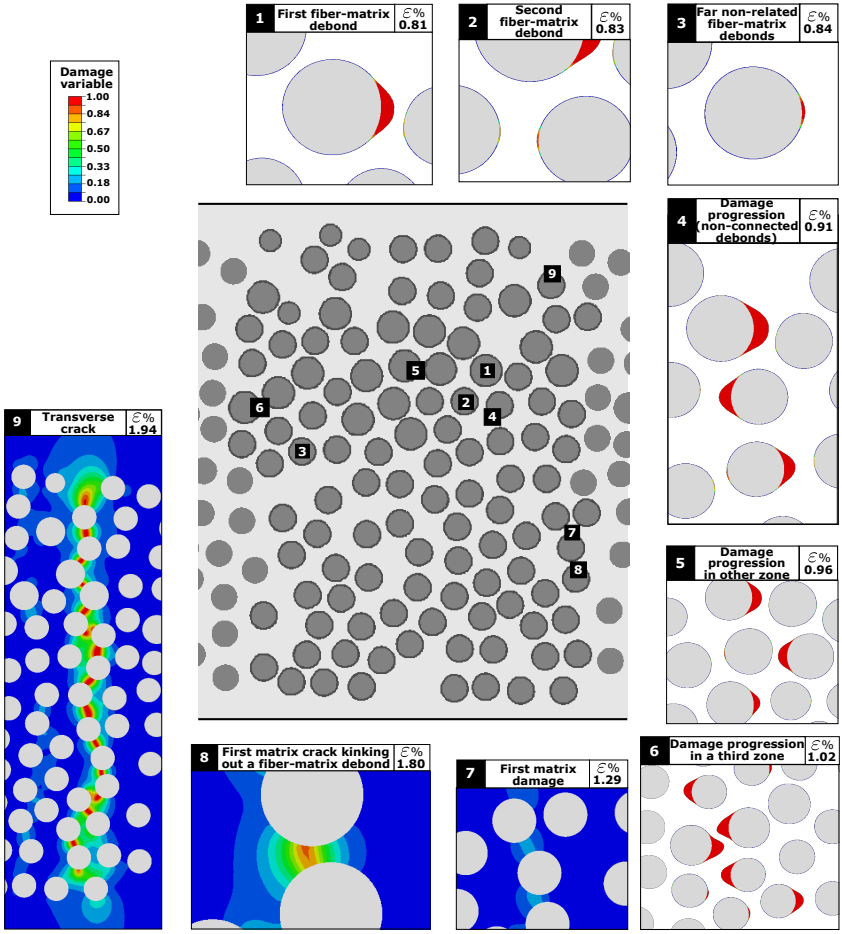

Figure 45: Sequence of damage events observed in the computational results for $[0_2^\circ/90_2^\circ/0_2^\circ]$ laminate.

predicted at the micro-scale, which, as expected, take place in the neighbourhood of several fiber-matrix debond tips (see phase 6 in Figures 43, 45 and 46). This is the previous step to the appearance of a matrix crack promoted by the fiber-matrix debonds. Since the size of the process zone in this problem is of the order of the fiber radius, it is expected to have a significantly large damaged zone

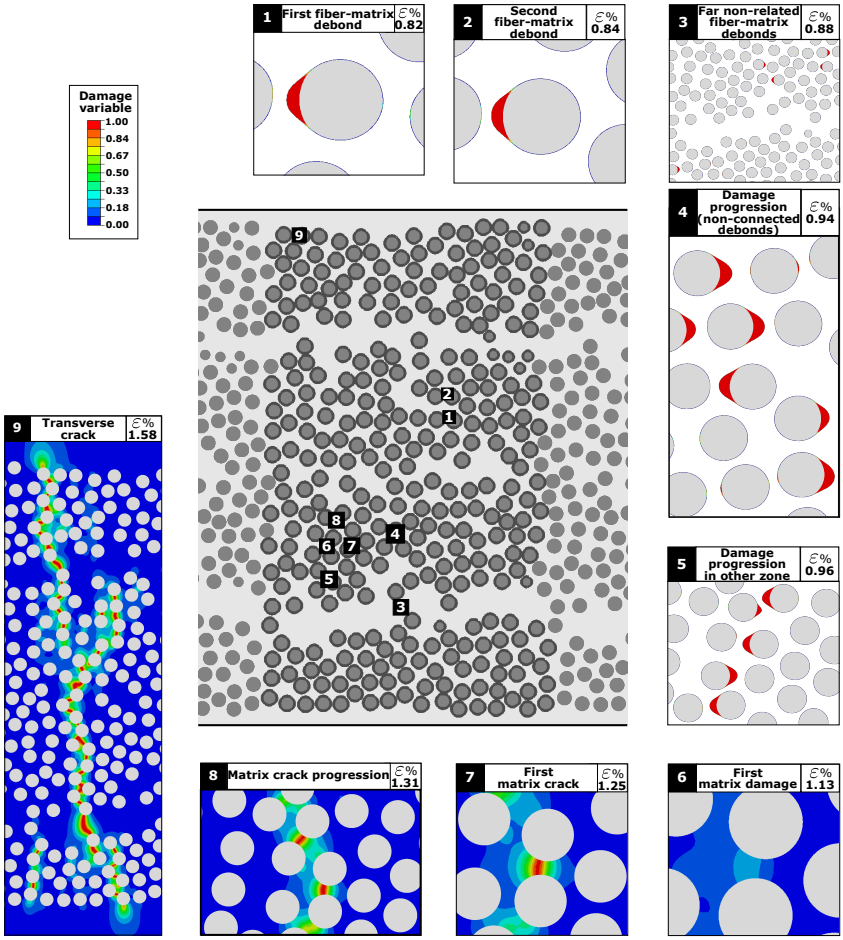

Figure 46: Sequence of damage events observed in the computational results for $[0_2^\circ/90_4^\circ/0_2^\circ]$ laminate.

before the corresponding kinking phenomenon.

- The posterior stage concerns the nucleation of a matrix crack in the damaged zone near a debond tip (see phases 7 and 8 in Figures 43, 45 and 46). This matrix crack connects two debonds of neighbouring fibers. The preferential path is mainly perpendicular to the

loading direction, in consonance with the experimental evidences (11) and alternative numerical studies (60; 61). However, the specific direction is mostly governed by the connection between the debonds already existing at the fibers.

- Once the first matrix crack appears connecting two debonds, this crack progresses up to spanning almost the whole thickness of the 90° layer (stage 9 in Figures 43, 45 and 46). This crack can be already considered a damage event at the meso-scale. Thus, this phase can be considered as the final transition between micro-scale cracking and meso-scale damage. The stability of this progression is mainly ruled by the presence of energetic barriers which interrupt further progressions. Current computational results predict that this process is generally unstable with some differences depending on the 90° layer thickness. It is also interesting to observe the final geometry of the fully transverse crack. Thus, in the case of the 90° layer would have been studied as an equivalent homogeneous solid, the preferential crack geometry would correspond to a straight crack perpendicular to the loading direction. However, this is not exactly what it is observed in the computational results presented here. At the micro-mechanical level, the actual heterogeneity of the specimen, in particular when some damage events have occurred, e.g. the distribution of debonds, promotes alternative crack paths with more chaotic topology. This is particularly significant for the thickest laminate here analyzed, see Figure 46.

Comparison with experimental results

This section outlines the comparison between the experimental results in (11) and the predictions obtained from the current computational models. The main target is to assess the influence of the 90° layer thickness on the onset and propagation of through thickness cracking events in line with (12; 60; 61). The current correlation relies on performing a comparison between the three states reported by Saito et al. (11) for each model (corresponding to three strain levels) with respect to similar damage extents in the current computations. Correspondingly, it is possible to compare the strain levels for which the computational models predict "similar" damage levels to those reported in the experimental study. Note that this comparison is focused on the analysis of the micro-graphs given in (11). Moreover, it is worth mentioning that the 2D simulations

here presented cannot take into account "tunneling effects", and therefore deviations with respect to the experimental data are expected in terms of characteristic strain values and cracking topology. These deviations are also affected by the deterministic character of the study.

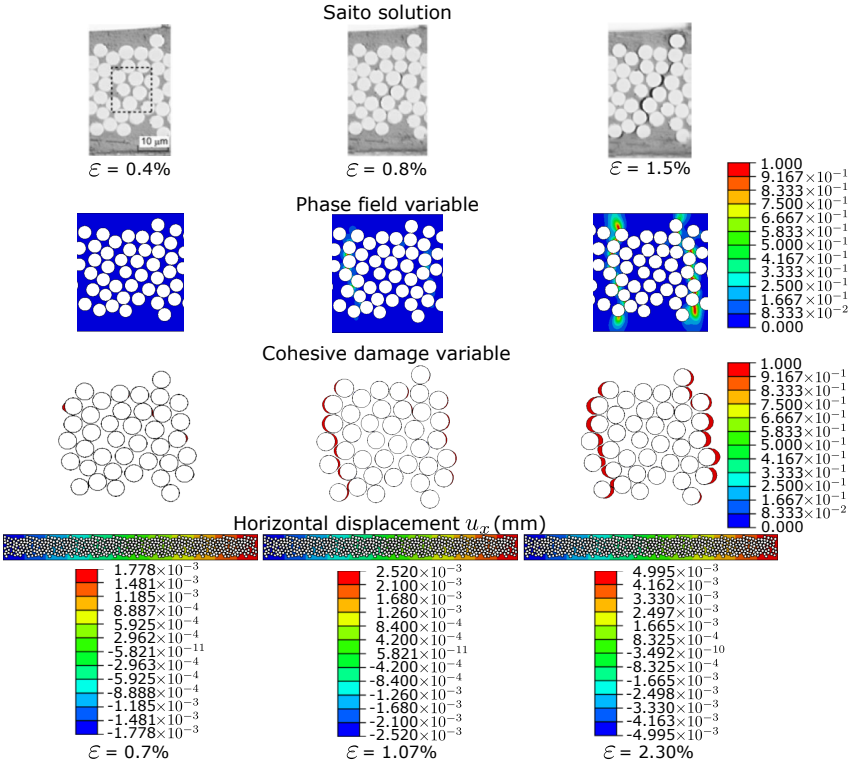

Figure 47: Saito (11) $[0_2^\circ/90^\circ/0_2^\circ]$ laminate results: Saito results, strains (ε), damage patterns, debondings and contour plot of the horizontal displacement field.

Figure 47 presents the comparison for the thinnest laminate with 0.04 mm in thickness of the 90° layer. As discussed in the previous section, damage started by the fiber-matrix interface debondings, which subsequently progressed in neighbour fibers and finally kinked towards the matrix forming a through the thickness crack. This sequence of cracking events is correctly reproduced by the present simulations. Thus, the first column of this graph corresponds to the appearance of the first debond-

ing event at the fiber-matrix interface, which was identified in the experiment at a strain level of $\varepsilon = 0.4\%$, whereas the current computational model predicts the first debond at $\varepsilon = 0.7\%$. As the applied strain increases, subsequent damage states evolve. Thus, the second column is referred to the first cracking state formed by several aligned debonds. According to the experiments, this occurred for $\varepsilon = 0.8\%$ whereas a strain level equal to $\varepsilon = 1.07\%$ is identified for the predictions of the computational model. Finally, the third column identifies a crack spanning almost the whole thickness of the 90° layer, this taking place for $\varepsilon = 1.5\%$ in the experiments whereas the similar status is achieved at $\varepsilon = 2.30\%$ according to the computational model.

Note that the position of the damage and cracking events notably diverges from the experimental observations to the computational estimations. As was amply discussed in previous studies, this result is expected because this is the classical problem of multi-site nucleation for damage, where many very similar points with critical conditions there exist, such locations being of potential damage initiation. In this case, these points correspond to the fiber-matrix interfaces with a very similar situation between them at the beginning of the failure mechanism. Therefore, the point at which the damage is finally nucleated at first is determined by very slight differences in geometry, elastic and fracture properties. The geometry is the only source of such diversity in the current computational model and not completely, due to the fact that small differences in the distributions of fibers at alternative placements of the laminates can affect the occurrence of this phenomenon.

As for the strain level, the comparison shows a relatively good agreement between the experiments and the computational model. The difference can be associated to the influence of the 3D effects, i.e. crack tunneling aspects. In particular, these effects can be very relevant for the first debonds occurring at the free edge locations. The problem in this initial stage is therefore highly 3D due to a high stress concentration which results from the different properties of fiber and matrix and the presence of a free edge.

Figure 48 depicts the comparison for the intermediate in thickness laminate, i.e. 0.8 mm in thickness. With respect to the damage pattern, the first column shows the very first debond, which occurred at a strain level of $\varepsilon = 0.4\%$, whereas the computational model predicts this event at $\varepsilon = 0.81\%$. In the second column, the first damage formed by several aligned debonds can be observed. According to the experiments, this took place for $\varepsilon = 1.2\%$, whereas the computations predict this event at

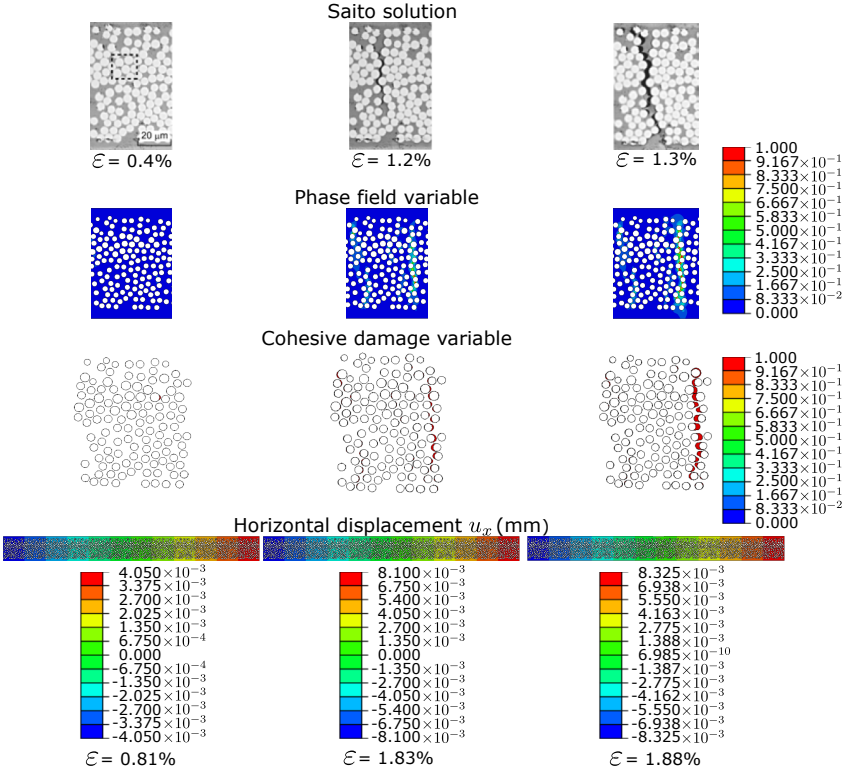

Figure 48: Saito (11) $[0_2^\circ/90_2^\circ/0_2^\circ]$ laminate results: Saito results, strains (ε), damage patterns, debondings and contour plot of the horizontal displacement field.

$\varepsilon = 1.83\%$. Finally, the third column correspond to a crack spanning almost the whole thickness of the 90° layer, this happening for $\varepsilon = 1.3\%$ in the experiments and $\varepsilon = 1.88\%$ according to the computational model. Note that the criterion about the prediction of the situation for damage and crack initiation also holds for this model. In this configuration, experimental and computational model results present notable deviations. These discrepancies are mainly attributed to the specific damage identification criterion herewith adopted.

Figure 49 presents the comparison for the thickest laminate, complying with 0.16 mm in thickness of the 90° layer. In line with the previ-

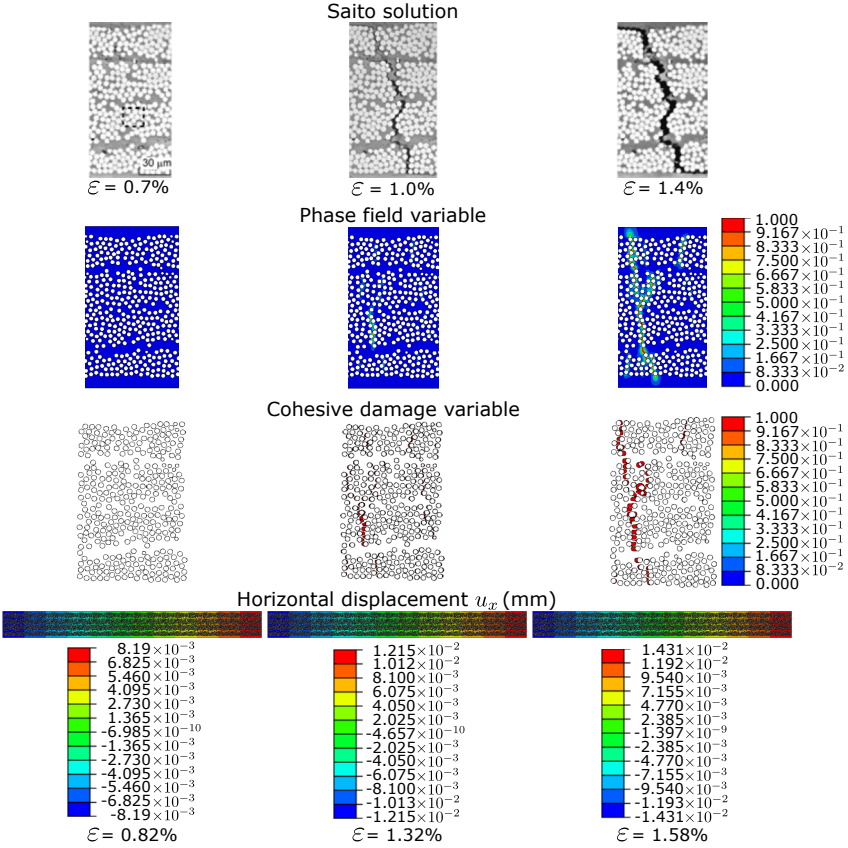

Figure 49: $[0_2^\circ/90_4^\circ/0_2^\circ]$ laminate results: Saito results, strains (ε), damage patterns, debondings and contour plot of the horizontal displacement field.

ous results, the first column of this graph corresponds to the appearance of the first debond, which occurred at a strain level of $\varepsilon = 0.7\%$ in the experimental study (11), whereas the computational model predicts the first debond at $\varepsilon = 0.82\%$. The second column stands for a state with the presence of transverse crack identified by the presence of multiple fiber-matrix debondings. According to the experiments, this occurred for an applied strain equal to $\varepsilon = 1.0\%$, whilst this situation is achieved in the current computations for $\varepsilon = 1.32\%$. The third column identifies a crack spanning almost the whole thickness of the 90° layer, this hap-

pening for $\varepsilon = 1.4\%$ in the experiments and $\varepsilon = 1.58\%$ according to the computational model. For this model the agreement between the computational model and the experiments is better than the previous ones. This could be connected with the idea of that failure for thin laminates is more governed by 3D phenomena (not taken into account here) than for thick laminates, as claimed by some works (180).

Once the current results have been described and contrasted with respect to available experimental data from a quantitative standpoint, it is interesting to perform a qualitative discussion of the predictions. In this context, it is noting that the *in-situ* observations reported in (11) identified that, for thicker 90° layers, the formation of a transverse crack experiences a rapid propagation through the thickness. This contrasts with the case of the thinnest specimen, whose simulations exhibit a more stable through the thickness crack propagation with increasing values of the applied strain, leading to higher values of the final failure strain. This trend is well captured in the present predictions, with the capacity to simulate damage events of different signatures and extent with physically-sound fracture models.

Size effect of the 90° layer. Comparison with the main theoretical models

This section analyses the role of the 90° layer thickness on the different steps of the failure mechanism, from the first fiber-matrix debonding event to the full transverse crack. Therefore, the current discussion allows the assessment of the *in-situ* strength behavior in conjunction with tracking the transition between micro-cracking to meso-scale damage scenarios.

Figure 50 reports the strain level at which the main characteristic phases of the failure mechanisms are identified in the computational results as a function of the 90° layer thickness.

For the first step, which corresponds to the initial fiber-matrix debonding failure, it can be observed that the strain level is almost independent of the 90° layer thickness. The reason for this is clear, this event is mostly sensitive to the elastic properties of fiber and matrix, fracture properties of the interface and fibers radius, see e.g. (13). Since these parameters are very similar to each other for the three models herein presented, it is expected to obtain a similar strain level for this first event. Note however that, in a lower level of influence, the situation of the neighbouring fibers can also play minor influence. Thus, the presence of more pref-

erential situations in some models or slight micro-mechanisms of stress concentrations as fiber clustering is the main source of the slight differences between the current computations.

For the second event, which stands for the first debond kinking out towards the matrix, presents an interesting size effect: the lowest value of the strain is found for the thinnest laminates, whilst the highest strain for the intermediate in thickness laminates. Note that current simulations predict nonuniform evolution since this phenomenon has a notable influence of the specific internal arrangement of the material, i.e. fiber locations, matrix-rich regions, among other aspects.

Interestingly, for the transverse crack a monotonic size effect can be identified, from the thinnest laminate to the thickest one, the size effect complies with the classical size effect reported by Parvizi (41) and subsequent experiments (181; 182; 183). This trend exhibits a decreasing evolution of the critical strain leading to a first through the thickness transverse crack as the 90° layer thickness increases. The reason for this size effect can be understood by comparing the evolution of the three stages plotted in Figure 50. Whereas first and second stages are very dependent on scattering on fibers arrangements, the third stage is significantly affected by the energy available to be released in a potential crack propagation. Thus, the key point is the nature of the damage evolution from the very first crack kinking out the fiber-matrix interface towards the matrix up to the full transverse crack. Once the first kink out occurs, the nature of this damage evolution is going to depend on the elastic energy available to propagate this crack up to span the whole thickness. For thinnest laminates, even if the first kink occurs prematurely, the elastic energy available to be released is low and the progression requires a significant increase of strain. In contrast, for the other laminates the increase in strain from second to third stage is significantly lower, showing a behavior much more unstable. In fact, for the thinnest laminate, it is not expected that this stable evolution can be detected by acoustic emission, which is the classical method used to detect transverse cracks in experiments. This crack would be likely detected in a subsequent stage of propagation as tunneling crack, which would be unstable in the last stage.

Beside the previous discussion, it is interesting to analyze the results summarized in Figure 50 advocating previous theoretical models in order to explain the size effect observed in classical experiments, see the review outlined in (183).

One of the most accepted model in the related literature is the so-

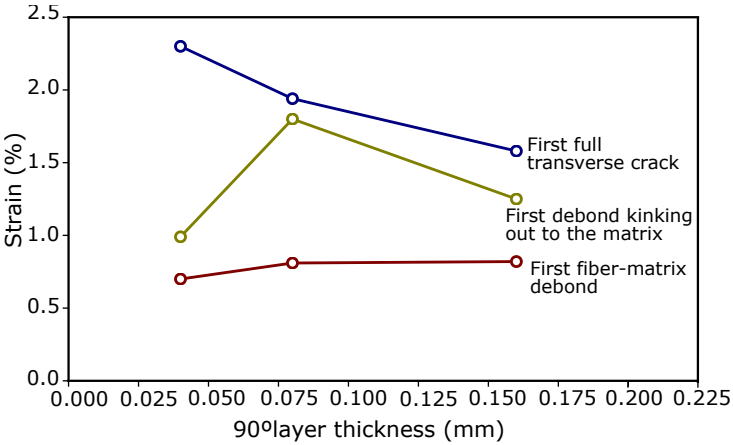

Figure 50: Effect of the 90° layer thickness on the strain for which the different steps of the process of crack initiation are observed in the computational model.

called Dvorak's formulation (180), which is based on assuming that a damage zone grows stably up to a certain critical length where it commences to progress unstably. Under such conditions, the critical length is assumed to be a material property. Very succinctly, the relation between this critical length and the 90° layer thickness promotes the size effect and differences on the crack growth direction (which can evolve either as a tunneling crack or as a transverse through the thickness crack), see (180) for a detailed justification. The weak point of this model relies on the hypothesis of the existence of a "material critical length" governing the transition from stable to unstable crack growth. It is interesting to observe that the transition has been identified here, see discussion in Section 6.3.2. In addition, it is worth noting the nature of crack growth between the first kink and the first transverse through the thickness crack in Figure 50. The evolution is much slower for the thinnest laminate than for the other two laminates, experiencing a clear crack propagation delay. This could be related with the consequence of the Dvorak theoretical model, which claims that: (i) the growth in the thinnest laminates is always stably along the thickness direction, and (2) unstably crack growths mostly occur as a tunneling crack along the width of the specimen.

Note however that two alternative theoretical models, incremental energy criterion (50) and finite fracture mechanics (46; 148), explain the

size effect assuming an abrupt onset of a crack with a finite length. The justification for this abrupt onset is the micro-mechanical transition from damage to crack. Some evidences can be observed here in the transition between a damage zone which span the whole thickness and after the first kink with a fast growth of the crack (particularly for $[0_2^\circ/90_2^\circ/0_2^\circ]$ and $[0_2^\circ/90_4^\circ/0_2^\circ]$). The comprehensive study of this phenomenon, i.e. how abrupt is this crack growth, would require a robust dynamic analysis which falls beyond the scope of the present study.

Finally, within this context, it is worth mentioning the existence of a different theoretical model which relies on the Weibull statistical theory in order to provide a plausible argument to this *in-situ* strength effect, see (53). This model bases the explanation of the size effect on the presence of flaws of a size statistically distributed per unit of volume. Basically, since thicker layers are characterized by larger volumes, they possess a higher probability for the presence of larger flaws. Note however that since the analysis presented here is purely deterministic and no dispersion on the material properties have been introduced, this model cannot be properly evaluated and discussed within the context of the present study.

Chapter 7

Fracture simulation in thin films on compliant substrates

In this chapter, the combination of the phase field approach for brittle fracture and the cohesive zone model (PF-CZM) is used to simulate damage in heterogeneous media with the presence of interfaces in thin layer-substrate systems. The main target is providing a characterization of the different damage patterns that can evolve based on the mechanical properties of the system. For this purpose, we present a comprehensive mechanical study endowing the simulation of several examples with different geometries, cracking paths and types of failure.

In Section 7.1, we simulate a 2D film-substrate system with a single-edge notched under different loading conditions and its respective mechanical properties between the constituents. Additionally, we vary the interface properties and after that, we introduce a secondary notch to evaluate its influence on the corresponding damage pattern. These actions are performed in order to study the influence of different system parameters on the propagation path and therefore, on the type of failure. Finally, recalling the information of the simulations herein under consideration, we construct a failure map of single-edge notched problem, to be able to predict the type of failure knowing the properties of our system.

Subsequently, Section 7.2 exemplary addresses the capabilities of the current numerical methodology to simulate 3D problems involving thin

layer-substrate systems under the three fracture modes.

All the simulations are conducted under displacement control and using the finite element software FEAP (168). This chapter is based on (78). Also, it must be mentioned that, the current numerical method introduces the role of two length scales into the model, l (associated with the PF model) and l_{CZM} (related to the CZM). After the computation of both length parameters (124; 126) for the corresponding material properties, we noticed that both length scales are of the similar order of magnitude, leading to a real competition between the corresponding failure modes. Finally, to clarify that the CZM used to simulate the interface failure is the classical tension cut off law previously described in Section 5.1. Therefore, no coupling is assumed between the phase field variable and the stiffness of the interface due to the fact that where damage is initiated is not known a priori.

7.1 2D film-substrate systems

In this section, we first analyse the failure and crack propagation of the system shown in Figure 51. The geometry and material parameters are collected in Tables 6 and 7.

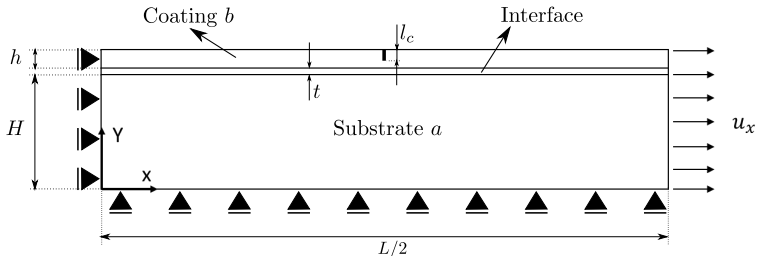

Figure 51: 2D film-substrate under tension: geometry.

L/t	2000	Specimen length/Interface thickness
h/t	25	Coating thickness/Interface thickness
H/t	250	Substrate thickness/Interface thickness
l_c/t	5	Notch length/Interface thickness

Table 6: 2D film-substrate under tension: geometrical parameters.

$E_a/\mathcal{G}_a$	1×10^7	Substrate Young modulus/Substrate Fracture energy
$E_b/\mathcal{G}_a$	5×10^8	Coating Young modulus/Substrate Fracture energy
$\nu_a/\mathcal{G}_a$	111	Substrate Poisson ratio/Substrate Fracture energy
$\nu_b/\mathcal{G}_a$	111	Coating Poisson ratio/Substrate Fracture energy
$\mathcal{G}_b/\mathcal{G}_a$	10	Coating Fracture energy/Substrate Fracture energy
$l/\mathcal{G}_a$	83.33	Phase field length scale parameter/Substrate Fracture energy
$\mathcal{G}_I/\mathcal{G}_a$	0.67	Interface Fracture energy for Mode I/Substrate Fracture energy
$\mathcal{G}_{II}/\mathcal{G}_a$	2.67	Interface Fracture energy for Mode II/Substrate Fracture energy
$\sigma_I/\mathcal{G}_a$	25×10^3	Interface Maximum traction for Mode I/Substrate Fracture energy
$\sigma_{II}/\mathcal{G}_a$	30×10^3	Interface Maximum traction for Mode II/Substrate Fracture energy
α	0.96	Dundurs' parameter α
β	0.24	Dundurs' parameter β

Table 7: 2D film-substrate under tension: mechanical properties.

In order to determine the influence of the interface properties on the failure of our system, the interface fracture energy for mode I, $\mathcal{G}_I$, is varied with respect to the baseline value in Table 7. This leads to three different configurations of the system: weak interface ($\mathcal{G}_I$), intermediate interface ($\mathcal{G}_I\times10$) and strong interface ($\mathcal{G}_I\times$ 100). From Figure 52, it can be noticed that for a weak interface, the predominant failure mode is due to pure delamination. However, for the strongest interface case, the interface represents a high energetic barrier that is very difficult to delaminate. For that reason, the crack penetrates into the substrate instead upon the complete system collapse. Finally, we analyze an intermediate situation, where there is delamination on the interface until a certain position following a symmetric pattern, and subsequently these damage events penetrate into the substrate instead of continuing the delamination path along the interface. These results illustrate the capabilities of the formulation in rather complex damage situations, verifying the current methodology.

It is also worth mentioning that from a quantitative point of view, the dissipated energy is different in each of the previous cases, according to the stress-strain evolution curves depicted in Figure 52. For instance, although in the delamination and penetration cases there is only one dissipation mechanism, the overall dissipated energy in the delamination case is smaller with respect to the strongest interface configuration. This is due to the difference between their corresponding fracture energies being much smaller the fracture energy of the interface than the one associated to the penetration failure (film and substrate).

Finally, for the intermediate case, there are two dissipation mecha-

nisms (delamination and penetration) which means that, in this case, the value of the dissipated energy corresponds to the highest one. This latter effect can be seen from the secondary branch of the corresponding response after the first drop of the evolution, featuring the system a modified stiffness (governed by the substrate) upon complete failure (second drop in the response).

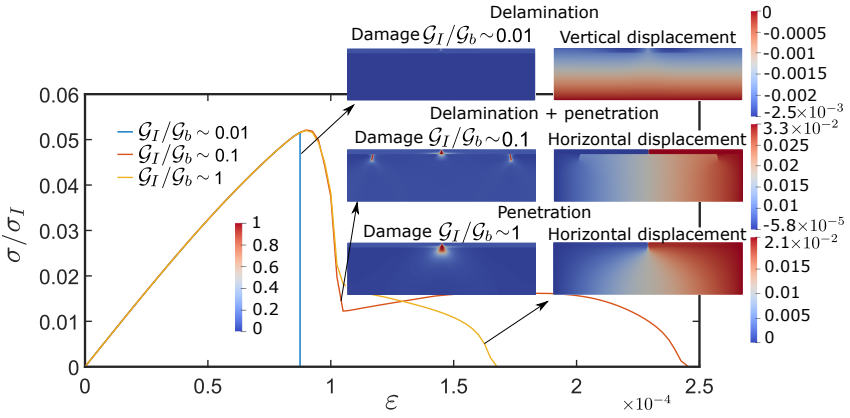

Figure 52: 2D film-substrate under tension problem: influence of $\mathcal{G}_I$ on the stress-strain evolution curve (stress of the system/stress-layer).

It is important to remark that current results represent a largely novel contribution to the state of the art regarding the analysis of the characteristic failure mechanisms in thin layer-substrate systems, which are principally confined to fracture aspects around the common interface. Differing from this, the current approach enables capturing a complete range of damage patterns upon complete system failure.

7.1.1 2D film-substrate system: secondary notch

Now, we introduce a secondary notch in our problem, close to the previous notch at the center of the system. The distance from the main notch to the secondary one is h_c: h_c/t=25. We aim at illustrating the influence of a secondary notch on the damage patterns and also the role of the interface fracture toughness $\mathcal{G}_I$, as was performed in the previous section. For this purpose, we simulate two problems, each of them corresponding

to different values of the secondary notch length: $l_c/2$ and l_c. The geometries of the problems are given in Figure 53 and the results are shown in Figure 54 and 55.

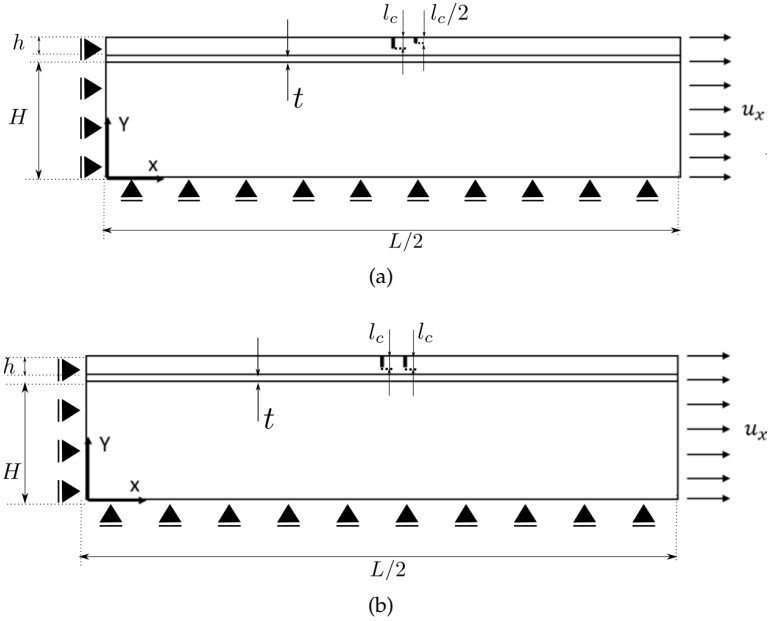

Figure 53: (a) Secondary notch of length equal to $lc/2$. (b) Secondary notch of length equal to lc.

Analyzing the results here obtained from a qualitative standpoint, we can argue that the influence of the secondary notch on the problem response depends on its length. Thus, it can be observed that when the secondary notch length is equal to $l_c/2$, the results are the same as the results of the one notch problem, i.e. with no interactions between notches. However, when the second notch is of the same length as the main one, the results are different because there is a clear interaction between the cracks that appear in both notches.

Summarizing current results, the following differences between single and double notched configurations can be identified where there exists interaction between the two notches:

- In the case of weak interfaces, if a secondary flaw is considered, the

result is the same as in the single notch problem (delamination). This means that the interface failure is not affected by the presence of a second notch.

- For intermediate tough interfaces and two interacting notches, current simulations only predict delamination events for longer secondary notches. Moreover, the dissipated energy decreases and the failure happens under smaller strain levels in comparison with the single notch specimen. Therefore, it can be stated that the presence of the secondary notch causes a different type of failure (delamination instead of delamination followed by penetration) as a consequence of the shielding effect between the two notches which makes more difficult the release of energy through the film than through the interface.

- Finally, for very tough interfaces, the predicted type of failure does not change between the single and the double notched systems (penetration) regardless the length of the secondary notch. However, the maximum stress shows a slight increase in comparison with the single notch configuration. Therefore, it can be concluded that there is a shielding effect as well as in the intermediate interface case.

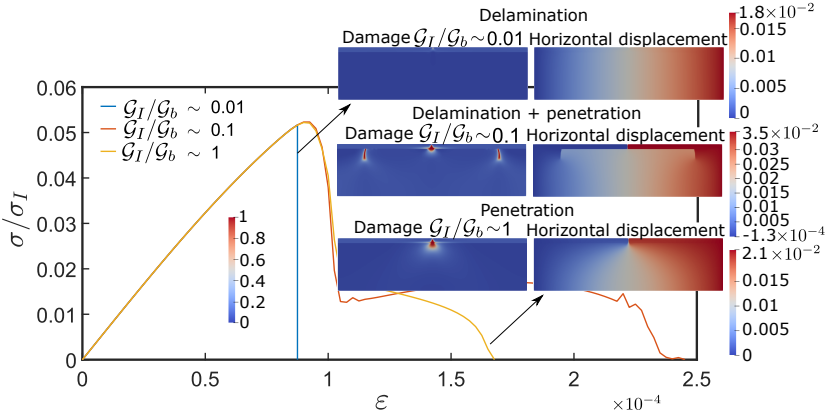

Figure 54: Secondary notch of length equal to $lc/2$: influence of $\mathcal{G}_I$ on the stress-strain evolution curve.

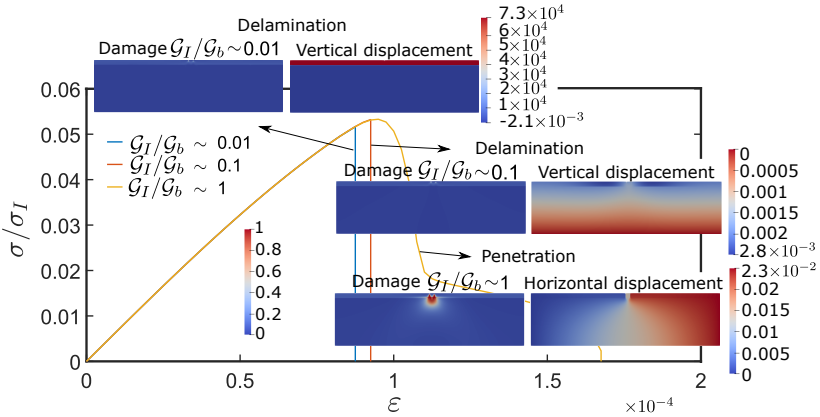

Figure 55: Secondary notch of length equal to lc: influence of $\mathcal{G}_I$ on the stress-strain evolution curve.

7.1.2 2D film-substrate system under bending

In the previous problems, the failure corresponded to pure fracture mode I. In this section, we aim at extending our study analyzing the systems responses under mixed fracture modes (mode I and II), which can be introduced by adding a vertical displacement leading to in-plane bending (See Figure 56).

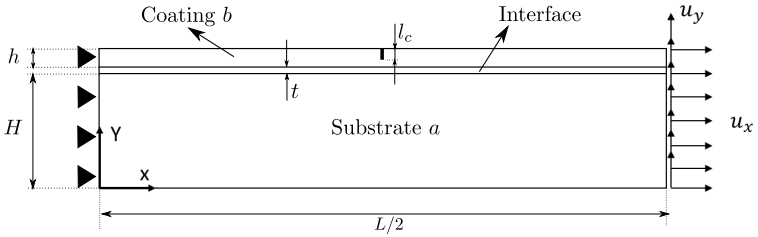

Figure 56: 2D film-substrate under bending: geometry.

Two problems have been examined: (a) a external solicitation for which the vertical and horizontal imposed displacements are of the same magnitude, and (b) the magnitude of the vertical imposed displacement

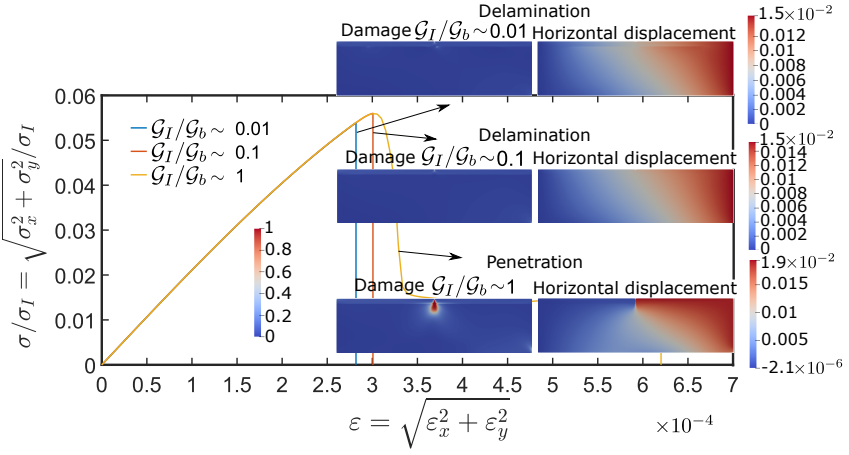

Figure 57: 2D film-substrate system under bending (a): $u_y = -0.05$ and $u_x = 0.05$ mm. Influence of $\mathcal{G}_I$ on the stress-strain evolution curve.

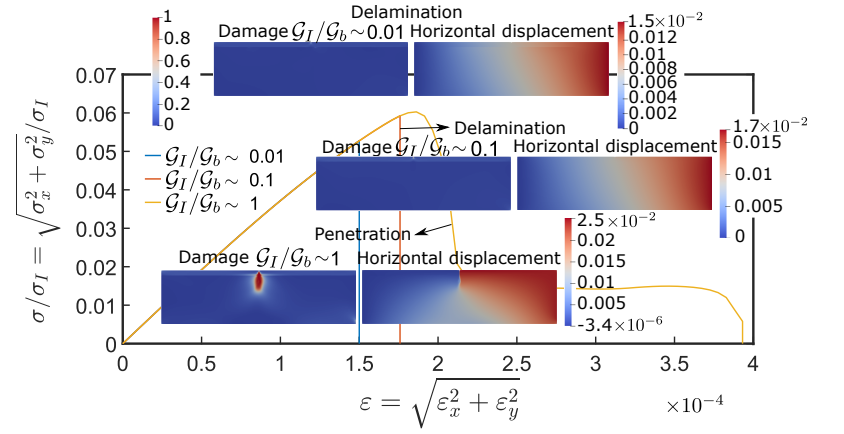

Figure 58: 2D film-substrate system under bending (b): $u_y = -0.05$ mm and $u_x = 0.1$ mm. Influence of $\mathcal{G}_I$ on the stress-strain evolution curve.

is the half with respect to that corresponding to the horizontal one.

The corresponding simulation results to the solicitations (a) and (b) are shown in Figure 57 and 58. In these graphs it can be seen that in the case of a weak or an intermediate interface, the governing failure is due

to thin layer-substrate delamination. However, the dissipated energies are different due to the difference on the order of the interfaces fracture energies. In the case of a strong interface, there is propagation through the substrate. Finally, qualitatively, it can be stated that in all the interface cases herein considered, as the horizontal displacement decreases, the stiffness of the system decreases and the deformation of failure increases.

7.1.3 2D film-substrate system: failure map.

Through the exploitation of the current numerical approach, in this section, we aim at constructing an overall failure map of the 2D film-substrate system, which is given in Figure 51 for different values of the Dundurs' parameter α and also, different values of $\mathcal{G}_I$. In that way, knowing the properties of our system, we can determine easily the type of failure that arises. This failure map is shown in Figure 59, where we can see that there are three types of failure: delamination ($0.1 \leq \mathcal{G}_I/\mathcal{G}_b \leq 0.25$), delamination+penetration ($0.75 \leq \mathcal{G}_I/\mathcal{G}_b \leq 1$) and penetration ($5 \leq \mathcal{G}_I/\mathcal{G}_b \leq 43$). From this failure map we can state that as α decreases, the damage in the substrate increases for all the types of failure and for the delamination+penetration case the delamination is reduced. The reason of that is the reduction of the elastic mismatch between the constituents as α decreases.

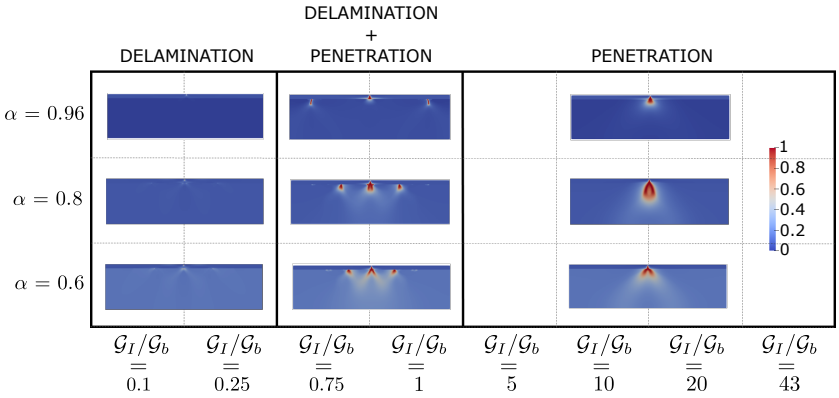

Figure 59: Failure map of the 2D film-substrate system under tension: Dundurs' parameter α vs $\mathcal{G}_I/\mathcal{G}_b$.

7.2 3D film-substrate system

In this section, we focus our attention on examining the capability of the proposed method to model 3D applications of thin layer-substrate systems. To do that, we simulate the 3D problem given in Figure 60. The geometry and material parameters are listed in Table 8 and 9. As can be observed in Figure 60, the geometry is subjected to several loading conditions, so we are simultaneously considering different fracture Modes, i.e. Mode I, II and III in an individual case.

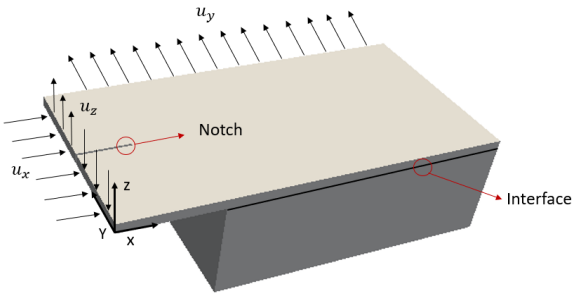

Figure 60: 3D film-substrate system: geometry.

The results of this problem are shown in Figure 61, whereby different failure mechanisms can be identified. Analyzing in detail these results, it can be appreciated that in the weak and intermediate interface cases, the failure is due to delamination. Moreover, for the intermediate interface case, it is observable that the corresponding failure pattern shows the concomitant development of delamination and bulk damage, which is characterized by a notable secondary plateau evolution prior the collapsing point. Differing from this, as can be expected, in the weak interface case, the corresponding failure mode of the system corresponds to the exclusive development of delamination with a single plateau evolution and a subsequent sudden drop. These two failure patterns contrast with that corresponding to the tough interface case, in which the strong energetic barrier of the interface provokes the breakage of the coating and precluding the initiation and evolution of deflection or penetration events along the prescribed interface.

L/t	2020	Specimen length/Interface thickness
L_a/t	1500	Substrate length/Interface thickness
W/t	1000	Specimen width/Interface thickness
h/t	50	Coating thickness/Interface thickness
H/t	500	Substrate thickness/Interface thickness
l_c/t	12	Notch length/Interface thickness

Table 8: 3D film-substrate system: geometrical parameters.

$E_a/\mathcal{G}_a$	3.79×10^4	Substrate Young modulus/ Substrate Fracture energy
$E_b/\mathcal{G}_a$	3.79×10^5	Coating Young modulus/Substrate Fracture energy
$\nu_a/\mathcal{G}_a$	11.71	Coating Poisson ratio/Substrate Fracture energy
$\nu_b/\mathcal{G}_a$	11.71	Substrate Poisson ratio/Substrate Fracture energy
$\mathcal{G}_b/\mathcal{G}_a$	2	Coating Fracture energy ratio/Substrate Fracture energy
$l/\mathcal{G}_a$	3.82×10^{-2}	Phase field length scale parameter/Substrate Fracture energy
$\mathcal{G}_I/\mathcal{G}_a$	0.17	Interface Fracture energy for all Modes/Substrate Fracture energy
$\sigma_I/\mathcal{G}_a$	2.58×10^4	Interface Maximum traction for all Modes/Substrate Fracture energy
α	0.82	Dundurs' parameter α
β	0.16	Dundurs' parameter β

Table 9: 3D film-substrate system: mechanical properties.

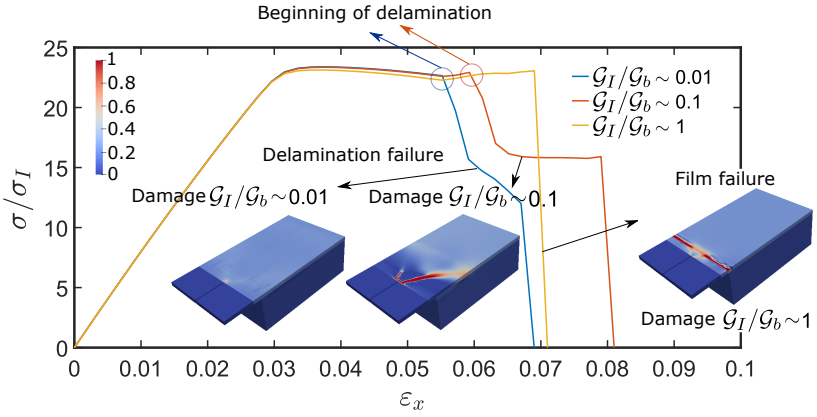

Figure 61: 3D film-substrate system: stress-strain evolution curve and damage pattern.

Chapter 8

Fracture simulation in functionally graded power-based shell structures

In this chapter, the simulation capabilities of a new model for fracture of functionally graded power-based shell structures are examined by means of several numerical examples solved with the finite element program FEAP (168) under displacement control. This new model consists on the phase field (127) combined with the 6-parameter shell formulation (106). Moreover, to obtain a locking-free finite element formulation, two methods are integrated: the enhanced assumed strain (EAS) method and the assumed natural strain (ANS) method. It is worthy to note that this new model has been previously described in Section 4.3 and 4.4. All the examples are made of metallic and ceramic phases whose corresponding properties are listed in Table 10 (126; 163).

Material	E [GPa]	ν	$\mathcal{G}_C$ [N/mm]	l [mm]
Metallic	0.7	0	4.39×10^{-1}	6.45×10^{-3}
Ceramic	1.51	0	7.12×10^{-2}	1.90×10^{-2}

Table 10: Materials properties.

The variation of the Young modulus (E), the fracture energy ($\mathcal{G}_c$) and the phase field length scale (l) with respect to the thickness direction (ξ^3) are given in Figures 62, 63 and 64, for different values of the volume fraction exponent (n). These figures have been obtained taking into account the rule of mixture given in Section 4.4.

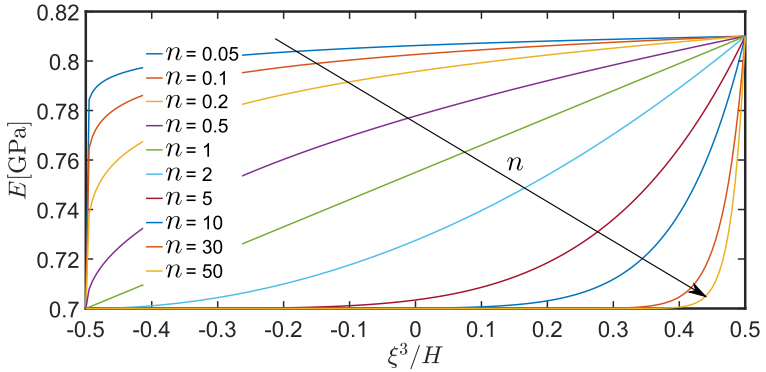

Figure 62: Variation of the young modulus (E) through the thickness (ξ^3) for different values of the volume fraction exponent (n).

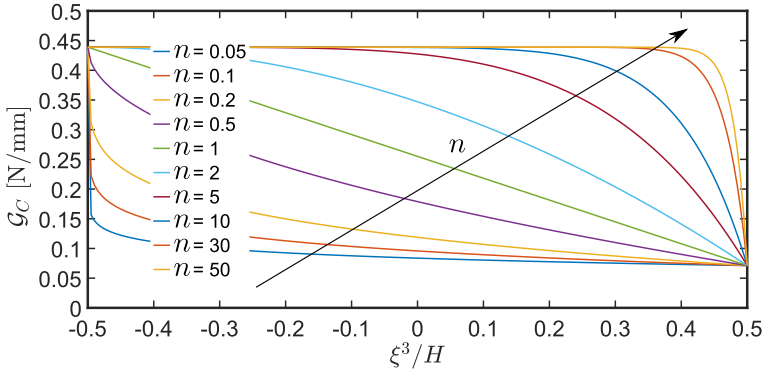

Figure 63: Variation of the critical fracture energy ($\mathcal{G}_C$) through the thickness (ξ^3) for different values of the volume fraction exponent (n).

The present chapter is based on (77) and organized as follows. In Section 8.1, a functionally graded power based square shell under in-plane loads is simulated. However, in Sections 8.2 and 8.3, a functionally

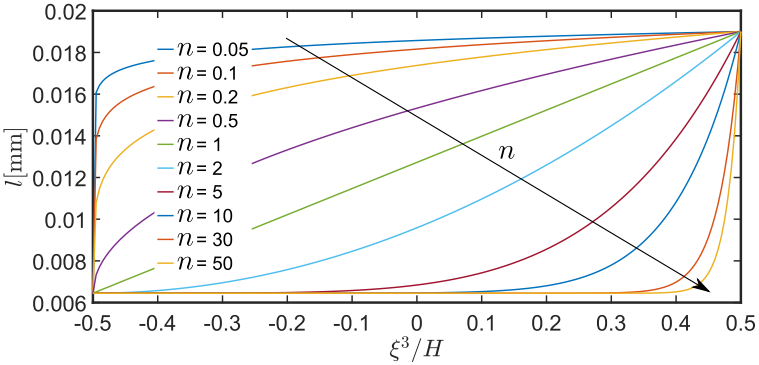

Figure 64: Variation of the phase field length (l) through the thickness (ξ^3) for different values of the volume fraction exponent (n).

graded power-based cylindrical shell is solved under in-plane and out-of-plane loading conditions, respectively. Moreover, the influence of the volume fraction exponent (n) on the applications response is analysed. Also, a comparison between the results obtained with the implementation proposed in this thesis and the solutions for the homogeneous solid shell formulation (106) (fully ceramic and fully metallic materials) is presented for verification purposes.

8.1 Plate under tension

The first problem under consideration is the classical square plate of unit size (L = 1 mm) given in Figure 65. The thickness of the plate, denoted by t, is set equal to 0.0125 mm. This configuration includes an initial sharp notch of length L/2 = 0.5 mm at the centre of the specimen. Regarding the prescribed conditions, a vertical displacement (δ_y) is imposed on the upper side of the plate while the lower side is restrained towards the vertical direction. Regarding the mesh refinement, we employ concentrated discretization scheme around the notch width using 15100 elements.

This problem is simulated for different values of the volume fraction exponent (n) and also for two homogeneous (metallic and ceramic) solid shells. In Figure 66, the stress-strain evolution curves and the contour plot of the phase field variable of the current simulations are given.

Firstly, it can be noticed that, depending on the value of the volume

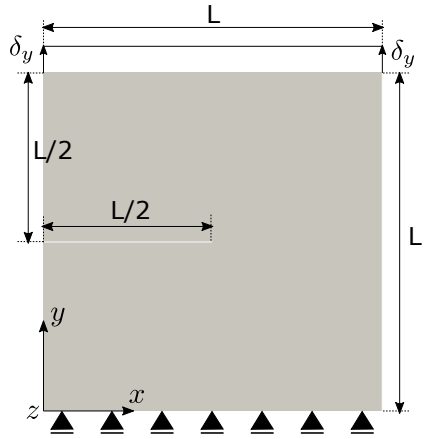

Figure 65: Plate under tension: geometry and boundary conditions.

fraction exponent (n), the behaviour of the system is changing from those of a fully ceramic (n=0) to a fully metallic one ($n \geq 50$). The limit cases of the proposed model (n = 0 and $n \geq 50$) are established by taking into account the variation of the material properties given in Figures 62, 63 and 64. Moreover, in Figure 66, it is possible to see that these limit cases agree with the homogeneous solid shell (SS) elements predictions, which are included for validation purposes.

With reference to the intermediate cases for intermediate values of n, we can see that, as n increases: the dissipated energy, or in other words the area under the stress-strain curve, increases (G_C increases), the stiffness decreases (E decreases) and the apparent strength increases. This is because larger values of n means larger values of the metallic volume fraction (See Equations 4.48, 4.49 and 4.50). Therefore, the material properties consistently change with the variation of the constituents in terms of volume fractions via the corresponding gradation law, as depicted in Figures 62, 63 and 64.

The evolution of the maximum stress when n changes is not determined in a straightforward manner due to the fact that it is an indirect measure in PF models. However, recalling Equation 4.2 and knowing that l decreases when n increases, it can be expected to obtain higher strengths associated to larger values of the n parameter.

It is worth mentioning that, in all the cases herein simulated (homoge-

neous shells and power-based shells with different values of n) the crack path follows an identical pattern and the stress-strain evolution curves present two different stages. The first stage exhibits an increasing stress-strain evolution until a maximum stress is reached. In this stage different events take place: a linear elastic evolution previous damage initiation, the onset of damage and the stable growth of the crack. However, in the second stage, the unstable growth of the crack happens until the complete failure of the system.

Finally, it is worth to point out that the damage pattern given in Figure 66 replicates that corresponding to the homogeneous case because the material properties in the current formulation are exclusively changing in the thickness direction (ξ^3) instead of within the $x-y$ plane. The extension for FGM formulation including both gradation scheme is beyond the matter of the present investigation but of high interest in future activities completing current formulation (132).

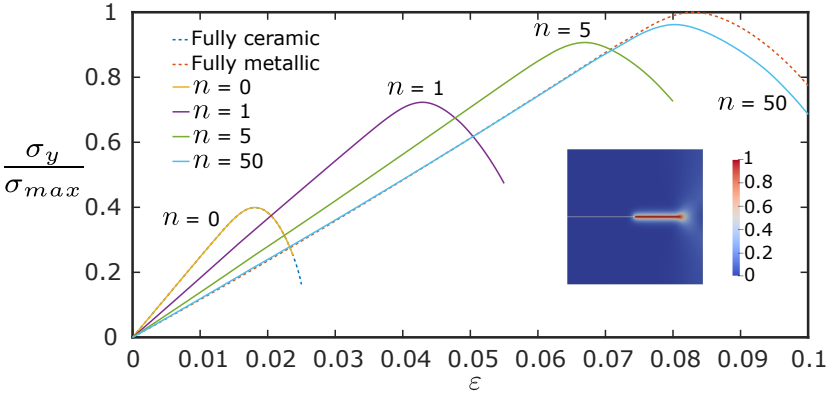

Figure 66: Plate under tension: stress-strain evolution curve and damage pattern (stress of the system/maximum stress, being $\sigma_{max} = 37.45\,\mathrm{N/mm^2}$).

8.2 Cylindrical shell under tension

In this section, we aim at assessing the capabilities of the modelling framework in capturing fracture events in curved structures which are here benchmarked. For this purpose, we consider a quarter of a cylindrical shell with an initial sharp notch at the centre of the specimen (See Fig-

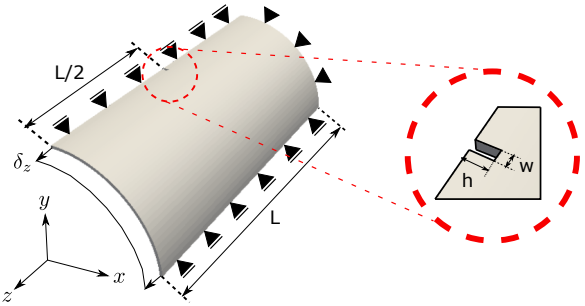

Figure 67: Cylinder under tension: geometry and boundary conditions.

ure 67). The geometrical parameters are: length L = 340.8 mm, internal radius r_i = 100.1 mm, external radius r_e = 103.1 mm, notch length h = 6 mm and notch width w = 3 mm. Regarding the boundary conditions and complying with the symmetry of the system, the x = 0 side is restrained towards the horizontal direction, while the vertical displacements are restrained at the y = 0. In addition to this, the shell is fully clamped to the z = 0 side, while a uniform displacement (δ_z) is imposed on the z = L side. The geometry is discretized using 9920 elements.

In line with the previous application, the curved shell given in Figure 67 is used to simulate functionally graded power-based shells with different values of the volume fraction exponent (n) and also, two homogeneous (metallic and ceramic) solid shells. The stress-strain evolution curves and the contour plot of the phase field variable of the simulations carried out in the present section, are given in Figure 68. It can be observed that the limit cases of the proposed formulation (n = 0 and $n \geq$ 50) are in agreement with the fully ceramic solid shell element and fully metallic solid shell element response, respectively, again pinpointing the robustness of the current methodology. Moreover, for the intermediate cases, the increase of n, which means an increase of the metallic constituent, causes the increase of the maximum stress and the dissipated energy (G_C increases). However, this provokes the reduction of the stiffness of our system (E decreases). As in the previous application, the explanation of the maximum stress increase is due to the reduction of l with the increase of n and to the relation given in Equation 4.2.

Moreover, the response of the system in all the cases considered (Figure 68) shows the same crack path and two different stages in the stress-

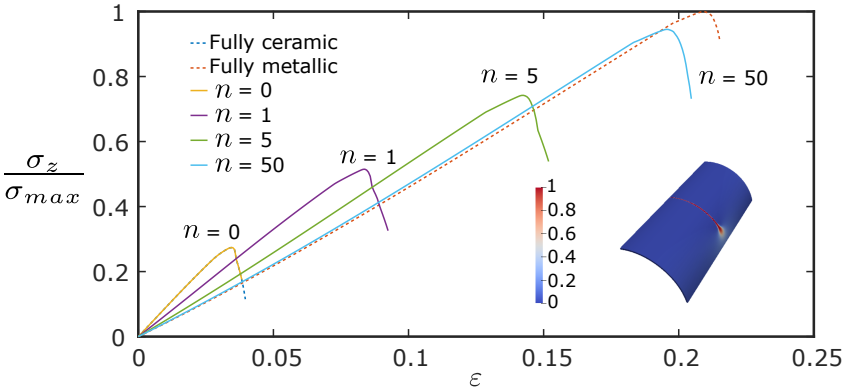

Figure 68: Cylinder under tension: stress-strain evolution curve and damage pattern (stress of the system/maximum stress, being σ_{max} = 171.90 N/mm^2).

strain evolution curve. The first stage shows an increasing stress-strain evolution where three different phases are identified: linear elastic evolution before damage, onset of damage and stable growth of the crack. Finally, in the second stage, the stress-strain evolution curve decreases along the loading path due to the unstable growth of the crack.

8.3 Cylindrical shell under tension and bending

Finally, after proving the applicability of the proposed model to the classical square plate and to a curved shell, we benchmark the current approach for tension-bending problems. To do so, we simulate the cylinder described in the previous section, but adding a vertical displacement (δ_y) at the top of the notch as we can see in Figure 69.

Again, as in the previous simulations, the results given in Figure 70 show that the response of the system changes from fully ceramic (n = 0) to fully metallic ($n \geq 50$) behaviour depending on the value of n. It can be noticed the agreement between the limit cases of the proposed model (n = 0 and $n \geq 50$) and the homogeneous solid shell (SS) element responses.

Moreover, as expected, when the volume fraction of the metallic phase increases, in other words when n raises, the maximum stress and the dis-

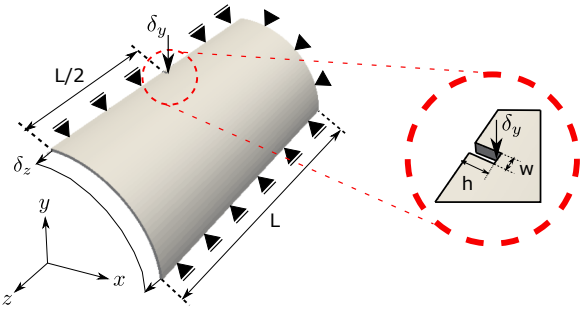

Figure 69: Cylinder under tension and flexion: geometry and boundary conditions.

sipated energy (G_C) increases. However, the stiffness of the system (E) decreases. The explanation of the evolution of the maximum stress with the variation of n is the same as in the previous applications.

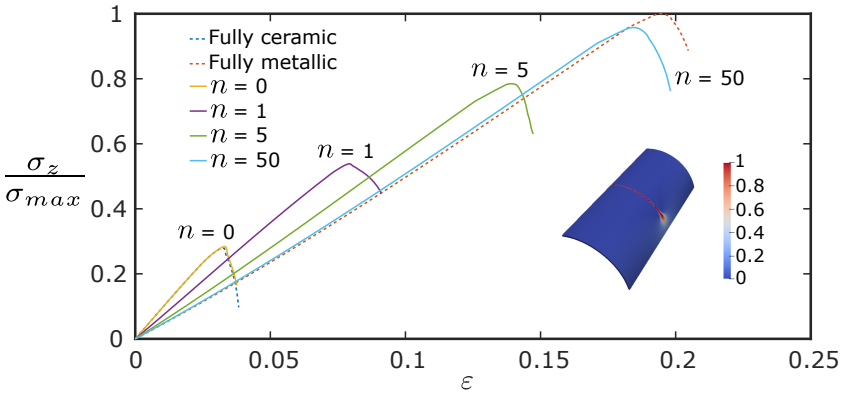

Figure 70: Cylinder under tension and flexion: stress-strain evolution curve and damage pattern (stress of the system/maximum stress, being σ_{max} = 158.86 N/mm^2).

In Figure 70, again, the different stages of the stress-strain evolution curves detected in the previous simulations are also identifiable: an increasing evolution were three different events happen (linear elastic evolution before damage, onset of damage and stable growth of the crack) and a decreasing evolution due to the unstable crack growth.

To conclude, comparing the results of the cylinder under tension with the current simulations, we can state that, although the damage pattern and the stiffness of the system is not notably affected by the inclusion of the vertical displacement δ_y, the maximum stress and the dissipated energy are significantly lower when the vertical displacement δ_y is introduced.

Chapter 9

Conclusions and future developments

9.1 Summary and conclusions

The research work conducted in this thesis deals with the development and assessment of a numerical framework that combined the phase field approach for brittle fracture and the interface-like crack method (denominated PF-CZM method).

The main motivation of this dissertation is focused on the analysis of fracture events in heterogeneous materials at different scales of observations, i.e macro- and micro-scale analysis. In particular, heterogeneous materials used in high-tech industries encompassing principally in this work aerospace and aeronautical applications (long-fiber reinforced composites, thin film-substrate structures, shells and FGMs).

This new approach presents several advantages with respect to alternative computational models used in the literature (strong discontinuous crack methods and continuum damage models) due to its hybrid character. One of the most prominent aspects is the fact that the proposed methodology allows overcoming important problems of crack tracking path and mesh dependency problems. Moreover, it has been evidenced several appealing capabilities of the proposed model to predict fracture in different macro and micro applications with and without the presence of interfaces. Therefore, the enormous versatility of the present model has been proved. Consequently, the denominated PF-CZM would con-

tribute in the achievement of a more profound understanding of complex fracture events in heterogeneous materials and the potential generation of new design and production scenarios for composite materials mainly in aerospace and aeronautical applications.

Results and discussions throughout the text have demonstrated that the scientific targets were successfully met. In the sequel, a more careful description of the main conclusions of the work is provided for a better comprehension.

Firstly, in Chapter 6, we have proved the capability of the proposed model to study failure initiation in long-fiber reinforced composites at the micro-scale and also, the subsequent propagation of damage into the meso-scale. To understand the huge complexity of failure modes in long-fiber reinforced composites, some experimental tests of CFRP composites under uni-axial transverse tension have been conducted in Section 6.1.

In Section 6.2, the failure initiation in composites at the micro-scale by means of the single-fiber problem was thoroughly studied. The approach presented in this thesis (PF-CZM) enabled predicting all the stages of the failure process and its versatility allowed the effect of the problem parameters on the failure process to be characterized. The predictions obtained agreed with the most accepted results presented in the related literature during the last few decades, being the advantage that all the current results were obtained in the present setting by a single robust computational approach without requiring semi-analytical solutions or approximations on the initial stress states.

Continuing with the discussion of the goals regarding the problem of fiber-matrix debonding at the micro-scale, the stages of the process of failure initiation in composites under transverse load were detailed in Section 6.2.1, obtaining an excellent agreement with experiments. This process is characterized by an initial decohesion event that nucleates at the most loaded region of the fiber-matrix interface. After that, this crack in the fiber-matrix interface grows along the interface and subsequently, kinks out the interface through the matrix. Finally, the crack grows through the matrix. In contrast to precedent predictive numerical tools, as those relying on classical fracture mechanics models which assumed an initial debonding angle whose value is around 10°, the current enabled capturing the damage onset which means that it is not necessary to assume an initial debonding angle. Moreover, the proposed model (PF-CZM) predicted a strong size effect of the fiber radius, already reported in previous works and especially in the studies based on finite fracture mechanics. Thus, for small fibers, the critical stress for the

abrupt onset increases. In addition, the failure behavior is much tougher and more ductile for small fibers than for the larger ones.

To complement this study of single-fiber decohesion failure, the effect of a secondary transverse load has also been studied in Section 6.2.2, finding that the presence of a secondary transverse load modified the behaviour of the system. Thus, in scenarios with a tensile secondary loading, the behaviour of the system was much more brittle although the load level required for the onset of decohesion was higher. However, for compression secondary loading, the effect was the contrary. It is important to say that these results agree with other results presented in the literature. Finally, in Section 6.2.3, the influence of a second neighbouring fiber on the failure initiation has been investigated. The results showed the ability of the proposed model to predict the coalescence of damage initiated at two different locations, opening perspectives for the study of complex multi-fiber interaction problems involving shielding and amplification effects.

After the study of failure initiation in long-fiber reinforced composites it was necessary to analyse the propagation of the previous damage in the meso-scale. With this aim, transverse cracking of cross ply laminates was investigated in Section 6.3. To do so, a micro-mechanical analysis of fracture events in cross ply laminates under in-plane monotonic loading has been conducted. The main focus has been the investigation of scale effects in such specimens using high-fidelity computational micro-mechanics. Multi-scale embedded models were generated via the reproduction of the fiber internal arrangements of the specimens reported in (11). Differing from alternative studies, the current numerical strategies encompassed the combined use of the CZM and the PF approach of fracture for respectively, triggering failure events at fiber-matrix and within the matrix. The adaption of such numerical tools ensured the simultaneously accounting for critical elastic energy release rate and critical stress. A detailed description of the computational model used was given in Section 6.3.1. The emphasis of the analysis has been devoted to the careful identification of the different phases of failure events within the specimens in conjunction with the study of the analysis of the 90° layer thickness on the onset of progression of through the thickness crack, which has a strong connection to the so-called *in-situ* strength effect in fibrous composite materials. The predictions carried out in Section 6.3.2 exhibited a closed qualitative agreement with respect to the experimental data available in the related literature, see (41; 46; 63). The proposed numerical technique enables the consistent

capturing of the sequence of damage events in laminates of the family $[0_2^\circ/90_n^\circ/0_2^\circ]$, with n=1, 2 and 4. In particular, it has been identified that the first damage mechanisms correspond to fiber-matrix decohesion events. Upon loading progression such phenomena coalesced leading to the generation of transverse through the thickness cracks within the matrix. Actual crack paths strongly depend on the particular fiber distributions, leading to possible branching and coalescence scenarios especially in thick laminates. This was in good agreement with respect to the experimental data. Nevertheless, our predictions presented deviations with respect to the strain levels at which these phenomena occurred. These differences are mainly attributed to possible 3D effects that have not been taken into consideration in the present 2D modeling framework. Moreover, another reason can be the deterministic character of the proposed computational model. With respect to the analysis of the *in-situ* strength effect in these specimens, it was found that the current numerical technique was in good agreement with the trend introduced by Dvorak's (51; 180; 184) in terms of through the thickness fracture propagation based on the thickness of the central 90° layer. Analyzing the current numerical data, we observed a clear cracking propagation delay within the matrix for the thinnest specimen, which caused the increase in the apparent critical strain for the development of through the thickness damage in comparison with the other two configurations. Nevertheless, note that the current numerical technique was unable to predict such size effect in terms of damage initiation at fiber-matrix interfaces. This inability was again ascribed to the fact that we simplified the problem to a 2D case. However, the results given in Section 6.3 evidenced the strong potential of the proposed numerical framework comprising: (i) the use of physically-based fracture modeling capabilities that properly accounted for capturing size effects in engineering, which cannot be retrieved using Griffith-based theories, linear elastic fracture mechanics and stress-based damage capabilities, among others, (i) its inherent versatility for triggering very complex fracture phenomena with reduced mesh-dependent pathology and without remarkable limitations in terms of geometry and constitutive laws at the material level.

Concerning macro-scale applications, in Chapter 7, the applicability of the proposed model (PF-CZM) to simulate and analyse fracture events in thin film-substrate structures with the presence of interfaces has been proved. The coupling of the PF and the CZM allows the simultaneous simulation of interface delamination and film or substrate damage. Therefore, the proposed model is capable of predicting several com-

plex crack paths and overcomes some of the limitations of discontinuity-based methods discussed previously. In particular, we simulated 2D (Section 7.1) and 3D (Section 7.2) problems, and captured different crack paths depending on the material and fracture properties of the system. Concretely, it has been analysed the influence of the interface fracture energy on the type of failure. For instance, in the 2D film-substrate system, we illustrate the different failure mechanisms that can experience the system based on the interface definition (weak, intermediate or strong) for a given bulk properties. Exploiting the versatility and robustness of the proposed numerical method, simulations enabled the construction of an overall failure map of such systems depending on the fracture properties and the Dundurs' parameter α, yielding to very valuable information regarding the different failure patterns that govern the system response. This is a novel contribution in the field, since this methodology provides a complete failure map, not only analysing the system response around the pre-existing notches and interfaces, but also gives additional information for subsequent propagation into the adjacent substrate upon complete failure.

Finally, in Chapter 8, a novel computational method for the analysis of fracture events in advanced shell structures (functionally graded power-based shells) was used. This method combined the PF approach with the 6-parameter shell formulation. Therefore, conversely to former PF methods for shells, the current model is based on a solid shell kinematic model, which was equipped with the EAS and ANS methods in order to obtain a locking-free element formulation. Then, this development was pioneering in terms of combining: locking-free shells, FGMs and phase field. In addition, it is remarkable to highlight that the proposed model allowed the inclusion of the young modulus, the fracture toughness and the phase field length scale as functions of the thickness coordinate. The attributes of the model comprised: (i) the efficient fracture initiation and propagation and (ii) the potential use for complex geometries and loading conditions. The applicability of this new model was demonstrated by means of several numerical applications. In Section 8.1 a functionally graded power-based plate under in-plane loading conditions was simulated. However, in Sections 8.2 and 8.3 a functionally graded power-based cylindrical shell under different loading conditions was solved. Moreover, the results of these simulations have been verified with the solutions for the homogeneous solid shell formulation (106)(fully ceramic and fully metallic materials). Finally, the influence of the volume fraction exponent (n) on the systems response has been

analysed.

9.2 Future developments

Stemming from the work carried out in this thesis, several research lines can be identified for further developments, which are described in the sequel.

The PF model used in the present thesis, gives very good results with brittle materials. However, there are many applications where plasticity has a very important role. For example, in long-fiber reinforced composites, fibers are elastic but matrices can present important plastic strains. Therefore, a future extension of the present formulation is the inclusion of plasticity, which is currently under development. The main idea can comprise the introduction of two different damage variables. One associated to brittle fracture, as we already have, to model the fiber and other phase field damage variable associated to an elasto-plastic fracture criterion to model the matrix behaviour. It is worth mentioning that the PF model proposed in the present dissertation ensures the irreversible character of the damage process through the introduction of an history variable as in (156). This procedure to ensure damage irreversibility potentially cause some drawbacks reducing the accuracy of the method. In (161) and (185) different procedures to overcome such problems are presented. Therefore, the adoption of these alternatives and a comparison with the current model should be done in the future with the aim of increasing the accuracy of the PF model. Also, taking into account that the proposed PF model does not preclude interpenetration, a future research to avoid this phenomenon should be carried out. A possible way to avoid interpenetration is given in (158). Other future extension paths of the present model will regard the enhancement of this modeling framework for dynamic fracture processes and the impact effect.

Moreover, within the context of the CZM combined with the PF, three different future improvements can be performed. On the one hand, it is assumed a brittle tension cut-off law to describe the behaviour of the interface. For that reason, a possible future approach can be the inclusion of a different cohesive law in order to be able to take into account a progressive degradation. This degradation can be linear, quadratic or any other type of degradation law. On the other hand, we have assumed that the coupling between the PF and the CZM is accomplished by modifying the critical displacement and maintaining constant the energy released.

Other assumptions or considerations about the coupling strategy can be introduced. Finally, it can be very useful to consider the roughness of the interface in our formulation. In the micro-scale, surface related phenomena become notable, in other words, waviness, roughness or other surfaces imperfections affect the heat or stress transfer, among many other types of interactions. A possible procedure to include the roughness of the interface can be obtained following the idea given in (186).

Taking into account that some of the applications simulated in the present dissertation concern Thermal Barrier Coatings (FGMs and thin film-substrate systems), it can be very useful to compute thermal and mechanical strains. Then, a future extension of the proposed formulation to thermo-mechanical problems should be carried out.

Moreover, it can be very interesting to complement this work with experimental tests to achieve a quantitative-qualitative correlation with respect to experimental data.

Concerning the study of fracture in cross ply laminates, a future activity can be the inclusion of interface elements, modelled with the CZMs proposed in this work, between 0° - 90° plies. In that way, we will be able to detect if the transverse matrix crack delaminates or penetrates into the 0° plies. Moreover, the micro-mechanical model proposed in this dissertation to simulate fracture in cross ply laminates has a deterministic character. This can be a possible source of the deviations between our results and the experimental ones. Therefore, in the future, we should consider the random character of the material properties taking into account their medium values and typical deviations or a Weibull distribution.

About thin film-substrate systems, to complement the present work, future research activities regarding further analysis on 3D curved geometries could be done. Moreover, the analysis of wrinkle and buckling instabilities can be very interesting. To address this aim, simulations under compression loading are worth to be investigated. In this direction, it should be pointed out the importance of the adhesive between the film and the substrate although it is out of the scope of the present dissertation. To determine the adhesive properties, peeling tests are needed. In these experiments, it has been observed that the fracture of the adhesive is a complex phenomenon. Therefore, the use of the PF-CZM approach herein proposed for the fracture simulation of an adhesive joint can be very useful. Doing so, we could capture the onset of damage, the kinking through the adherents, delaminations and also the possible propagation through the adherents. For that reason, numerical simulations of peeling tests using the PF-CZM approach are currently under develop-

ment. Also, taking into account that structural adhesives typically have a nonlinear behaviour, the introduction of hyperelasticity in the PF model herein proposed will be the next future development.

In the context of FG power-based shells, can be very interesting to consider the material properties as functions of several directions, not only of the thickness direction (ξ^3).

Other research activity currently under development is the inclusion of a hydrogen-dependent fracture energy degradation, as proposed in (187) , on the PF-CZM formulation here proposed. In that way, we will be able to take into account the problem of hydrogen assisted cracking due to corrosion.

Concerning the study of the free-boundary value problem, it would be very interesting to find a way to solve it using the phase field model.

Finally, one of the main problems of the proposed model is the computational capability because the PF model requires a very small element size. Therefore, with medium or large problem sizes, the number of unknowns is so high that the resolution of the problem is very slow or cannot be possible without super computers. To solve this situation, we need to conduct robust numerical schemes for the parallelization of the code. In other words, we have to move from our implicit formulation to an explicit one in order to obtain an uncoupled system of equations. Doing that, we will be able to simulate bigger problems and therefore, 3D laminates. The main objective of simulating 3D laminates is to be able to capture "tunneling effects" and consequently, the *in-situ* effect in terms of damage initiation that we could not capture in the present work.

References

[1] S. Heimbs and T. Bergmann. High-velocity impact behaviour of pre-stressed composite plates under bird strike loading. *International Journal of Aerospace Engineering*, 2012, 2012. x, 2

[2] M. Floristán, R. Fontarnau, A. Killinger, and R. Gadow. Development of electrically conductive plasma sprayed coatings on glass ceramic substrates. *Surface and Coatings Technology*, 205(4):1021–1028, 2010. x, 3

[3] D.K. Jha, T. Kant, and R.K. Singh. A critical review of recent research on functionally graded plates. *Composite Structures*, 96:833–849, 2013. x, 3

[4] Dr F. Smith. The use of composites in aerospace: Past, present and future challenges. `https://avaloncsl.com/resources-2/presentations/`, 2012. Accessed: 2019-12-03. x, 4

[5] S. T. Pinho, P. Robinson, and L. Iannucci. Fracture toughness of the tensile and compressive fibre failure modes in laminated composites. *Composites Science and Technology*, 66(13):2069–2079, 2006. x, 5

[6] N.J. Pagano, G.A. Schoeppner, R. Kim, and F.L. Abrams. Steady-state cracking and edge effects in thermo-mechanical transverse cracking of cross-ply laminates. *Composites Science and Technology*, 58(11):1811–1825, 1998. x, 6

[7] D. Cao, H. Hu, Q. Duan, P. Song, and S. Li. Experimental and three-dimensional numerical investigation of matrix cracking and delamination interaction with edge effect of curved composite laminates. *Composite Structures*, page 111154, 2019. x, 6

[8] E. Correa, M. I. Valverde, M. L. Velasco, and F. París. Microscopical observations of inter-fibre failure under tension. *Composites Science and Technology*, 155:213–220, 2018. x, 7

[9] San Diego Composites Inc. (SDC). SDC fabricating stiffened fuselage test panels for research on blunt impact of commercial aircraft. http://www.sdcomposites.com/Media/newsarticle120511.html, 2011. Accessed: 2019-12-03. x, 12

[10] R. Groh. A brief history of aircraft structures. http://aerospaceengineeringblog.com/aircraft-structures/, 2012. Accessed: 2019-12-03. x, 12

[11] H. Saito, H. Takeuchi, and I. Kimpara. Experimental evaluation of the damage growth restraining in 90 layer of thin-ply CFRP cross-ply laminates. *Advanced Composite Materials*, 21(1):57–66, 2012. xii, xiii, xv, 10, 85, 86, 87, 88, 89, 90, 91, 97, 98, 100, 101, 102, 128

[12] A. Arteiro, G. Catalanotti, A.R. Melro, P. Linde, and P.P. Camanho. Micro-mechanical analysis of the in situ effect in polymer composite laminates. *Composite Structures*, 116:827–840, 2014. xv, 7, 68, 87, 89, 91, 97

[13] V. Mantič. Interface crack onset at a circular cylindrical inclusion under a remote transverse tension. Application of a coupled stress and energy criterion. *International Journal of Solids and Structures*, 46(6):1287–1304, 2009. xv, 71, 87, 102

[14] M. Paggi and J. Reinoso. Revisiting the problem of a crack impinging on an interface: A modeling framework for the interaction between the phase field approach for brittle fracture and the interface cohesive zone model. *Computer Methods in Applied Mechanics and Engineering*, 321:145 – 172, 2017. xviii, 13, 14, 54, 56, 59

[15] T. Guillén-Hernández, I.G. García, J. Reinoso, and M. Paggi. A micromechanical analysis of inter-fiber failure in long reinforced composites based on the phase field approach of fracture combined with the cohesive zone model. *International Journal of Fracture*, pages 1–23, 2019. 5, 13, 39, 54, 65, 91

[16] T. Guillén-Hernández, A. Quintana-Corominas, I.G. García, J. Reinoso, M. Paggi, and A. Turon. In-situ strength effects in long fibre reinforced composites: a micro-mechanical analysis using the phase field approach of fracture. *Theoretical and Applied Fracture Mechanics*, page 102621, 2020. 5, 13, 39, 54, 65

[17] A.R. Melro, P.P. Camanho, and S.T. Pinho. Generation of random distribution of fibres in long-fibre reinforced composites. *Composites Science and Technology*, 68(9):2092–2102, 2008. 7

[18] E. Totry, C. González, and J. LLorca. Prediction of the failure locus of C/PEEK composites under transverse compression and longitudinal shear through computational micromechanics. *Composites Science and Technology*, 68(15-16):3128–3136, 2008. 7, 8

[19] D. Trias, J. Costa, J.A. Mayugo, and J.E. Hurtado. Random models versus periodic models for fibre reinforced composites. *Computational Materials Science*, 38(2):316–324, 2006. 7

[20] T.J. Vaughan and C.T. McCarthy. A combined experimental–numerical approach for generating statistically equivalent fibre distributions for high strength laminated composite materials. *Composites Science and Technology*, 70(2):291–297, 2010. 7

[21] F. París, E. Correa, and V. Mantič. Kinking of transversal interface cracks between fiber and matrix. *Journal of Applied Mechanics*, 74(4):703–716, 2007. 8

[22] E. Correa, F. París, and V. Mantič. Effect of the presence of a secondary transverse load on the inter-fibre failure under tension. *Engineering Fracture Mechanics*, 103:174–189, 2013. 8, 10, 80

[23] E. Correa, V. Mantič, and F. París. Numerical characterisation of the fibre-matrix interface crack growth in composites under transverse compression. *Engineering Fracture Mechanics*, 75(14):4085–4103, 2008. 8, 66, 68, 71, 72

[24] C. Sandino, E. Correa, and F. París. Numerical analysis of the influence of a nearby fibre on the interface crack growth in composites under transverse tensile load. *Engineering Fracture Mechanics*, 168:58–75, 2016. 8

[25] L. Zhuang, A. Pupurs, J. Varna, R. Talreja, and Z. Ayadi. Effects of inter-fiber spacing on fiber-matrix debond crack growth in unidirectional composites under transverse loading. *Composites Part A: Applied Science and Manufacturing*, 109:463–471, 2018. 8

[26] R. Ballarini, A. Franco, and G. Royer-Carfagni. Wedge-shaped fracturing in the pull out of FRP stiffeners from quasi-brittle substrates. *International Journal of Solids and Structures*, 51(18):3196–3208, 2014. 8

[27] R. Ballarini, L.M. Keer, and S.P. Shah. An analytical model for the pull-out of rigid anchors. *International journal of fracture*, 33(2):75–94, 1987. 8

[28] I. G. García, V. Mantič, and E. Graciani. Debonding at the fibre-matrix interface under remote transverse tension. One debond or two symmetric debonds? *European Journal of Mechanics, A/Solids*, 53:75–88, 2015. 8, 10, 73, 91

[29] M. Muñoz-Reja, L. Távara, V. Mantič, and P. Cornetti. Crack onset and propagation at fibre–matrix elastic interfaces under biaxial loading using finite fracture mechanics. *Composites Part A: Applied Science and Manufacturing*, 82:267–278, 2016. 8

[30] L. Távara, V. Mantič, E. Graciani, and F. París. BEM analysis of crack onset and propagation along fiber–matrix interface under transverse tension using a linear elastic–brittle interface model. *Engineering Analysis with Boundary Elements*, 35(2):207–222, 2011. 8, 71

[31] I. G. García, M. Paggi, and V. Mantič. Fiber-size effects on the onset of fiber-matrix debonding under transverse tension: A comparison between cohesive zone and finite fracture mechanics models. *Engineering Fracture Mechanics*, 115:96–110, 2014. 8, 36, 68, 71, 75, 76

[32] E. Totry, J. M. Molina-Aldareguía, C. González, and J. LLorca. Effect of fiber, matrix and interface properties on the in-plane shear deformation of carbon-fiber reinforced composites. *Composites Science and Technology*, 70(6):970–980, 2010. 8, 66

[33] A.R. Melro, P.P. Camanho, F.M.A Pires, and S.T. Pinho. Micromechanical analysis of polymer composites reinforced by unidirectional fibres: Part II–micromechanical analyses. *International Journal of Solids and Structures*, 50(11-12):1906–1915, 2013. 8, 85

[34] T. J. Vaughan and C. T. McCarthy. Micromechanical modelling of the transverse damage behaviour in fibre reinforced composites. *Composites Science and Technology*, 71(3):388–396, 2011. 8

[35] C. González and J.B. LLorca. Mechanical behavior of unidirectional fiber-reinforced polymers under transverse compression: microscopic mechanisms and modeling. *Composites Science and Technology*, 67(13):2795–2806, 2007. 8

[36] M. Romanowicz. A numerical approach for predicting the failure locus of fiber reinforced composites under combined transverse compression and axial tension. *Computational Materials Science*, 51(1):7–12, 2012. 8

[37] A.R. Melro, P.P. Camanho, F.M.A. Pires, and S.T. Pinho. Micromechanical analysis of polymer composites reinforced by unidirectional fibres: Part I–constitutive modelling. *International Journal of Solids and Structures*, 50(11-12):1897–1905, 2013. 8

[38] L. P. Canal, C. González, J. Segurado, and J. LLorca. Intraply fracture of fiber-reinforced composites: Microscopic mechanisms and modeling. *Composites Science and Technology*, 72(11):1223–1232, 2012. 8, 9

[39] E. Ghorbel. A viscoplastic constitutive model for polymeric materials. *International Journal of Plasticity*, 24(11):2032–2058, 2008. 9

[40] B. Bourdin, G. A. Francfort, and J. J. Marigo. Numerical experiments in revisited brittle fracture. *Journal of the Mechanics and Physics of Solids*, 48(4):797–826, 2000. 9, 16, 38, 71

[41] A. Parvizi, K.W. Garrett, and J.E. Bailey. Constrained cracking in glass fibre-reinforced epoxy cross-ply laminates. *Journal of Materials Science*, 13(1):195–201, 1978. 9, 103, 128

[42] P. P. Camanho, C. G. Dávila, S. T. Pinho, L. Iannucci, and P. Robinson. Prediction of in situ strengths and matrix cracking in composites under transverse tension and in-plane shear. *Composites Part A: Applied Science and Manufacturing*, 37(2):165–176, 2006. 9, 10

[43] P.P. Camanho, P. Maimí, and C.G. Dávila. Prediction of size effects in notched laminates using continuum damage mechanics. *Composites Science and Technology*, 67(13):2715 – 2727, 2007. 9

[44] J. Reinoso, G. Catalanotti, A. Blázquez, P. Areias, P. P. Camanho, and F. París. A consistent anisotropic damage model for laminated fiber-reinforced composites using the 3D-version of the puck failure criterion. *International Journal of Solids and Structures*, 126:37–53, 2017. 9, 16

[45] A. Quintanas-Corominas, P. Maimí, E. Casoni, A. Turon, J.A. Mayugo, G. Guillamet, and M. Vázquez. A 3D transversally isotropic constitutive model for advanced composites implemented in a high performance computing code. *European Journal of Mechanics - A/Solids*, 71:278 – 291, 2018. 9

[46] I.G. García, V. Mantič, A. Blázquez, and F. París. Transverse crack onset and growth in cross-ply [0/90] s laminates under tension. Application of a coupled stress and energy criterion. *International Journal of Solids and Structures*, 51(23-24):3844–3856, 2014. 9, 10, 104, 128

[47] I. G. García, B. J. Carter, A. R. Ingraffea, and V. Mantič. A numerical study of transverse cracking in cross-ply laminates by 3D finite fracture mechanics. *Composites Part B: Engineering*, 95:475–487, 2016. 9, 10

[48] J. Aveston. The properties of fiber composites. In *Conf. Proc. National Physical Lab., 1971*. IPC Science and Technology Press, 1971. 10

[49] K.W. Garrett and J.E. Bailey. Multiple transverse fracture in 90 cross-ply laminates of a glass fibre-reinforced polyester. *Journal of Materials Science*, 12(1):157–168, 1977. 10

[50] Z. Hashin. Finite thermoelastic fracture criterion with application to laminate cracking analysis. *Journal of the Mechanics and Physics of Solids*, 44(7):1129–1145, 1996. 10, 104

[51] G. Dvorak. *Micromechanics of composite materials*, volume 186. Springer Science & Business Media, 2012. 10, 129

[52] P. Maimı, P.P. Camanho, J.A. Mayugo, and A. Turon. Matrix cracking and delamination in laminated composites. Part I: Ply constitutive law, first ply failure and onset of delamination. *Mechanics of Materials*, 43(4):169–185, 2011. 10

[53] D. S. Li and M. R. Wisnom. Evaluating weibull parameters for transverse cracking in cross-ply laminates. *Journal of Composite Materials*, 31(9):935–951, 1997. 10, 105

[54] M.R. Wisnom. 5.03 - size effects in composites. In Anthony Kelly and Carl Zweben, editors, *Comprehensive Composite Materials*, pages 23 – 47. Pergamon, Oxford, 2000. 10

[55] R. Higuchi, T. Okabe, and T. Nagashima. Numerical simulation of progressive damage and failure in composite laminates using XFEM/CZM coupled approach. *Composites Part A: Applied Science and Manufacturing*, 95:197–207, 2017. 10

[56] J. Bieniaś, H. Dębski, B. Surowska, and T. Sadowski. Analysis of microstructure damage in carbon/epoxy composites using FEM. *Computational Materials Science*, 64:168–172, 2012. 10

[57] Y. Wang and H. Waisman. Progressive delamination analysis of composite materials using XFEM and a discrete damage zone model. *Computational Mechanics*, 55(1):1–26, 2015. 10

[58] T.A. Sebaey, J. Costa, P. Maimí, Y. Batista, N. Blanco, and J.A. Mayugo. Measurement of the in situ transverse tensile strength of composite plies by means of the real time monitoring of microcracking. *Composites Part B: Engineering*, 65:40–46, 2014. 10

[59] L. Di Stasio, J. Varna, and Z. Ayadi. Energy release rate of the fiber/matrix interface crack in ud composites under transverse loading: effect of the fiber volume fraction and of the distance to the free surface and to non-adjacent debonds. *Theoretical and Applied Fracture Mechanics*, page 102251, 2019. 10

[60] A. Arteiro, G. Catalanotti, A.R. Melro, P. Linde, and P.P. Camanho. Micro-mechanical analysis of the effect of ply thickness on the transverse compressive strength of polymer composites. *Composites Part A: Applied Science and Manufacturing*, 79:127–137, 2015. 10, 85, 91, 97

[61] M. Herráez, D. Mora, F. Naya, C. S. Lopes, C. González, and J. LLorca. Transverse cracking of cross-ply laminates: A computational micromechanics perspective. *Composites Science and Technology*, 110:196–204, 2015. 10, 85, 97

[62] F. París, M. L. Velasco, and E. Correa. Micromechanical study on the influence of scale effect in the first stage of damage in composites. *Composites Science and Technology*, 160:1–8, 2018. 11

[63] S. Kohler, J. Cugnoni, R. Amacher, and J. Botsis. Transverse cracking in the bulk and at the free edge of thin-ply composites: experiments and multiscale modelling. *Composites Part A: Applied Science and Manufacturing*, 2019. 11, 85, 128

[64] E. Wyart, D. Coulon, T. Pardoen, J.F. Remacle, and F. Lani. Application of the substructured finite element/extended finite element method (S-FE/XFE) to the analysis of cracks in aircraft thin walled structures. *Engineering Fracture Mechanics*, 76(1):44–58, 2009. 11, 15

[65] B. H. Coburn, Z. Wu, and P. M. Weaver. Buckling analysis of stiffened variable angle tow panels. *Composite Structures*, 111:259–270, 2014. 11

[66] C. Meeks, E. Greenhalgh, and B. G. Falzon. Stiffener debonding mechanisms in post-buckled CFRP aerospace panels. *Composites Part A: Applied Science and Manufacturing*, 36(7):934–946, 2005. 11

[67] L. Aktay, A. F. Johnson, and M. Holzapfel. Prediction of impact damage on sandwich composite panels. *Computational Materials Science*, 32(3-4):252–260, 2005. 11

[68] A. Riccio, A. Raimondo, A. Sellitto, V. Acanfora, and M. Zarrelli. Multifunctional polypropylene core for aerospace sandwich composite panels. *Procedia Engineering*, 167:64–70, 2016. 11

[69] C. H. Nguyen, K. Chandrashekhara, and V. Birman. Multifunctional thermal barrier coating in aerospace sandwich panels. *Mechanics Research Communications*, 39(1):35–43, 2012. 11

[70] B. Zhu and Y.J. Cai. A strain rate-dependent enhanced continuum model for elastic-plastic impact response of metal-ceramic functionally graded composites. *International Journal of Impact Engineering*, 133:103340, 2019. 11

[71] S. Kumar, K.M. Reddy, A. Kumar, and G.R. Devi. Development and characterization of polymer–ceramic continuous fiber reinforced functionally graded composites for aerospace application. *Aerospace Science and Technology*, 26(1):185–191, 2013. 12

[72] J. Jang and S. Han. Mechanical properties of glass-fibre mat/PMMA functionally gradient composite. *Composites Part A: Applied Science and Manufacturing*, 30(9):1045–1053, 1999. 12

[73] J. Reinoso, M. Paggi, and R. Rolfes. A computational framework for the interplay between delamination and wrinkling in functionally graded thermal barrier coatings. *Computational Materials Science*, 116:82–95, 2016. 13, 14

[74] W. Y. Lee, D. P. Stinton, C. C. Berndt, F. Erdogan, Y. D. Lee, and Z. Mutasim. Concept of functionally graded materials for advanced thermal barrier coating applications. *Journal of the American Ceramic Society*, 79(12):3003–3012, 1996. 13

[75] M. Peters, U. Schulz, B. Saruhan-Brings, and C. Leyens. Advanced thermal barrier coatings for future aero engines. In *17th INternational Symposium on Airbreathing Engines (ISABE)*, 2005. 13

[76] K.D. Harris, D. Vick, E.J. Gonzalez, T. Smy, K. Robbie, and M.J. Brett. Porous thin films for thermal barrier coatings. *Surface and Coatings Technology*, 138(2-3):185–191, 2001. 13

[77] T. Guillén-Hernández, J. Reinoso, and M. Paggi. Phase field model for fracture analysis of functionally graded power-based shell structures. *Mechanics of Advanced Materials and Structures*, pages 1–11, 2020. 13, 39, 118

[78] T. Guillén-Hernández, J. Reinoso, and M. Paggi. Fracture analysis of thin films on compliant substrates: A numerical study using the phase field approach of fracture. *International Journal of Pressure Vessels and Piping*, 2019. 13, 39, 54, 107

[79] J.Y. Sun, N. Lu, J. Yoon, K.H Oh, Z. Suo, and J.J. Vlassak. Debonding and fracture of ceramic islands on polymer substrates. *Journal of Applied Physics*, 111(1):013517, 2012. 14

[80] H. Zhao, Z. Yu, and H. N. G. Wadley. The influence of coating compliance on the delamination of thermal barrier coatings. *Surface and Coatings Technology*, 204(15):2432–2441, 2010. 14

[81] J. W. Hutchinson. Stresses and failure modes in thin films and multilayers. *Notes for a Dcamm Course. Technical University of Denmark, Lyngby*, 1, 1996. 14

[82] H. Ming-Yuan and J. W. Hutchinson. Crack deflection at an interface between dissimilar elastic materials. *International Journal of Solids and Structures*, 25(9):1053–1067, 1989. 14

[83] J. W. Hutchinson and Z. Suo. Mixed mode cracking in layered materials. In *Advances in Applied Mechanics*, volume 29, pages 63–191. Elsevier, 1991. 14

[84] R. Bermejo and R. Danzer. High failure resistance layered ceramics using crack bifurcation and interface delamination as reinforcement mechanisms. *Engineering Fracture Mechanics*, 77(11):2126–2135, 2010. 14

[85] E. Martin, D. Leguillon, and C. Lacroix. A revisited criterion for crack deflection at an interface in a brittle bimaterial. *Composites Science and Technology*, 61(12):1671–1679, 2001. 14

[86] D. Leguillon, C. Lacroix, and E. Martin. Interface debonding ahead of a primary crack. *Journal of the Mechanics and Physics of Solids*, 48(10):2137–2161, 2000. 14

[87] M. Ortiz and A. Pandolfi. Finite deformation irreversible cohesive elements for three-dimensional crack-propagation analysis. *International Journal for Numerical Methods in Engineering*, 44:1267–1282, 1999. 14

[88] J. Reinoso and M. Paggi. A consistent interface element formulation for geometrical and material nonlinearities. *Computational Mechanics*, 54(6):1569–1581, 2014. 14, 16, 59, 61

[89] S. Goyal, K. Srinivasan, G. Subbarayan, and T. Siegmund. On instability-induced debond initiation in thin film systems. *Engineering Fracture Mechanics*, 77(8):1298–1313, 2010. 14

[90] F. Armero and C. Linder. New finite elements with embedded strong discontinuities in the finite deformation range. *Computer Methods in Applied Mechanics and Engineering*, 197(33-40):3138–3170, 2008. 14

[91] J. Dolbow, N. Moës, and T. Belytschko. An extended finite element method for modeling crack growth with frictional contact. *Computer Methods in Applied Mechanics and Engineering*, 190(51):6825–6846, 2001. 14

[92] W. Pompe, H. Worch, M. Epple, W. Friess, M. Gelinsky, P. Greil, U. Hempel, D. Scharnweber, and K. Schulte. Functionally graded materials for biomedical applications. *Materials Science and Engineering: A*, 362(1-2):40–60, 2003. 15

[93] D. Mahmoud and M. A. Elbestawi. Lattice structures and functionally graded materials applications in additive manufacturing of orthopedic implants: a review. *Journal of Manufacturing and Materials Processing*, 1(2):13, 2017. 15

[94] R. Vassen, H. Kassner, A. Stuke, D. E. Mack, M. O. Jarligo, and D. Stöver. Functionally graded thermal barrier coatings with improved reflectivity and high-temperature capability. In *Materials Science Forum*, volume 631, pages 73–78. Trans Tech Publ, 2010. 15

[95] E. Mueller, Č. Drašar, J. Schilz, and W. A. Kaysser. Functionally graded materials for sensor and energy applications. *Materials Science and Engineering: A*, 362(1-2):17–39, 2003. 15

[96] B. Bartczak, D. Gierczycka-Zbrożek, Z. Gronostajski, S. Polak, and A. Tobota. The use of thin-walled sections for energy absorbing components: a review. *Archives of Civil and Mechanical Engineering*, 10(4):5–19, 2010. 15

[97] W. Abramowicz. Thin-walled structures as impact energy absorbers. *Thin-Walled Structures*, 41(2-3):91–107, 2003. 15

[98] A. L. Kalamkarov, G. C. Saha, and A. V. Georgiades. General micromechanical modeling of smart composite shells with application to smart honeycomb sandwich structures. *Composite Structures*, 79(1):18–33, 2007. 15

[99] V. V. Vasiliev, V. A. Barynin, and A. F. Rasin. Anisogrid lattice structures–survey of development and application. *Composite Structures*, 54(2-3):361–370, 2001. 15

[100] K. Naumenko and V. A. Eremeyev. A layer-wise theory of shallow shells with thin soft core for laminated glass and photovoltaic applications. *Composite Structures*, 178:434–446, 2017. 15

[101] P. Areias, J. H. Song, and T. Belytschko. Analysis of fracture in thin shells by overlapping paired elements. *Computer Methods in Applied Mechanics and Engineering*, 195(41-43):5343–5360, 2006. 15

[102] X. Y. Zhuang, R. Q. Huang, H. H. Zhu, H. Askes, and K. Mathisen. A new and simple locking-free triangular thick plate element using independent shear degrees of freedom. *Finite Elements in Analysis and Design*, 75:1–7, 2013. 15

[103] E. Carrera, M. Cinefra, M. Petrolo, and E. Zappino. *Finite element analysis of structures through unified formulation*. John Wiley & Sons, 2014. 15

[104] M. B. Dehkordi, S. M. R. Khalili, and E. Carrera. Non-linear transient dynamic analysis of sandwich plate with composite face-sheets embedded with shape memory alloy wires and flexible core-based on the mixed LW (layer-wise)/ESL (equivalent single layer) models. *Composites Part B: Engineering*, 87:59–74, 2016. 15

[105] E. Carrera. Theories and finite elements for multilayered plates and shells: a unified compact formulation with numerical assessment and benchmarking. *Archives of Computational Methods in Engineering*, 10(3):215–296, 2003. 15

[106] J. Reinoso, M. Paggi, and C. Linder. Phase field modeling of brittle fracture for enhanced assumed strain shells at large deformations: formulation and finite element implementation. *Computational Mechanics*, 59(6):981–1001, 2017. 16, 17, 46, 51, 52, 117, 119, 130

[107] K. Rah, W. Van Paepegem, A. M. Habraken, J. Degrieck, R. A. de Sousa, and R. F. Valente. Optimal low-order fully integrated solid-shell elements. *Computational Mechanics*, 51(3):309–326, 2013. 16, 51

[108] J. C. Simo, F. Armero, and R. L. Taylor. Improved versions of assumed enhanced strain tri-linear elements for 3D finite deformation problems. *Computer Methods in Applied Mechanics and Engineering*, 110(3-4):359–386, 1993. 16

[109] M. Bischoff and E. Ramm. Shear deformable shell elements for large strains and rotations. *International Journal for Numerical Methods in Engineering*, 40(23):4427–4449, 1997. 16, 48

[110] L. Vu-Quoc and X. G. Tan. Optimal solid shells for non-linear analyses of multilayer composites. i. statics. *Computer Methods in Applied Mechanics and Engineering*, 192(9-10):975–1016, 2003. 16, 51

[111] S. Reese. A large deformation solid-shell concept based on reduced integration with hourglass stabilization. *International Journal for Numerical Methods in Engineering*, 69(8):1671–1716, 2007. 16

[112] O. C. Zienkiewicz, R. L. Taylor, and J. M. Too. Reduced integration technique in general analysis of plates and shells. *International Journal for Numerical Methods in Engineering*, 3(2):275–290, 1971. 16

[113] J. Reinoso and A. Blázquez. Application and finite element implementation of 7-parameter shell element for geometrically nonlinear analysis of layered CFRP composites. *Composite Structures*, 139:263–276, 2016. 16, 46

[114] F. Tornabene and E. Viola. Static analysis of functionally graded doubly-curved shells and panels of revolution. *Meccanica*, 48(4):901–930, 2013. 16

[115] E. Carrera, S. Brischetto, M. Cinefra, and M. Soave. Effects of thickness stretching in functionally graded plates and shells. *Composites Part B: Engineering*, 42(2):123–133, 2011. 16

[116] J. Reinoso, M. Paggi, P. Areias, and A. Blázquez. Surface-based and solid shell formulations of the 7-parameter shell model for layered CFRP and functionally graded power-based composite structures. *Mechanics of Advanced Materials and Structures*, 26(15):1271–1289, 2019. 16, 17

[117] T. Van Do, D. H. Doan, N. D. Duc, and T. Q. Bui. Phase-field thermal buckling analysis for cracked functionally graded composite plates considering neutral surface. *Composite Structures*, 182:542–548, 2017. 16, 17

[118] R. A. Arciniega and J. N. Reddy. Large deformation analysis of functionally graded shells. *International Journal of Solids and Structures*, 44(6):2036–2052, 2007. 16

[119] H. Bayesteh and S. Mohammadi. XFEM fracture analysis of shells: the effect of crack tip enrichments. *Computational Materials Science*, 50(10):2793–2813, 2011. 16

[120] P. M. Areias and T. Belytschko. Non-linear analysis of shells with arbitrary evolving cracks using XFEM. *International Journal for Numerical Methods in Engineering*, 62(3):384–415, 2005. 16

[121] P. D. Zavattieri. Modeling of crack propagation in thin-walled structures using a cohesive model for shell elements. *Journal of Applied Mechanics*, 73(6):948–958, 2006. 16

[122] I. Scheider and W. Brocks. Cohesive elements for thin-walled structures. *Computational Materials Science*, 37(1-2):101–109, 2006. 16

[123] C. G. Dávila, P. P. Camanho, and A. Turon. Cohesive elements for shells. © *NASA TP Technical Reports, 2007, núm. 214869*, 2007. 16

[124] M. Paggi and P. Wriggers. Stiffness and strength of hierarchical polycrystalline materials with imperfect interfaces. *Journal of the Mechanics and Physics of Solids*, 60(4):557–572, 2012. 16, 59, 65, 107

[125] T. T. Nguyen, J. Yvonnet, M. Bornert, C. Chateau, K. Sab, R. Romani, and R. Le Roy. On the choice of parameters in the phase field method for simulating crack initiation with experimental validation. *International Journal of Fracture*, 197(2):213–226, 2016. 16, 40

[126] E. Tanné, T. Li, B. Bourdin, J.J. Marigo, and C. Maurini. Crack nucleation in variational phase-field models of brittle fracture. *Journal of the Mechanics and Physics of Solids*, 110:80 – 99, 2018. 16, 40, 65, 89, 107, 117

[127] C. Miehe, F. Welschinger, and M. Hofacker. Thermodynamically consistent phase-field models of fracture: Variational principles and multi-field fe implementations. *International Journal for Numerical Methods in Engineering*, 83(10):1273–1311, 2010. 16, 40, 42, 117

[128] F. Amiri, D. Millán, Y. Shen, T. Rabczuk, and M. Arroyo. Phase-field modeling of fracture in linear thin shells. *Theoretical and Applied Fracture Mechanics*, 69:102–109, 2014. 16

[129] J. Kiendl, M. Ambati, L. De Lorenzis, H. Gomez, and A. Reali. Phase-field description of brittle fracture in plates and shells. *Computer Methods in Applied Mechanics and Engineering*, 312:374–394, 2016. 17

[130] J. Reinoso, A. Arteiro, M. Paggi, and P.P. Camanho. Strength prediction of notched thin ply laminates using finite fracture mechanics and the phase field approach. *Composites Science and Technology*, 150:205 – 216, 2017. 17, 48, 75

[131] V. Carollo, J. Reinoso, and M. Paggi. A 3D finite strain model for intralayer and interlayer crack simulation coupling the phase field approach and cohesive zone model. *Composite Structures*, 182:636 – 651, 2017. 17, 57

[132] Hirshikesh, S. Natarajan, R. K Annabattula, and E. Martínez-Pañeda. Phase field modelling of crack propagation in functionally graded materials. *Composites Part B: Engineering*, 169:239–248, 2019. 17, 53, 121

[133] G. A. Holzapfel. Nonlinear solid mechanics: a continuum approach for engineering science. *Meccanica*, 37(4):489–490, 2002. 19

[134] C. Truesdell and W. Noll. The non-linear field theories of mechanics. In *The non-linear field theories of mechanics*, pages 1–579. Springer, 2004. 19

[135] F. París. *Teoría de la elasticidad*. Universidad de Sevilla, Escuela técnica Superior de Ingenieros Industriales, 1998. 19

[136] E. W. V. Chaves. *Notes on continuum mechanics*. Springer Science & Business Media, 2013. 19

[137] M. E. Gurtin. *An introduction to continuum mechanics*, volume 158. Academic press, 1982. 19

[138] O. C. Zienkiewicz and R. L. Taylor. *The finite element method for solid and structural mechanics*. Elsevier, 2005. 29

[139] P. Wriggers. *Nonlinear finite element methods*. Springer Science & Business Media, 2008. 29

[140] C. E. Inglis. Stresses in a plate due to the presence of cracks and sharp corners. *Trans Inst Naval Archit*, 55:219–241, 1913. 34

[141] A. A. Griffith. The phenomena of rupture and flow in solids. *Philosophical transactions of the royal society of london. Series A, containing papers of a mathematical or physical character*, 221(582-593):163–198, 1921. 35, 40

[142] G. R. Irwin. Analysis of stresses and strains near the end of a crack transversing a plate. *Trans. ASME, Ser. E, J. Appl. Mech.*, 24:361–364, 1957. 35, 36

[143] T. L. Anderson. *Fracture mechanics: fundamentals and applications*. CRC press, 2005. 36

[144] G. R. Irwin. Onset of fast crack propagation in high strength steel and aluminum alloys. Technical report, NAVAL RESEARCH LAB WASHINGTON DC, 1956. 36

[145] D. S. Dugdale. Yielding of steel sheets containing slits. *Journal of the Mechanics and Physics of Solids*, 8(2):100–104, 1960. 36

[146] A. A. Wells. Unstable crack propagation in metals: cleavage and fast fracture. In *Proceedings of the crack propagation symposium*, volume 1, 1961. 36

[147] J. R. Rice. A path independent integral and the approximate analysis of strain concentration by notches and cracks. *Journal of Applied Mechanics*, 35(2):379–386, 1968. 36

[148] D. Leguillon. Strength or toughness? a criterion for crack onset at a notch. *European Journal of Mechanics-A/Solids*, 21(1):61–72, 2002. 36, 104

[149] P. Cornetti, N. Pugno, A. Carpinteri, and D. Taylor. Finite fracture mechanics: a coupled stress and energy failure criterion. *Engineering Fracture Mechanics*, 73(14):2021–2033, 2006. 36

[150] G. Catalanotti and P. P. Camanho. A semi-analytical method to predict net-tension failure of mechanically fastened joints in composite laminates. *Composites Science and Technology*, 76:69–76, 2013. 36

[151] P. P. Camanho and C. G. Dávila. Mixed-mode decohesion finite elements for the simulation of delamination in composite materials. 2002. 37

[152] L. Távara, V. Mantič, A. Salvadori, L. J. Gray, and F. París. Cohesive-zone-model formulation and implementation using the symmetric galerkin boundary element method for homogeneous solids. *Computational Mechanics*, 51(4):535–551, 2013. 37

[153] P. Cornetti, M. Corrado, L. De Lorenzis, and A. Carpinteri. An analytical cohesive crack modeling approach to the edge debonding failure of frp-plated beams. *International Journal of Solids and Structures*, 53:92–106, 2015. 37

[154] N. Moës, J. Dolbow, and T. Belytschko. A finite element method for crack growth without remeshing. *International Journal for Numerical Methods in Engineering*, 46(1):131–150, 1999. 37

[155] C. Linder and F. Armero. Finite elements with embedded strong discontinuities for the modeling of failure in solids. *International Journal for Numerical Methods in Engineering*, 72(12):1391–1433, 2007. 37

[156] C. Miehe, M. Hofacker, and F. Welschinger. A phase field model for rate-independent crack propagation: Robust algorithmic implementation based on operator splits. *Computer Methods in Applied Mechanics and Engineering*, 199(45-48):2765–2778, 2010. 38, 39, 40, 41, 42, 43, 46, 52, 131

[157] A. Quintanas-Corominas, J. Reinoso, E. Casoni, A. Turon, and J. A. Mayugo. A phase field approach to simulate intralaminar and translaminar fracture in long fiber composite materials. *Composite Structures*, 220:899–911, 2019. 38

[158] F. Freddi and G. Royer-Carfagni. Regularized variational theories of fracture: a unified approach. *Journal of the Mechanics and Physics of Solids*, 58(8):1154–1174, 2010. 43, 131

[159] C. Steinke and M. Kaliske. A phase-field crack model based on directional stress decomposition. *Computational Mechanics*, Sep 2018. 43

[160] M. Strobl and T. Seelig. A novel treatment of crack boundary conditions in phase field models of fracture. *Proceedings in Applied Mathematics and Mechanics*, 15(1):155–156, 2015. 43

[161] T. Linse, P. Hennig, M. Kästner, and R. de Borst. A convergence study of phase-field models for brittle fracture. *Engineering Fracture Mechanics*, 184:307 – 318, 2017. 43, 131

[162] M. A. Msekh, J. M. Sargado, M. Jamshidian, P. Areias, and T. Rabczuk. Abaqus implementation of phase-field model for brittle fracture. *Computational Materials Science*, 96:472–484, 2015. 46

[163] J. Reinoso and A. Blázquez. Geometrically nonlinear analysis of functionally graded power-based and carbon nanotubes reinforced composites using a fully integrated solid shell element. *Composite Structures*, 152:277–294, 2016. 48, 53, 117

[164] J. C. Simo and F. Armero. Geometrically non-linear enhanced strain mixed methods and the method of incompatible modes. *International Journal for Numerical Methods in Engineering*, 33(7):1413–1449, 1992. 48

[165] C. V. Verhoosel and R. de Borst. A phase-field model for cohesive fracture. *International Journal for Numerical Methods in Engineering*, 96(1):43–62, 2013. 56

[166] A. Turon, P.P. Camanho, J. Costa, and C.G. Dávila. A damage model for the simulation of delamination in advanced composites under variable-mode loading. *Mechanics of Materials*, 38(11):1072 – 1089, 2006. 63

[167] L. Távara, J. Reinoso, D. Castillo, and V. Mantič. Mixed-mode failure of interfaces studied by the 2D linear elastic–brittle interface model: Macro-and micro-mechanical finite-element applications in composites. *The Journal of Adhesion*, 94(8):627–656, 2018. 66

[168] R. L. Taylor. FEAP - finite element analysis program, 2014. 68, 107, 117

[169] B. N. Legarth and Q. Yang. Micromechanical Analyses of Debonding and Matrix Cracking in Dual-Phase Materials. *Journal of Applied Mechanics*, 83, 2016. 72

[170] Z. P. Bažant. *Scaling of structural strength*. CRC Press, 2002. 75

[171] L. Távara, V. Mantič, E. Graciani, and F. París. Modelling interfacial debonds in unidirectional fibre-reinforced composites under biaxial transverse loads. *Composite Structures*, 136:305 – 312, 2016. 79

[172] V. Mantič and I. G. García. Crack onset and growth at the fibre-matrix interface under a remote biaxial transverse load. Application of a coupled stress and energy criterion. *International Journal of Solids and Structures*, 49(17):2273–2290, 2012. 79, 91

[173] L. Zhuang, R. Talreja, and J. Varna. Transverse crack formation in unidirectional composites by linking of fibre/matrix debond cracks. *Composites Part A: Applied Science and Manufacturing*, 107:294–303, 2018. 83

[174] J.M. Berthelot. Transverse cracking and delamination in cross-ply glass-fiber and carbon-fiber reinforced plastic laminates: Static and fatigue loading. *Applied Mechanics Reviews*, 56(1):111–147, 2003. 88

[175] P. Cornetti, A. Sapora, and A. Carpinteri. Short cracks and v-notches: Finite fracture mechanics vs. cohesive crack model. *Engineering Fracture Mechanics*, 168:2 – 12, 2016. 89

[176] I. G. García, V. Mantič, and A. Blázquez. The effect of residual thermal stresses on transverse cracking in cross-ply laminates. An application of the Coupled Criterion of the Finite Fracture Mechanics. *International Journal of Fracture*, 211:61–74, 2018. 90

[177] J.N. Goodier. Concentration of stress around spherical and cylindrical inclusions and flaws. *Journal of Applied Mechanics*, 55:39–44, 1933. 91

[178] B.F. Sorensen and R. Talreja. Effects of nonuniformity of fiber distribution on thermally-induced residual stresses and cracking in ceramic matrix composites. *Mechanics of Materials*, 16(4):351 – 363, 1993. 92

[179] C. Sandino, E. Correa, and F. París. A study of the influence of a nearby fibre on the interface crack growth under transverse compression in composite materials. *Engineering Fracture Mechanics*, 193:1 – 16, 2018. 92

[180] G. J. Dvorak and N. Laws. Analysis of first ply failure in composite laminates. *Engineering Fracture Mechanics*, 25(5-6):763–770, 1986. 102, 104, 129

[181] T. Okabe, H. Sekine, J. Noda, M. Nishikawa, and N. Takeda. Characterization of tensile damage and strength in GFRP cross-ply laminates. *Materials Science and Engineering: A*, 383(2):381–389, 2004. 103

[182] T. Okabe, H. Imamura, Y. Sato, R. Higuchi, J. Koyanagi, and R. Talreja. Experimental and numerical studies of initial cracking in CFRP cross-ply laminates. *Composites Part A: Applied Science and Manufacturing*, 68:81–89, 2015. 103

[183] I.G. García, J. Justo, A. Simon, and V. Mantič. Experimental study of the size effect on transverse cracking in cross-ply laminates and comparison with the main theoretical models. *Mechanics of Materials*, 128:24 – 37, 2019. 103

[184] G.J. Dvorak and N. Laws. Mechanics of first ply failure in composite laminates. *Fracture of Fibrous Composites*, pages 59–69, 1985. 129

[185] C. Kuhn and R. Müller. A continuum phase field model for fracture. *Engineering Fracture Mechanics*, 77(18):3625–3634, 2010. 131

[186] J. Bonari, M. R. Marulli, N. Hagmeyer, M. Mayr, A. Popp, and M. Paggi. A multi-scale FEM-BEM formulation for contact mechanics between rough surfaces. *Computational Mechanics*, pages 1–19, 2019. 132

[187] E. Martínez-Pañeda, A. Golahmar, and C. F. Niordson. A phase field formulation for hydrogen assisted cracking. *Computer Methods in Applied Mechanics and Engineering*, 342:742–761, 2018. 133